Scanning probe microscopy with SQUID-on-tip sensor

Inauguraldissertation

zur
Erlangung der Würde eines Doktors der Philosophie
vorgelegt der
Philosophisch-Naturwissenschaftlichen Fakultat
der Universität Basel

von

Lorenzo Ceccarelli
aus Italien

Basel, 2020

Genehmigt von der Philosophisch-Naturwissenschaftlichen Fakultat auf Antrag von

Prof. Dr. Martino Poggio Fakultatsverantwortlicher	Prof. Dr. José Maria De Teresa Korreferent
Basel, den 21.04.2020	Prof. Dr. Martin Spiess Dekan

Contents

Introduction

During the last years, the scientific community witnessed a fast progress of both experimental and theoretical understanding in the field of condense matter physics. Indeed, the discovery of new materials and their characterization are important challenges, and their application in the everyday life depends on their study. Scanning probe microscopy techniques (SPM) play a crucial role in the nanometer-scale research for the local detection of electrical, magnetic, thermal and morphological signals, allowing for the observation of new phenomena and physical interactions. Recently magnetic imaging technology went through a remarkable improvements in both sensitivity and resolution. Some examples of most successful techniques are spin-polarized scanning tunneling microscopy, magnetic force microscopy (MFM), scanning Hall-bar microscopy, scanning magnetometers with nitrogen-vacancy center in diamond (NV-centers), and scanning superconducting quantum interference devices (SQUID). The aim of this work, is to present the results and performance of a new magnetic scanning probe, and in order to do that, it is important to distinguish between two different types of magnetic scanning probes. The first group includes all the mapping techniques sensitive to the sample magnetization, e.g. neutron diffraction, synchrotron-based-x-ray techniques, scanning tunneling microscopy (STM), and magneto-optic microscopy. The second group includes all those techniques able to sense the magnetic field produced by a sample, e.g. Lorentz microscopy, electron holography, and other SPM techniques like MFM, scanning NV center and scanning SQUID. Direct measurements of magnetization are especially attractive for the investigation of magnetic domains and spin patterns, since magnetization configurations cannot be calculated from stray field measurements alone. The downside for these techniques are the restrictions on the types of samples and conditions of measurement that apply. Our scanning probe falls in the second category. Before introducing our probe, we give an overview about the sensitivity and spatial resolution for other techniques as comparison:

- MFM: the development of magnetic force microscopy followed as natural extension of the atomic force microscopy (AFM). Nowadays, these probes are

able to perform under different conditions, e.g. in liquid, air, vacuum and at different temperatures. The typical spatial resolution is around 100nm (but can reach 10nm), while the sensitivity is related to the mechanical property of the probe itself.

- Hall-bar microscopy: progress has been made for scanning Hall-bars (SHMs), where have been developed a non-perturbative probe with a spatial resolution lower than 100 nm and a sensitivity of 500 μT/Hz$^{1/2}$.

- NV center magnetometry: one of the most recent scanning probes developed (2008), the scanning NV-center magnetometers, are used as scanning single-spin sensors. Their capability to work at almost any temperature condition makes them a powerful experimental tool. Their sensitivity is around 60 nT/Hz$^{1/2}$, with a spatial resolution better than 100 nm. A strong downside for this technique, is the required optical excitation, which poses a limit on the possible samples, since it strongly perturbs materials such as direct-band-gap semiconductors, nanomagnets, and fragile biological structures.

- nanoSQUID: despite the new emerging scanning techniques, SQUIDs remain the most sensitive magnetometers. In the last years, the resolution of this type of probe was improved from micrometer-scale to nanometer-scale, through the use of different strategies, e.g. miniaturization of the pick-up loop of a conventional SQUID, placing it at the extreme corner of the chip where it can come close to a sample. The spatial resolution is around 200 nm, while the sensitivity reaches 130 nT/Hz$^{1/2}$. An important limitation is that SQUIDs only function below the superconducting transition temperature, which is typically only a few Kelvin.

In this thesis, we present the work developed in the past four years, on the fabrication, improvements and applications of a promising scanning probe technique, based on the SQUID technology. As mentioned above, the nanoSQUID sensors improved drastically, but most of them lie on the plane of a large substrate and are therefore complicated to apply as scanning sensors. Although there have been demonstrations of magnetic imaging by scanning samples in proximity to such SQUIDs, the geometry is not amenable to a generally applicable microscopy. To solve this problem, Finkler et al. of the Zeldov group at the Weizmann Institute introduced the SQUID-on-tip (SOT) design, in which a nanoSQUID is fabricated on the end of a pulled quartz tip. These nanoSQUIDs, unlike conventional planar SQUIDs, can have diameters down to 50nm and are positioned on the apex of a sharp tip, hence their name a SQUID-on-tip (SOT). One of the most important advantages in this configuration, is the possibility to have the two Josephson junctions of the SQUID close to the investigated sample, differently from the planar

SQUID setup. This allows us to use the probe not only as magnetometer, but also as an extremely sensitive temperature sensor (below the temperature working range of the superconducting layer of material that composes the SQUID). These sensors allow a local magnetic field sensitivity of 50 nT/Hz$^{1/2}$, temperature sensitivity of 1 μKT/Hz$^{1/2}$, and sample-to-sensor distances down to 10 nm. We work with Pb SOTs which operate at temperatures below 7 K and external magnetic fields up to 1 T. In this thesis, we report two different experiments using this scanning technique:

- In the first experiment, we investigated the magnetic behavior of ferromagnetic nanotubes (FNTs) under the effect of an external applied magnetic field. These FNTs are attracting attention as potential elements in continuosly minituarizing magnetic memory. As the physical size of a unit of information reaches nanoscale, mutual interactions between the units becomes increasingly important. Nanotubes, presenting topologically non-trivial surfaces, allow forming magnetic nanostructures with potentially zero stray fields, thus reducing collective interactions of their assemblies to minimun. Studies of single FNTs until recently were challenging, due to their extremely non-planar topography, small sizes, and consequently small magnetic signals. Application of cantilever magnetometry significantly advanced the experimental determination of the magnetic structure of FNTs, but direct imaging of their stray fields had so far not been possible, due to numerous reasons. In this work as first result, we report direct magnetic imaging of single CoFeB nanotubes of various lengths using our SOT sensor. The combined sensitivity, spatial resolution and large range of operational magnetic fields of the nanoSQUIDs allowed us to image vortex states in FNTs while crossing zero magnetisation state on their hysteresis curves. We show that the existence of the clear vortex state strongly depends on the length and the geometrical perfection of the tubes.

- The second experiment represents the core of this thesis, in which we investigate superconducting vortex dynamics in Molybdenum Silicide (MoSi) thin film. Indeed, superconductors are widely used in many different fields, from quantum information to engineering applications like electromagnetic shielding for experimental setups in low loss signal transport. Non-dissipative current transport and the expulsion of magnetic field lines below critical temperature (T_c) characterize these materials. In type-II superconductors, if not controlled, the presence of vortices and their motion are often detrimental to applications. We use our SOT to image individual vortices in amorphous superconducting MoSi thin films. Spatially resolved measurements of the magnetic field generated by both vortices and Meissner screening satisfy the

Pearl model for vortices in thin films, and yield values for the Pearl length and bulk penetration depth at 4.2 K. Flux pinning is observed and quantified through measurements of vortex motion driven by both applied currents and thermal activation. The effects of pinning are also observed in metastable vortex configurations, which form as the applied magnetic field is reduced and magnetic flux is expelled from the film. The high flux sensitivity and resolution of our SQUID-on-tip scanning probe provides an unparalleled tool for studying vortex dynamics, potentially improving our understanding of their complex interactions. Controlling these dynamics in amorphous thin films is crucial for optimizing devices such as superconducting nanowire single photon detectors (SNSPDs) (the most efficient of which are made from MoSi, WSi, and MoGe) because vortices are likely involved in both the mechanism used for the detection of photons and in the generation of dark counts.

Theory

1.1 Superconductivity

This chapter presents a brief introduction of superconductivity. This is necessary, whereas it is the physics which stands behind both the scanning probe microscopy (SPM) probe (that we used to perform our experiments) and one of the two investigated samples, presented in this work. However this will be only a summary of the most relevant characteristics and behaviors of superconductors, since the topic is already richly developed various academic texts. In the first section, I will present a brief overview as well as the distinction between Type I and Type II superconductors. Then, I will describe two devices based on superconductive principles: Josephson Junctions and Superconducting Quantum Interference Devices (SQUID). These two devices are the fundamental components of our sensitive probe. The following sections will introduce the main theoretical models and phenomena which were used to study the physical behavior of our MoSi superconducting sample; more precisely, the competition between the the forced which push to a vortex expulsion from the sample and the ones which inhibit the vortices dynamics in our sample, will be stressed.

1.1.1 Introduction to Superconductors

Nowadays, commercial technology is based mainly on electrical semiconducting and conducting materials. The latter are represented primarily by metal and metallic alloys characterized by a high conductivity ($\propto 10^5 - 10^7$ S/m). In the beginning of the 20th century, Drude developed a theory describing the motion of the electron in such conductive materials, and in 1933 Sommerfeld demonstrated the validity of this model even considering the new-born quantum mechanics theory. The relationship between the electric field applied $\mathbf{E}$ across an isotropic conductive

material and the electron current density **J**, is given by:

$$\mathbf{J} = \frac{nq^2\tau}{m}\mathbf{E} \tag{1.1}$$

with n the electron number density, q the electron charge, τ the mean free time of the electron and m the electron mass. All these entities are assumed constants except the mean free time, which is a property of the material itself and its lattice structure. Thus it is possible to define:

$$\sigma = \frac{nq^2\tau}{m} \tag{1.2}$$

where σ is the conductivity of the material. The resistivity ρ is given by the inverse of σ. In a metallic sample, the resistivity behavior has a strong dependence on the temperature. The higher is the thermal energy, the higher is the probability for a conductive electron to undergo to an electron-electron or phonon-electron scattering process. Such probability drastically decreases below the Debye temperature T_θ, since the resistivity is described by the following equation [1]:

$$\rho(T) = \rho_0 + AT^5 + BT^p exp(-\hbar\omega_0/k_BT) + CT^2 \tag{1.3}$$

The electron-electron scattering probability is proportional to the quadratic term of T, while the T^5 is linked to the phonon-electron scattering probability (considering a pure metal [2]). The middle term in the right side of the equation is an empirical T-dependent term. It is clear that for temperatures close to the absolute zero, the theoretical expectation for these materials is that the residual resistivity is only depending by the ρ_0 term, which is linked only to the presence of impurities and defects in the material itself. In the first years of the twentieth century, a main focus of physics research was the possibility to reach increasingly lower temperatures. In 1908, Heike Kamerlingh Onnes succeeded in liquefying helium, making low temperatures physics accessible for investigation, and confirming some theoretical models. In 1911, Onnes decided to perform a current-voltage characterization of mercury at low T, since due to the high purity of this metal, one could confirm the theoretical prediction of a low ρ_0 as expected by the Drude model. Surprisingly, it was found that the resistivity of the mercury goes abruptly to 0 below 4.2 K (see Fig. 1.1). After mercury, other elements were tested, showing the same resistivity transition below different, so called, critical temperatures (T_C).

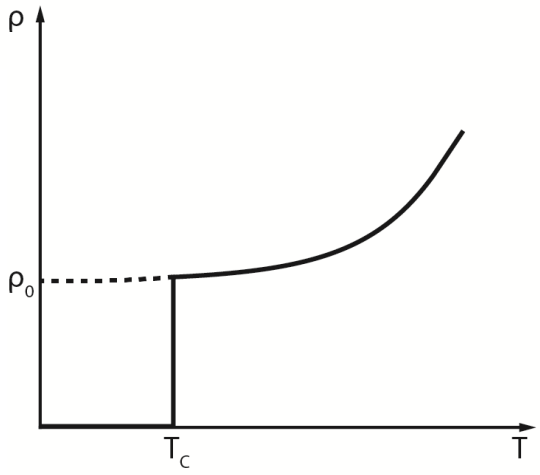

Figure 1.1: The graph shows a comparison between the expected behavior of the resistivity close to 0 K (dashed line), and the superconducting behavior discovered in mercury.

A new state of the matter was discovered. This superconducting state was explained with different approaches. A first attempt was made by Fritz Wolfgang and Heinz London. The two brothers proposed a set of equations, deduced from the phenomenological observation of the superconducting materials, which describe the microscopic electric and magnetic fields [3]:

$$\mathbf{E}_m = \frac{\partial}{\partial t}\left(\frac{4\pi\lambda^2\mathbf{J}_S}{c^2}\right) \tag{1.4}$$

$$\mathbf{B}_m = -\nabla \times \left(\frac{4\pi\lambda^2\mathbf{J}_S}{c}\right) \tag{1.5}$$

where $\mathbf{J}_S$ is the superconducting current density, λ is the penetration depth, c is the speed of light and the m subscript, for both magnetic and electric fields, refers to the microscopic scale. These two equations describe the peculiarities of superconductors, like the continuous acceleration of superconducting electrons without dissipation due to the resistance under an applied electric field, and the exponential screening effect of a sample against an external magnetic field. The last characteristic depends on the above introduced parameter λ, as will be discussed later. In 1950 Ginzburg and Landau proposed an initial form of a theory, which explained the phenomenology of type I superconductors [4], introducing a complex pseudo-wavefunction ψ as an order parameter of the electrons in the medium, and postulating the superconducting state as a second-order phase transition, but without considering the microscopic properties. These properties were considered in 1958 with the postulate of the so called BCS theory (from Bardeen, Cooper

and Schrieffer). Later, Gor'kov showed how the Ginzburg-Landau (GL) theory is a derivation in some limit of the microscopic theory. This theory introduced the coherence length, which is characteristic for each superconducting material:

$$\xi(T) = \frac{\hbar}{|2m^*\alpha(T)|} \tag{1.6}$$

where $\hbar$ is Planck constant and α is the GL parameter. This particular length has an essential role in the definition of the superconducting behavior close to the boundaries or discontinuities of a SC material.

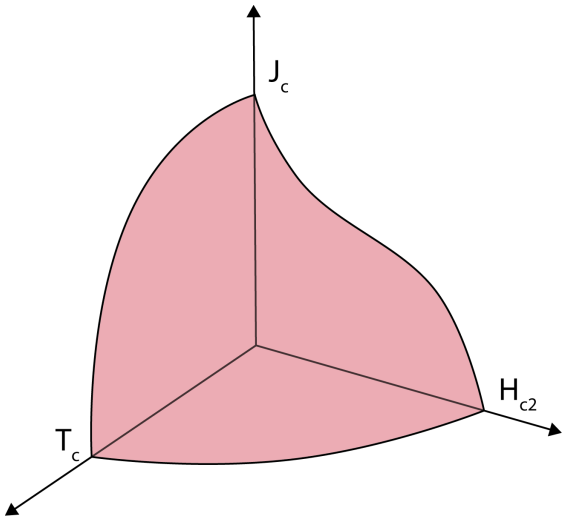

Figure 1.2: The critical surface defines a volume in which the material behaves as a superconductor.

Together with ξ, it is necessary to introduce another important parameter: the penetration depth λ.

$$\lambda(T) = \sqrt{\frac{m^*}{4\mu_0 e^{*2}|\psi|^2}}[1 - (T/T_c)^4]^{-1/2} \tag{1.7}$$

where ψ is the GL pseudo-wavefunction, and m^* and e^* are respectively the effective mass and elementary charge for cooper pairs. This characteristic length is linked to the capacity of a superconducting sample to shield the external magnetic field, which decays exponentially to 0, from the surface of the SC at the distance defined by the λ length. The stability of the superconducting state in a certain element is strongly related to the magnetic field in which it is plunged, the electric field applied across it, and the temperature of the environment. A separated characterization of each of these three entities results in a critical value ($\mathbf{J}_c$, $\mathbf{H}_c$, T_c), at

which the superconductor encounters a phase transition from the superconducting state to the normal state. However, a competitive effect among these three parameters is unavoidable for most experimental setups and conditions. The physical behavior of the superconducting state, as a function of these three variables, can be summarized by the critical surface. The dependence of one parameter on another is connected to the geometric characteristics of the material and its composition, and under certain approximations can be neglected. An example is the dependence of **J** on the external applied field $\mu_0 \mathbf{H}_{ext}$, which can be neglected if we are working in a thin film regime, where **J** can be considered homogeneous for the entire thickness of the sample.

1.1.2 Microscopic Causes of Superconductivity

The BCS theory was formulated after the observation of the T_C dependence on the isotopic mass of the atoms of the material investigated. The emergence of an attractive interaction between electrons in the Fermi surface levels gives rise to a single macroscopic quantum state, in which pairs of negative charges, named Cooper pairs, moves coherently along the entire superconducting material. Such interaction between electrons with opposite spins is mediated by phonons. The indirect interaction between electron pairs can be summarized in two main phenomena:

- The motion of one electron along the crystal structure produces a local distortion of the ions in the lattice;
- The displacement of the ions from their equilibrium position results in their vibration.

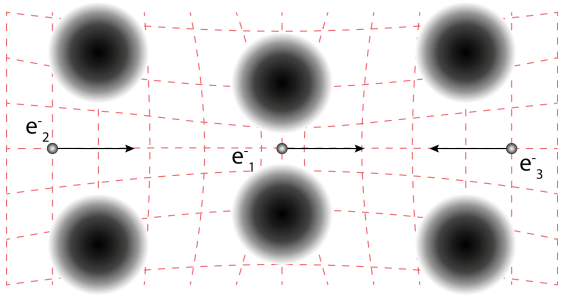

Figure 1.3: The first electron (e_1)deforms the lattice potential of the neighboring ions. A second electron (e_2 or e_3) senses the distorted potential and an attractive interaction between the first and second electrons emerges. The interaction is stronger in case of e_1-e_3 than e_1-e_2, because the momenta of the two electrons are opposite

The timescales of these two events are different, thus when an ion is excited, it goes back to the original position with a relaxation time proportional to ω_D^{-1} the inverse of the Debye frequency; meanwhile the time taken by an electron to pass in proximity of an ion is proportional to $\hbar\epsilon_F^{-1}$. At low T, phonon-electron interactions are suppressed, resulting in $\omega_D^{-1} \gg \hbar\epsilon_F^{-1}$. Therefore, the local lattice potential distortion holds for a time longer than the one required to the electron to pass nearby the excited ion, allowing a second electron to pass on the same path and sensing the same distorted ionic potential. Thus, this delay in the relaxation creates an attractive interaction which is stronger than the Coulomb repulsion. Such a link is more efficient if the momentum of the second electron is opposite to the first one. In Fig.1.3, a simplified version of the process is presented. These electrons have an energy close to the ϵ_F, and since the phononic energy has a magnitude $\propto \hbar\omega_D$, the interaction range is limited in a gap of the same range around the Fermi energy.

1.1.3 Meissner Effect

In 1933, Meissner and Ochsenfeld discovered the second main characteristic of superconductors beside non-dissipative transport of electrical current. If a superconductor is placed in an applied external magnetic field above the T_c, it shows a normal behavior, but once the temperature is decreased below the critical point, the magnetic flux lines are expelled completely from the inside of the specimen. Only in a thin region of its surface, the magnetic flux lines can penetrate with a strong spatial deviation. A superconductor expels completely the flux lines independently of whether the external magnetic field is applied before or after the phase transition. This effect is largely described in literature, and for the purposes of this work it is useful to point out only the strong relationship between the Meissner effect and the geometry of the sample considered. Similarly to the classic magnetic materials, also for superconductors exist conditions, which can boost or counteract the magnetization process, and then the penetration of the external field in the sample. These conditions translate in demagnetizing factors which are linked to the sample geometry [5, 6].As presented in Fig.S1.4 a shielding current density induces a magnetic field which counteracts the external applied field. This screening effect can be derived from the London eq.1.5 and eq.1.4. The external field H_{ext} decreases exponentially at the surface of the superconductor:

$$H_{ext} = H(0)e^{-x/\lambda} \tag{1.8}$$

where x is the distance from the surface of the sample towards the inside of the superconductor.

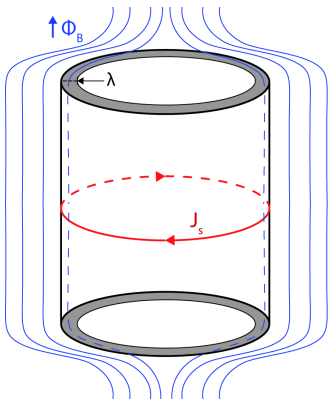

Figure 1.4: The most common shape used to explain the Meissner effect is a cylindrical superconductor. The superconductor is surrounded by magnetic flux parallel to the axis of symmetry of the cylinder. A current density J_s induces an inner field which counteracts the external applied flux Φ_B. The small surface, in which the flux is able to penetrate, has a thickness approximated as the bulk penetration depth (λ).

The shielding current density is related then to the penetration of the magnetic field inside the specimen, because the current is not allowed to exist in the inner part of the superconductor. As introduced before, the geometry of the sample under investigation plays a crucial role to describe our experiments, we use an analytic model applicable in the limit of the thin films ($thickness << \lambda$). In this case the penetration of the magnetic field and the current density distribution have a strong deviation from the model for bulk superconductors [7]. Moreover, as discussed in next paragraphs, for the interaction between the external magnetic field and the sample, one must also to take into account isolated islands inside the material in the normal state, surrounded by the superconducting state. Such behavior is typical for a second category of superconductor: so-called Type II. The interaction between superconductors and magnetic field will be discussed later, highlighting the main concepts useful for the analysis of our experiments.

1.1.4 Discontinuities in Superconducting State

Theory asserts that superconductivity is a macroscopic quantum state, which exists throughout a superconducting material. This is true in an ideal case, and in many theoretical approaches it is considered as a good approximation for describing the experimental results. However, under certain conditions, neglecting the effect of the material structure or discontinuities inside the material, is not possible anymore. Superconductors show a localized normal behavior where superconductivity is broken. In this work, both the probe used, and the sample investigated

are influenced by these discontinuity phenomena. Although the phenomena are similar, deep differences can emerge. These distinctions can be summarized in two categories:

- Artificial discontinuities. These features are planned in the fabrication process to break the superconducting state under certain conditions. Josephson junctions (JJ) are the main example of this category. They can be described as a discontinuity of the superconducting state, which can be fabricated in many ways (e.g. weak links, normal conductor layers, etc.). For the general approach adopted in this paragraph, we treat the most common JJ configuration, that is made by a sandwich of a thin layer of insulating material between two superconducting leads. JJ have a strong importance in this work, as they constitute the basic structure for the quantum probe, that we we used for our experiments (Superconductive Quantum Interference Device, SQUID).

- Random discontinuities. On the contrary of the previous category, these local discontinuities are not planned during the fabrication process, and they can be impurities, defects or contamination of different elements in manifold forms (e.g. grains, layers, filaments etc.). Such elements result in pinning centers, which are the main source for the nucleation of quantized vortices, and magnetization hysteresis in type II superconductors. In the thin film approximation, these effects acquire an increasing prominence, due to the large surface/volume ratio. The study of these pinning centers, and their response to external magnetic and electric fields, is the core of the MoSi sample investigation.

1.1.5 Josephson Junctions

Focusing on the first category reported in the previous paragraph, we can consider the most common JJ, composed by a superconductor-insulator-superconductor (SIS) structure. The thin junction affects the electrical current, producing a phase-dependent voltage across the JJ. One must consider the non-zero thermal energy ($T > 0$) involved in the system. For this reason the current flowing through the JJ element is the sum of the paired-electron current (non-dissipative current), and the quasiparticle current of normal electrons, with a density which depends on the thermal break-up of the Cooper Pairs (CP); this quasiparticle current behaves in a ohmic way. If no voltage arises across the JJ then the contribution of the quasiparticle current vanishes, and the CP pass through the junction with the equivalent of the quantum tunneling mechanism. The current follows the first

Josephson relation:

$$I_s = I_c \sin \delta \tag{1.9}$$

where I_s is the supecurrent, I_c is the critical current and δ is the phase. We assume that the critical current density $J_c = I_c/S_{JJ}$ is homogeneous between the junction surfaces (S_{JJ}), moreover we assume that $0 < T << T_c$, in order to neglect the possibility that the thermal fluctuations destroy the dependence of the supercurrent from δ, and then $I_c > \frac{2ek_bT}{\hbar}$. A voltage drop does not exists across a superconductor below the critical current, and the current follows eq.1.9, but once the current reaches the critical value, then a voltage drop emerges, which is dependent on the time variation of the phase-shift, given by the second Josephson relation:

$$\frac{d\delta}{dt} = \frac{2\pi}{\Phi_0} U \tag{1.10}$$

where Φ_0 is the magnetic quantum flux, and the phase is of the order parameter (or Ginzburg-Landau wavefunction) ψ.

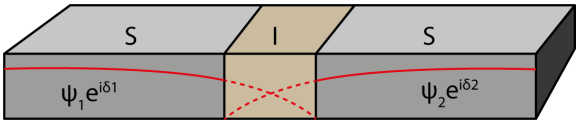

Figure 1.5: The image presents a qualitative view for the spreading of the GL order parameter from the two superconducting leads inside the insulator, described by the function Γ in eq.1.11 , where the $\delta = \delta_2 - \delta_1$ is the phase difference of the JJ.

If we consider the process to occur like a spatial decay of ψ, proportional to the length of the insulating layer, then we can resolve the GL equation [3]:

$$\alpha\psi + \beta|\psi|^2\psi - \frac{\hbar^2}{2m^*}\frac{d^2\psi}{dx^2} = 0 \tag{1.11}$$

with the proper geometric boundary conditions, in order to describe the function for the decay of the CPs inside the non superconducting material. The vector potential $\mathbf{A}$ term has been neglected, since we assume that no magnetic field is applied. Then we can write:

$$\xi^2\frac{d^2\Gamma}{dx^2} + \Gamma - \Gamma^3 = 0 \tag{1.12}$$

with $\Gamma = \psi/\psi_\infty$, the normalized pseudo-wavefunction, and ψ_∞ is the GL parameter inside a superconductor ideally infinitely far from any surface effects. Note that we assumes an equilibrium state for the two SC leads, which allows us to consider $\Gamma = 1$. Aslamazov and Larkin [8] found that for thickness of the insulating layer

smaller than the coherence length ξ, eq.1.12 can be reduced to a Laplace equation with a general solution, in the one dimensional case, given by:

$$\Gamma = (1 - x/L) + (x/L)\exp(i\delta) \tag{1.13}$$

with x the spatial variable and L the length of the insulating layer. Using this form for the Γ function in the GL equation, one can obtain eq.1.9 which defines the phase shift due to the junction. For the aim of this work, it is useful to consider the JJ as a circuit component. We use the resistively and capacitively shunted junction model (RCSJ) for the description of the dynamics of a JJ; it can be represented by a circuit equivalent to the one reported in Fig.1.6 [9].

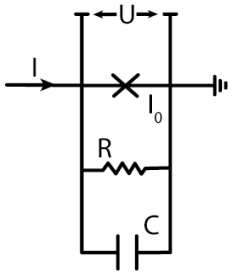

Figure 1.6: The schematic represents both the contribution of the quasiparticle current (R), the superconducting current (given by eq.1.9), and the nonlinear conductance (C) which holds the dependence on voltage and T.

In a RCSJ, it is assumed that the resistance given by the quasiparticle contribution to the current is constant, and its value is taken as the resistance of the junction in the normal state. The circuit equation can be written as:

$$C\frac{dU}{dt} + \frac{U}{R} + I_c \sin\delta = I \tag{1.14}$$

Introducing the potential from 1.10, which is time dependent, it results in a non-linear differential equation:

$$\frac{\Phi_0}{2\pi}C\frac{\partial^2\delta}{\partial t^2} + \frac{\Phi_0}{2\pi}\frac{1}{R}\frac{\partial\delta}{\partial t} + \frac{2\pi}{\Phi_0}\frac{\partial U_t}{\partial\delta} = 0 \tag{1.15}$$

where U_t corresponds to the tilted washboard potential [9] for the junction. It is obtained by:

$$U_t = \int_0^t I_s U dt = \frac{\Phi_0}{2\pi}\int_0^t \frac{\partial\delta}{\partial t} I_c \sin\delta dt = \frac{\Phi_0}{2\pi}\int_0^\delta I_c \sin\delta d\delta \tag{1.16}$$

then it results in:

$$U_t = \frac{\Phi_0}{2\pi}[I_c(1-\cos\delta) + I_s\delta] \tag{1.17}$$

in this equation for the tilted washboard potential the multiplication factor is the Josephson coupling energy ($E_j = \Phi_0/2\pi$). The complete form of eq.1.15, together with eq.1.17, describes the dynamic phase evolution, and it recalls the equation of motion of a particle with mass M, and damping coefficient η, in the potential U_t.

$$M\ddot{x} + \eta\dot{x} + \nabla U_t = 0 \tag{1.18}$$

with the damping proportional to R^{-1} of the junction and the mass to the capacitance.

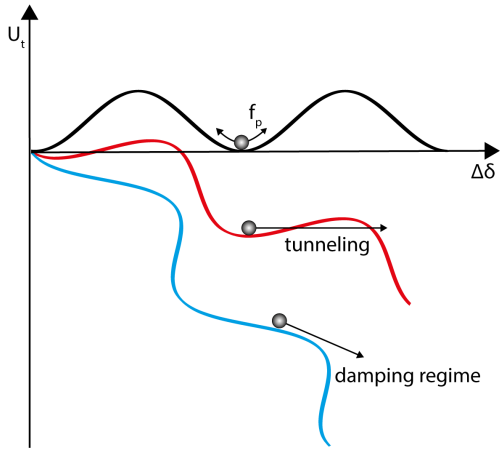

Figure 1.7: Representation of the tilted washboard potential. The tilt is depending on the bias current applied.

In Fig.1.7 the three main cases are reported. If no bias current is applied across the junction the potential is flat, and the oscillations of the analogous particle occur at the junction plasma frequency (f_p). These oscillations of the phase in the minimum of potential are exponentially dependent on the plasma frequency ($\Delta\delta = C\exp(if_pt)$). Once a bias current is applied below the I_c value, the tunneling effect becomes relevant and the rate is proportional to the current itself. Once the bias current is higher than I_c the damping regime takes over, and the junction behaves in a ohmic regime. For the previous argument, we did not consider the thermal activation due to thermal fluctuations, which can induce a phase shift even with zero bias current applied [10]. These fluctuations are one of the main causes for the hysteretic behavior of a junction along the I-V characteristic path defined by the ramp up end a following reduction of the bias current. The underdamped and overdamped regimes for a junction are mainly due to this thermal effects and one of the most relevant effects is the respectively increasing or lowering of the I_c [3].

1.1.6 SQUID

The superconducting quantum interference device (SQUID) is a superconducting ring with two JJ placed as shown in the diagram reported in Fig.1.8. The supecurrent I_s is limited by the sum of the critical currents of the two junctions. This device is a powerful magnetometer, indeed its critical current depends on the overlap of the two superconducting wavefunctions through the two branches of the ring. When magnetic flux passes through the ring it modulates the I_c with a period equal to one quantum flux ($\Phi_0 = h/2e$).

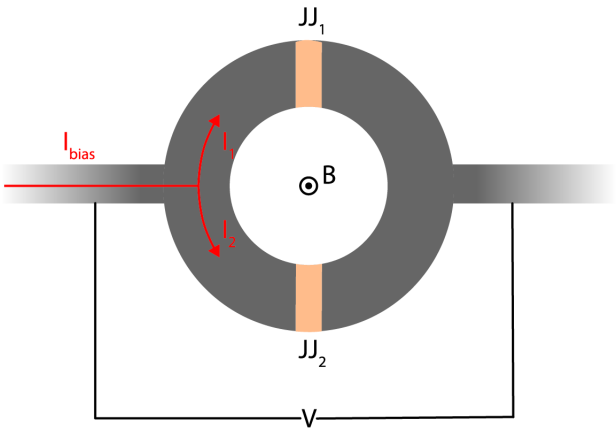

Figure 1.8: Schematic structure of a superconducting quantum interference device (SQUID). Current flows through the two branches. Since the superconducting state is a macroscopic quantum state, the phase is the same for both of them. Once the two current components meet the two junctions, both of them sense a shift of the phase and the following overlap of the two wavefunction, gives rise to the I_c interference pattern as a function of magnetic field passing through the ring.

For the purpose of this thesis, we use this device as a sensitive magnetometer, since the phase of the quantum state of the supercurrent sensitively depends on the external magnetic field. In an overdamped regime, it is possible to set the bias current just slightly above the I_c, and observe that the resulting voltage across the SQUID depends on the external applied magnetic field. More precisely, it depends on the amount of magnetic flux passing through the area of the ring, therefore it is straightforward that the only component of a magnetic field measurable by the device is the one which results perpendicular to the SQUID loop area.

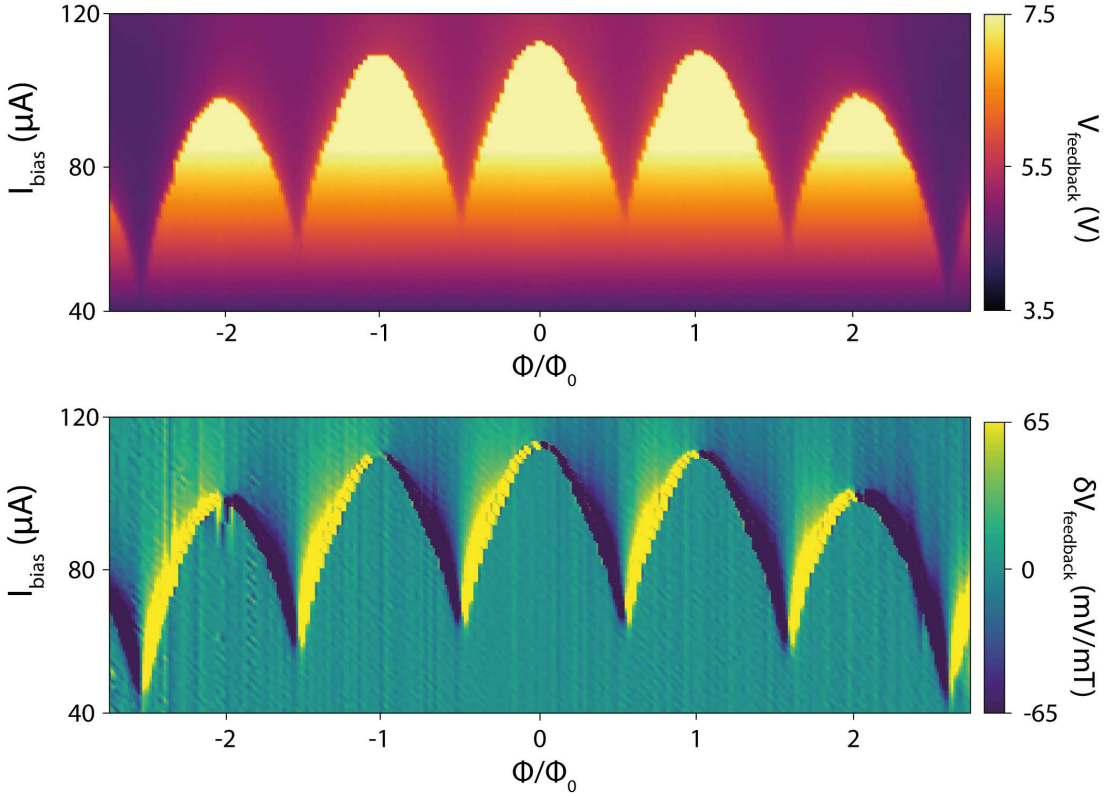

Figure 1.9: The interference pattern of a SQUID characterized in our laboratory and its derivative with respect to Φ. In the second chapter, the characteristic interference pattern will be associated directly to our experimental setup.

Starting from the RCSJ model for a JJ, we extend the concept for a SQUID, which consists of two JJs in parallel configuration. Both of the junctions produce phase shifts (δ_1 and δ_2) of the wavefunction and can be described by the following equations [9]:

$$\begin{cases} \frac{I}{2} + J = I_{c,1}\sin(\delta_1) + \frac{\Phi_0}{2\pi R_1}\dot{\delta}_1 + \frac{\Phi_0}{2\pi}C_1\ddot{\delta}_1 + I_{N,1} \\ \frac{I}{2} - J = I_{c,2}\sin(\delta_2) + \frac{\Phi_0}{2\pi R_2}\dot{\delta}_2 + \frac{\Phi_0}{2\pi}C_2\ddot{\delta}_2 + I_{N,2} \end{cases} \tag{1.19}$$

This form takes in to account the currents through the JJs, which are half of the bias current, J the circulating current flowing through the loop, derived from the London equations (inducing a field which counteracts the external one), and the noise contribution ($I_{N,1}$ and $I_{N,2}$). The other terms represent the supercurrents and the quasiparticle contribution as in eq.1.15. The relationship between the two phase differences is derived by the quantum mechanical probability for the current in a electromagnetic field [11], and since we know the law for the tunnel probability

for the pseudo-wavefunction ($\psi = \sqrt{n_s}\exp(i\delta)$), we can use it to find that:

$$\mathbf{J} = \frac{\hbar}{m^*}\left[\nabla\delta - \frac{q_e}{\hbar}\mathbf{A}\right] n_s \tag{1.20}$$

where n_s is the cooper pair density, and $\mathbf{A}$ is the vector potential. As explained before, both bias currents and induced currents are unable to flow in the inner part of the superconductor because of the Meissner effect. Instead they flow in a thin layer on the surface. It means that the current density $\mathbf{J}$ is zero in the volume enough far from the surface, indeed it is suppressed following the trend given by eq.1.8. At this point, the calculation of eq.1.20 is simplified if we consider the path of the loop where $\mathbf{J} = 0$. Then we can rewrite eq.1.20 as:

$$\nabla\delta = \frac{q_e}{\hbar}\mathbf{A} \tag{1.21}$$

and integrating between the two bias leads we obtain:

$$\int_A^B \nabla\delta \; dl = \frac{q_e}{\hbar}\int_A^B \mathbf{A}d\mathbf{l} \tag{1.22}$$

the wavefunction is a single valued function, then we can calculate the phase shift [12], which emerges between the two SQUID leads as:

$$\delta_1 - \delta_2 = \frac{2\pi}{\Phi_0}\oint \mathbf{A}d\mathbf{l} = \frac{2\pi}{\Phi_0}\Phi_{tot} \tag{1.23}$$

which can be also rewritten as a circuital element for the RCSJ model:

$$\delta_1 - \delta_2 = \frac{2\pi}{\Phi_0}\Phi_{tot} = \frac{2\pi}{\Phi_0}\left(\frac{H_{z,ext}}{\pi R^2} + LJ\right) \tag{1.24}$$

where $H_{z,ext}$ is the magnetic field component perpendicular to the SQUID loop plane, and Φ_{tot} is the entire flux through the SQUID. Explicit in this latest form are also the two main contributions to the total flux. The first one is the external field contribution, while the second is the circulating shielding current, where the inductance term holds the geometrical dependence. In the approximation just exposed, we assume that the branches of the SQUID are wider than the λ of the superconducting material. This is not true when we consider our magnetometer device, since it reaches nanometric dimensions and it works in a regime where the width of the branches is smaller or comparable with the penetration depth. In this case, the inductance term has a rising importance in the phase shift calculation.

In the shown approach, we have considered two perfectly symmetric junctions, avoiding a difference in the current contribution, moreover we are considering the

response in superconducting state, with zero DC voltage contribution, assuming $R \to \infty$ and $C \to 0$. Then the two equations in 1.19 have same parameters and assuming also zero-noise ($I_{N,1} = I_{N,2} = 0A$), and defining the normalized current as $i = I/I_{c,n}$ (with $n = 1, 2$), eq.1.19 can be simplified in the following form:

$$\begin{cases} \frac{i}{2} + J = sin(\delta_1) \\ \frac{i}{2} - J = sin(\delta_2) \end{cases} \tag{1.25}$$

Considering negligible induction ($L = 0$), we can reduce eq.1.24 to $\delta_1 - \delta_2 = 2\pi\phi_a$, with $\phi_a = \frac{2\pi H_{z,ext}}{\Phi_0 \pi R^2}$. Thus, we can rewrite:

$$i = sin(\delta_1) + sin(\delta_2) = sin(\delta_1) + sin(\delta_1 + 2\pi\phi_a) \tag{1.26}$$

and defining $\gamma = \delta_1 + \pi\phi_a$, we can get the following form for the current:

$$i = 2sin\gamma \cdot cos\left(\pi\phi_a\right) \tag{1.27}$$

The phase-dependent highest value for the current is achievable when $sin\gamma = \pm 1$. At the end, the critical current for the SQUID (I_{cc}) is modulated between $2I_{cs}$ and 0:

$$I_{cc} = 2I_{cs} \left|\cos\left(\pi\phi_a\right)\right| \tag{1.28}$$

Fig.1.9 reports an example of the current modulation, as a function of the applied magnetic field, for one of the SQUIDs fabricated in our laboratory. The assumptions introduced in this paragraph are needed as a basic background for the probe used for our measurements, which will be presented in the second chapter. We will consider the effect of the JJs structure, the inductance contribution, and the characteristics of the material used for the fabrication.

1.2 Type II Superconductors

Until now we have assumed the homogeneity of the superconducting state all over the specimen under observation below the critical surface condition, with the only exception given by the exponential decay of the magnetic field at the surface. We saw that this behavior is related to the penetration depth λ. Together with the coherence length ξ, these are the two main parameters, which allow us to predict the magnetic behavior of a superconductor. But the superconductivity can be broken locally under certain conditions. Indeed, until now we described the behavior of Type I superconductors, considering them as a unique homogeneous macro quantum state, which holds for the entire extension of the specimen, excluding the behavior at the surfaces/edges. Before introducing type II superconductors, it is worth considering that, also the type I can present an intermediate state, where it is split in to normal and superconducting domains. This phenomenon is strongly linked to the demagnetization factor, which depends on the geometry of the sample, and the angle at which the external field is applied. It is important to highlight that the Ginzburg-Landau surface energy for the intermediate state is positive. More precisely the length factor $\Delta = \xi - \lambda$ in the surface energy equation:

$$\gamma = \frac{H_c^2}{8\pi}\Delta \tag{1.29}$$

is positive, and it means that the macroscopic pattern is energetically stable.

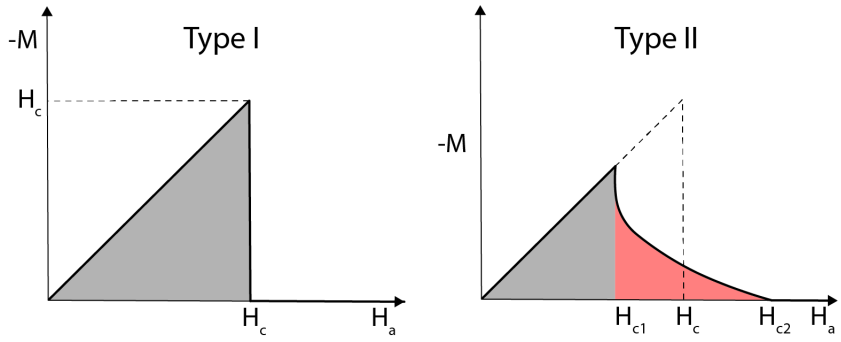

Figure 1.10: The graph on the left represents the magnetization of a virgin state of a Type I superconductor as a function of the applied external field. H_c is the critical field, at which the transition occurs. On the right the same graph for a Type II. H_{c1} and H_{c2} are the lower and higher critical fields, respectively. The gray areas indicate the regime of perfect diamagnetic behavior, while the ref area shows where the mixed state emerges.

It is worth to remark on the previous concept in terms of energy, since a new kind of superconductor presenting a negative surface energy, was discovered in

1935. The most interesting peculiarity of this so-called Type II superconductor is clear if one compares its magnetization curve to the one of Type I superconductor as shown in Fig.1.10. Type II superconductors are able to expel completely the magnetic field below H_{c1} (lower critical field). Once the applied field H_a is larger, one does not see an abrupt transition to the normal state as in a Type I; rather, the magnetic flux starts to penetrate into the inner part of the material in the form of quantized vortices. The right part of Fig.1.10 shows a decrease in magnetization and a higher amount of penetrating flux, until H_a reaches the upper critical field H_{c2}, where the material has a complete transition to the normal state. The upper and lower critical fields for Type II superconductors have the following form [13]:

$$H_{c1} = \frac{\Phi_0}{\mu_0 4\pi\lambda^2}\left[ln(\kappa) + \alpha\right] \tag{1.30}$$

with

$$\alpha(\kappa) = \frac{1}{2} + \frac{1 + ln2}{2\kappa - \sqrt{2} + 2} \approx 0.5 \quad \rightarrow \quad \kappa >> 1 \tag{1.31}$$

and

$$H_{c2} = \frac{\Phi_0}{\mu_0 2\pi\xi^2} \tag{1.32}$$

where $\kappa = \lambda/\xi$ is the Ginzburg-Landau parameter.

1.2.1 Superconducting Vortices

Alexei Alexeyevich Abrikosov first proposed the existence of superconducting vortices in Type II superconductors. The state in which the vortices appear is called the mixed state. In Fig.1.11, we report an example of a measurement of the z-component of the magnetic field H_a penetrating a mixed state of a film of Nb; this is possible since we are using the thin-film approximation, as will be explained afterwards. The distribution of the vortices, their interaction, and their confinement in the material, are studied in detail later in this work. In this sense, it is crucial to remember that this mixed state is strongly dependent on the magnetic history of the sample [14].

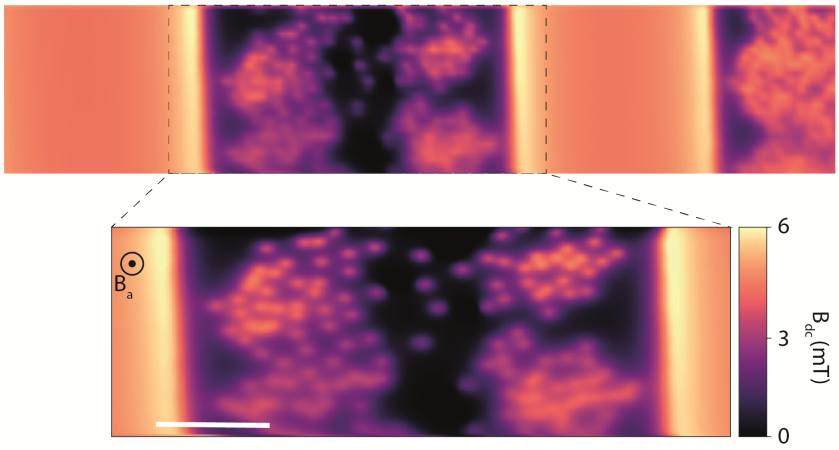

Figure 1.11: Example of a mixed state in a Nb film 150 nm thick, measured with our scanning probe technique (scale-bar 2 μm). $B_a = 4.8$ mT is the external magnetic field, which is applied perpendicularly to the sample surface, while B_{dc} is the magnetic signal measured by our probe. The darkest region represents the Meissner state where the magnetization of the sample counteracts perfectly the effect of the applied magnetic field, while the vortices are distributed on the entire surface of the strip. The superconducting screening effect of the applied field is also clear at the edges of the strip, where the higher intensity of the signal denotes a distortion of the magnetic flux lines.

The Ginzburg-Landau parameter $\kappa = \lambda/\xi$ defines the ratio of the two main characteristic lengths, and tells which type of superconductor is under investigation:

$$\begin{cases} \kappa << 1 & \rightarrow & \lambda << \xi & \text{Positive energy barrier (Type I)} \\ \kappa >> 1 & \rightarrow & \lambda >> \xi & \text{Negative energy barrier (Type II)} \end{cases} \tag{1.33}$$

These relationships describe the decay rate with which ψ_∞ reaches $\psi = 0$ across a superconductor/normal interface. In the first case of eq.1.33, the small penetration depth does not allow the magnetic field to penetrate deep enough inside the superconductor's bulk, and the coherence condition for the Cooper pairs allows the ψ to decay slowly towards the surface. On the contrary a long penetration of the magnetic field (e.g. large λ), works against the coherence of the Cooper pairs and it produces a rapid decay of the ψ function towards the superconductor's surface. The second case produce a negative surface energy, which is the first condition for the mixed state description, and one can think that the local suppression of the superconductivity can produce an arbitrarily small amount of flux penetration. This is forbidden by the the second condition, which defines the minimum amount of magnetic flux which composes each vortex. The fluxoid quantization, through a superconducting ring, has been discussed in Ginzburg-Landau theory,

and is linked to the Abrikosov solution for a periodic magnetic field pattern in a superconductor:

$$F = F_n + \alpha |\psi|^2 + \frac{\beta}{2} |\psi|^4 + \frac{1}{2m^*} \left| \left(\frac{\hbar}{i} \nabla - \frac{e^*}{c} \mathbf{A} \right) \psi \right|^2 + \frac{\mathbf{H}^2}{8\pi} \tag{1.34}$$

where m^* and e^* are respectively the effective mass and elementary charge for cooper pairs, while α and β are the two Ginzburg-Landau phenomenological parameters. We also included the condensation energy, the kinetic energy and the magnetic energy. In the condition of $\kappa > \sqrt{1/2}$, one can calculate the amplitude of ψ, from the GL equation, including the non-linear term. It results in a linear superposition of degenerate solutions of the linearized GL equation:

$$\frac{1}{m^*} \left(-i\hbar\nabla - \frac{e^* A}{c} \right)^2 \psi = -\alpha\psi \tag{1.35}$$

Since, the ψ is expected to be periodic, Abrikosov chose the following form for the order parameter:

$$\psi(r) \propto \sum_n C_n e^{-\frac{n^2\hbar^2}{\xi^2 H_{c2}^2}} \tag{1.36}$$

with C_n, the periodic parameter, which defines the lattice type periodicity in function of the chosen condition (e.g. $C_n = C_{n+1}$ produces a square lattice periodicity). One can impose the stationary condition for the free energy [15]:

$$dF = 0 \tag{1.37}$$

One has to consider that, in eq.1.34 the vector potential $\mathbf{A}$ is a sum of the external field $\mathbf{A}_b$ plus the effect of the supercurrent density $\mathbf{A}_j$, introduced previously. If $\mathbf{A}_j$ is assumed small enough, one can use the current density associated to the unperturbed solution:

$$J_0 = \frac{e^*}{m^*} \left[\psi^* \left(-i\hbar\nabla - \frac{2eA_b}{c} \right) \psi + Const. \right] \tag{1.38}$$

in the from stationary condition:

$$\int \left(\beta |\psi(\mathbf{r})|^4 - \frac{\mathbf{A}_j \cdot \mathbf{J}_0}{c} \right) d^3\mathbf{r} = 0 \tag{1.39}$$

Integrating the eq.1.39, we can obtain the new stationary condition, which depends on the two magnetic field contributions associated with $H_j \to A_j$ and $H_b \to A_b$, and their difference is equal to the difference of the applied field H_a with H_{c2}. As described in [15], if ψ is the eigenfunction for the lowest eigenvalue of the linearized

GL equation, then the current density J_0 corresponds to the superconducting electron density trajectories, identified by the coefficient C_n, introduced above. From this condition, we can obtain the form of the free energy F as a function of H_a:

$$F = \frac{1}{8\pi}\left[H_a^2 - \frac{(H_{c2} - H_a)}{1 + (1\kappa^2 - 1)\,\beta_A}\right] \tag{1.40}$$

with β_A a lattice-dependent coefficient, which is defined in the detailed study [15], and which has to be minimized to obtain the most favorable energy for the magnetic flux distribution. Then, it is possible to deduce the behavior of the magnetization in the superconductor to:

$$M = \frac{H_a - H_{c2}}{\mu_0 \beta_A\,(1\kappa^2 - 1)} \quad \rightarrow \quad H_{c1} < H_a < H_{c2} \tag{1.41}$$

It is possible to summarize few points from this results:

- The magnitude of the magnetization increases linearly with magnetic field.
- The most favorable vortex lattice structure is triangular, which minimize β_A more efficiently, compared to the other lattice patterns.
- In the GL regime, the slope of M is function of κ.
- The magnetic field inside the superconductor changes periodically in space and this periodicity is given by a pattern of fluxoid maxima, corresponding to one quantum flux Φ_0.

As explained above, there exists a minimum amount of flux which is the single quantum flux of a vortex, and it is a derivation of the fluxoid quantization:

$$2\pi n = \frac{2e^*}{\hbar c}\oint \mathbf{A} d\mathbf{l} = \frac{2e^*}{\hbar c}\Phi \rightarrow \Phi = n\Phi_0 \tag{1.42}$$

where n is an integer, and $\Phi_0 \approx 2.1e^{-15}$ Tm^2 is the magnetic quantum flux. Then, the minimum flux scale possible for a single vortex has the lower limit of one Φ_0. It is also interesting to observe how the characteristic length defines the structure of an Abrikosov vortex. In the vortex center, the state is normal and it means that the order parameter is $\psi = 0$, and the magnetic field associated with the quantum flux, $H(r) = \Phi_0/r^2\pi$, has its maximum value covering a core area, whose radius can be approximated as ξ. $H(r)$ decrease exponentially with the radial distance from the core:

$$H(r) = \frac{\Phi_0}{2\pi\lambda^2}\sqrt{\left(\frac{\pi\lambda}{2r}\right)}\exp(-r/\lambda) \tag{1.43}$$

the λ length defines approximately the size of the vortex area (called "electromagnetic region"). For example, in Fig.1.11 the diameter of the measured magnetic field for each vortex corresponds approximately to $2\lambda_{Nb} = 80$ nm. This is a valid estimation only if other factors (e.g. $\lambda(T)$ dependence, the film thickness or material structure) are negligible or not present. One may observe, that in Fig.1.11, the above described periodicity is not clear and it looks like the vortex density and distribution is not homogeneous over the sample. We will consider later the main factors, which can produce a deviation from the regular structure, predicted by Abrikosov.

Pearl Vortices

The previous paragraph mentioned that the diameter of vortices does not always follow the 2λ approximation. Indeed the Abrikosov theory explains faithfully vortices in bulk superconductors, but once the thickness is comparable or lower than λ, then the vortex flux lines are distorted at the film surface. Pearl introduced a theory [16] for thin films in an external magnetic field normal to the film's surface.

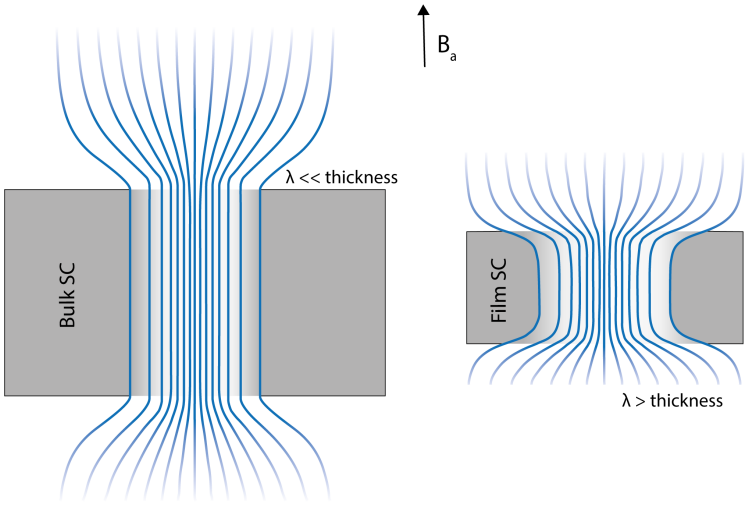

Figure 1.12: On the left, the flux lines are forced on a straight path through the entire thickness of the material. On the right, the thin film condition presents a deviation of the flux lines in the proximity of the surface

Carnerio et al.[14] presented a compete numerical analysis for the dependence of the vortex size on the sample thickness. He found that the lower is the thickness, the more the vortex flux lines radially spread [17]. The most relevant difference with bulk vortices is that the majority of Pearl vortex's energy is associated with

field outside the sample, rather than inside the sample, as with Abrikosov vortices. The B_{vortex} component normal to the film diverges as $\propto ln\,(\lambda/r)$, while in the bulk case the behavior follows $\propto 1/r$, where $r = \sqrt{x^2 + y^2}$. The model used for the magnetic profile description of an isolated Pearl vortex in our experiment will be presented in the third chapter, but Tafuri et al. [18] show a accurate form of this profile with:

$$B_z(k, z) = \frac{\Phi_0 \exp(-kz)}{1 + k\Lambda} \tag{1.44}$$

where $\Lambda = 2\lambda_{x,y}^2/t$ is the Pearl penetration depth, t is the film thickness, $k = \sqrt{k_x^2 + k_y^2}$, and K_x, K_y are the Fourier transformed coordinates in the plane. In this case, the London penetration depth is assumed on its two planar components, since the material is not necessarily isotropic.

The above described phenomenon has strong implications for the vortex distribution, and their interaction between each other, and potential energies present in the sample (e.g. geometric barrier, Bean-Livingstone surface barriers, or pinning centers). In further sections, we will discuss about these effects, which anticipate our result in the third chapter.

1.3 Superconductors in External Magnetic Field

In the previous section the magnetic flux penetration in Type II superconductors was introduced, and how this penetrating flux is quantized in Φ_0. The aim of the work done in the third chapter is the study of the vortex dynamics in MoSi films i.e. the study of the interaction between vortices, and the surrounding potentials. A central role is played by the impurities and defects producing pinning centers, which strongly affect the vortex motion. The nucleation and the expulsion of vortices are tightly bound to these phenomena. The approach to this topic can be done through the study of the global magnetization, considering vortices no more as single quanta of flux, but as a homogeneus magnetization ensemble. In literature, two opposite cases are generally treated: the complete absence of pinning (reversible superconductors), with the consequent free flow and reconfiguration of vortices in the material, and the strong pinning, which obstruct their motion (irreversible superconductors). The second case refers to the Bean Critical State Model, in which one adopts a macroscopic view of the vortices as a magnetic flux ensemble (or bundles [3]). Later, we will mention the model proposed in different works [19], [20] for the magnetic flux and current density distribution in superconducting films, together with the treatment of the edge barriers in a real sample from the Bean-Livingston and the geometric barriers theories. At the end of the section an overview of the trapping potential in terms of free Gibbs energy will be given to describe the vortex confinement in superconducting film strips.

1.3.1 Critical State Model and Remanent State

The Critical State model introduced by Bean [21] does not treat each vortex separately, instead it works with a continuum of electromagnetic front which produces an extra term for the current density in the medium, thus reducing the complexity of the problem. The Bean model assumes that current can exist inside a superconductor far from the surface (in a length bigger then λ). Brand et al. [22] assert that the only way an extrinsic current density can exist in a Type II superconductor is through a gradient of vortex density, like the one shown in Fig.1.13a). The premise of the Bean's model is that, if a superconducting region senses a change in the magnetic field locally, then a shielding current J_c flows there. The model starts from the assumption that no current flows in the virgin state (or Zero Field Cooled state ZFC).

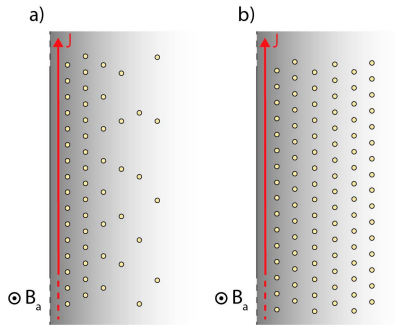

Figure 1.13: Vortices nucleate on the edge of the sample and the current density produces a DC Lorentz force which pushes them towards the center. a) shows the case in presence of pinning centers, while b) is the situation for a pinning-free sample. A vortex (and then a magnetic field) gradient exists in the inner part of the sample only in a).

Then, the initial conditions, for a ZFC initial state, can be translated as:

$$\nabla \times \mathbf{H} = 0 \tag{1.45}$$

since the magnetization of the Meissner effect opposes to the external magnetic field ($\mathbf{B} = \mu_0 \mathbf{M}$), thus:

$$\nabla \times \mathbf{B} = \mu_0 \mathbf{J} \tag{1.46}$$

But Bean's model add the extra condition, which imposes for the current density:

$$\mathbf{J} = \begin{cases} \mathbf{J}_c \rightarrow \text{in region with non-zero magnetic field} \\ 0 \rightarrow \text{in region with ZFC condition} \end{cases} \tag{1.47}$$

transforming eq.1.46 in:

$$\nabla \times \mathbf{B} = \mu_0 \mathbf{J}_c \tag{1.48}$$

A macroscopic justification for this model can be presented assuming a small increase of the external magnetic field, and a consequent transient change in the penetrating flux inside the superconductor. We can assume that inside the material the conductivity behaves like:

$$\sigma \begin{cases} = \infty & for \quad J \leq J_c \\ \neq \infty & for \quad J > J_c \end{cases} \tag{1.49}$$

Considering the region in which $J < J_c$ we have an infinite conductivity, then it results in:

$$\mathbf{E} = \left(\frac{m^*}{4ne^2} \right) \frac{\partial \mathbf{J}}{\partial t} \tag{1.50}$$

then, using Faraday's law, and considering the ZFC initial conditions of $\mathbf{B} = 0$ and $\mathbf{J} = 0$ in the sample, we get:

$$\mathbf{B}(t) = -\left(\frac{m^*}{4ne^2}\right)\nabla \times \mathbf{J}(t) \tag{1.51}$$

Eq.1.46 and 1.51 recall the London's equations for $J < J_c$, but once the field penetrates, then $J > J_c$ and the equations are no longer satisfied. Indeed for such condition we have a finite σ and the current decays as in a normal metal until it becomes equal to its critical value J_c, since it is the maximum value for which $\sigma = \infty$. A further increase in magnetic field corresponds to a redistribution further towards the inside of the superconductor of the magnetic flux, and consequently a redistribution of the current density. Is is worth to highlight that in the Bean theory the current density is a two level function (0 or J_c are the only allowed value). This is important since is related to the sample structure itself. In thin film geometry the distribution of the current density (and consequently of the magnetic field) follows a more complex behavior [20][19].

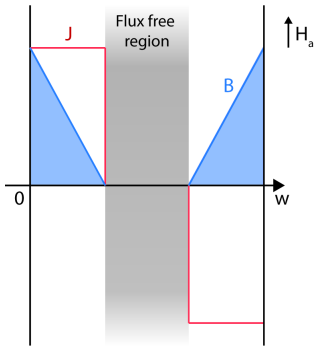

Figure 1.14: The image present a typical example of the current density J and magnetic field B behavior in the Bean's model in a sample of width w. In the case reported, the applied field H_a is much lower then the higher critical field H_{c2}, but higher then H_{c1}, therefore the magnetic field starts to penetrate in form of vortices, which nucleate from the edges.

Once a initial minimum value of magnetic field penetrates the superconductor a shielding current density emerges. Since the magnetic field penetrates in form of quantized vortices, the current density induces a Lorentz force which pushes vortices towards the inner part of the material. In the Bean model, this motion is hindered by pinning centers in the material. For the sake of simplicity we assume an homogeneous distribution of them (which in the majority of cases is not consistent with experimental conditions, like will be shown in the third chapter). In the case of ideal free-pinning material, one can deduce that the flow of vortices from

the edges to the center would completely fill the material volume, and it would stop only when the vortex-vortex repulsion potential becomes strong enough and the vortex pattern would become hexagonal to minimize the energy. The strong implication is that the critical current density depends not on the superconducting material itself but on the defect structure. Indeed, their structure can produce a significant difference between the highest possible J_c, and the depairing current density J_d. As reported by Arcos et al.[23], J_c is significantly lower than J_d, and it finds its maximum vale for columnar defects. Therefore, in the superconductor, for any value of magnetic field exists a balance relation between the the Lorentz force, which is produced by J_c, and pushes vortices towards the center of the specimen, and the pinning forces, which oppose to the vortex motion. Since both of these forces are finite, it is possible to write the relationship:

$$\mathbf{F}_L = \mathbf{J}_c \times \mathbf{B} = -max\left[\mathbf{F}_{pinning}\right] \tag{1.52}$$

It is worth to point out that the analysis presented until now does not take in to account the vortex dynamics, instead it deals with equilibrium states for certain values of **J** and **B** under geometric and structure conditions.

1.3.2 Thin Film Model

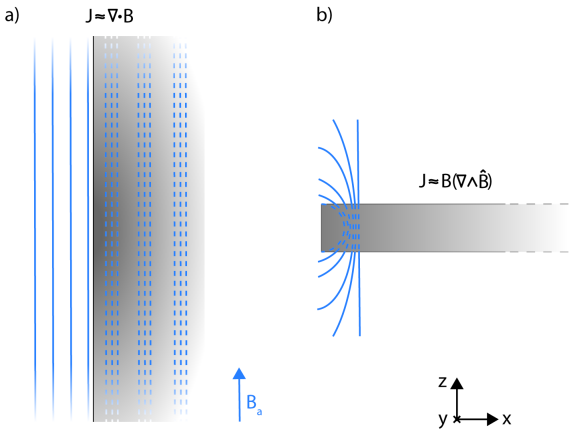

Figure 1.15: The figure reports the near-edge cross-section of a slab specimen a), and a thin film b). In the first case, the field gradient term is dominant and the flux lines are parallel to the sample edge. In the second case the tangential components outside the sample are contributing strongly giving rise to the curvature term in eq.1.53.

Before going through the implications of the Bean's model on the magnetization, relative to the vortex inside the material, it is necessary to introduce a model

for a different case than Bean's. Until now, the boundary conditions have been quite restrictive, i.e. thickness much larger than the width (or radius in case of a cylinder) of the sample, or the assumption of no dependence of the current density on the magnetic field; this regime can be called parallel geometry (PG), since is assumed that the external field is applied parallel to an ideally infinite or very large thickness, following the condition $\lambda << t$. A thin film model needs to be introduced also in regarding of the sample measured for our purposes. Brandt et al.[24] introduced an analytic model for thin film geometry, and later Zeldov et al.[19] presented a comparison between the magnetization in the thin film model and the thick slab one. Moreover, McDonald et al.[20] provided a critical-state model for the thin film, based on the field-dependent current density, emphasizing the hysteresis behavior for Type II superconducting thin films, which require a numerical approach. In the thin film model, the applied field is assumed to be perpendicular to the strip plane, i.e. normal geometry (NG). One of the main differences between PG and NG is the vortex structure. In the first case the vortex cylindrical core is parallel to the sample edges, instead in the second case the flux lines are curved because of the strong demagnetizing effects. This is clear if one considers:

$$\nabla \times \mathbf{B} = \mu_0 \mathbf{J} \rightarrow (\nabla B) \times \hat{\mathbf{u}}_B + B\,(\nabla \times \hat{\mathbf{u}}_B) = \mu_0 \mathbf{J} \tag{1.53}$$

with $\hat{\mathbf{u}}_b = \mathbf{B}/B$. The rewritten Ampere's law eq.1.53 shows the contribution of the magnetic flux density (∇B) and the curvature of the field lines in the material ($B\,(\nabla \times \hat{\mathbf{u}}_B)$). The vortex-transverse contribution also produces modifications in the resulting magnetic and current profile of the critical state model. At the end of this chapter, we will also observe the strong dependence of the flux lines' curvature on the vortex position in a superconducting strip and how this effect is enhanced by the edges. Both the previous cited approaches (numerical and analytic) start from considering the system in a virgin state. A perfect Meissner state, where the current shields the external field completely except for a small region of the same scale of λ. The perfect screening holds only if the condition of $\lambda < t < W$ (or $t < \lambda < \Lambda < W$) exists; where t is the film thickness, $2W$ is the film width and Λ is the Pearl penetration depth. Using the conformal mapping method [25], and referring the coordinate system in Fig.1.15 b), one obtains:

$$J_y(x) = -\frac{2B_a x}{\mu_0 t\sqrt{W^2 - x^2}} \tag{1.54}$$

$$B_z(x) = \begin{cases} 0 & \rightarrow \quad |x| < W \\ \frac{B_a|x|}{\sqrt{x^2 - W^2}} & \rightarrow \quad |x| > W \end{cases} \tag{1.55}$$

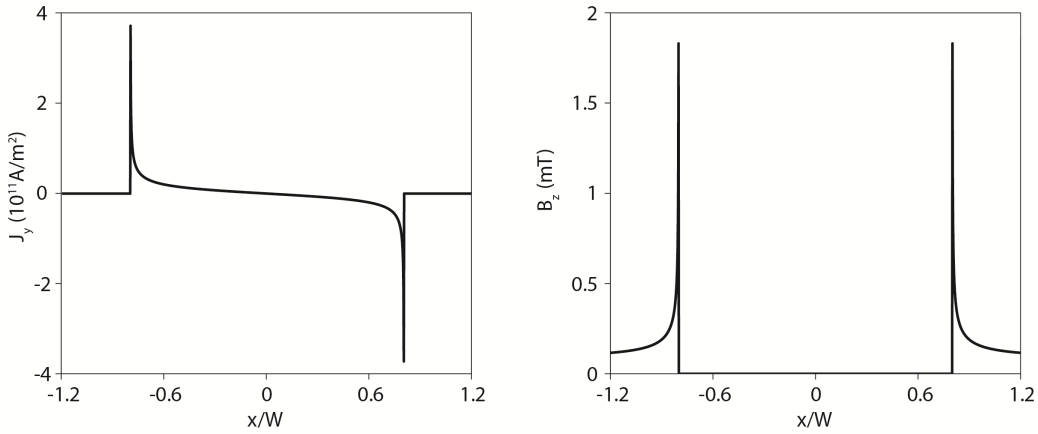

Figure 1.16: An example of current density (left) and magnetic field (right) profiles are reported for a complete screening Meissner state. Both are calculated with eq.1.54 and 1.55, using values for applied field $B_a = 1$ mT, thickness $t = 65$ nm and width $W = 9.8$ μm taken from the MoSi measurements in the third chapter. It should be pointed out that, we obtain this magnetic profile starting from the zero field cooling condition for thin films. Further in the third chapter, one can note a disagreement with some results taken at the same B_a, but it has to keep in mind that our results start from a study of field cooling condition.

The numerical model now requires us to find a form for $J_c(x)$ and $B_z(x)$, which takes in to account the dependence $J_c[B_z(x)]$, with x the coordinate parallel to the width of the film. The form of these two functions was presented by Mikheenko and Kuzovlev [26] and depend on a weight function $G(s, B_a)$, whose normalization (eq.1.56) is linked to the condition of zero-flux in a region of $|x| < a$, where a is the x value that defines the region, in which a complete screening exists. Therefore, the regions in $a < |x| < W$ allow the magnetic field penetration, while for $|x| < a$, the Meissner state persists.

$$\int_a^W G(s, B_a) ds = 1 \tag{1.56}$$

This normalization condition leads to the constitutive relationship between the applied field and the parameter a:

$$a = \frac{W}{\cosh(B_a / B_{scale})} \tag{1.57}$$

where

$$B_{scale} = \frac{\mu_0 t J_c|_{B_a=0}}{\pi} \tag{1.58}$$

is the characteristic field related to the geometry [19]. Merging the Mikheenko and Kuzovlev form for the current density and the condition of dynamic equilibrium for the flux inside the superconductor, one can obtain a Volterra equation for the weight function:

$$G(x, B_a) = -\frac{B_a}{B_{scale}} \frac{d}{dx} \int_x^W \frac{ds}{\sqrt{s^2 - x^2}} \left[\frac{J_c(B_z(s))}{J_c|_{B_a=0}} \right] \tag{1.59}$$

with s the integration variable. Replacing $G(s, B_a)$ in the Mikheenko and Kuzovlev equation, the current and magnetic field are defined as:

$$J_y(x) = \begin{cases} -\frac{2}{\pi} x \sqrt{a^2 - x^2} \int_a^W \frac{J_c(B_z(s))}{(s^2 - x^2)\sqrt{s^2 - a^2}} ds & \rightarrow \quad |x| < a \\ -\frac{x}{|x|} J_c(B_z(s)) & \rightarrow \quad a < |x| < W \end{cases} \tag{1.60}$$

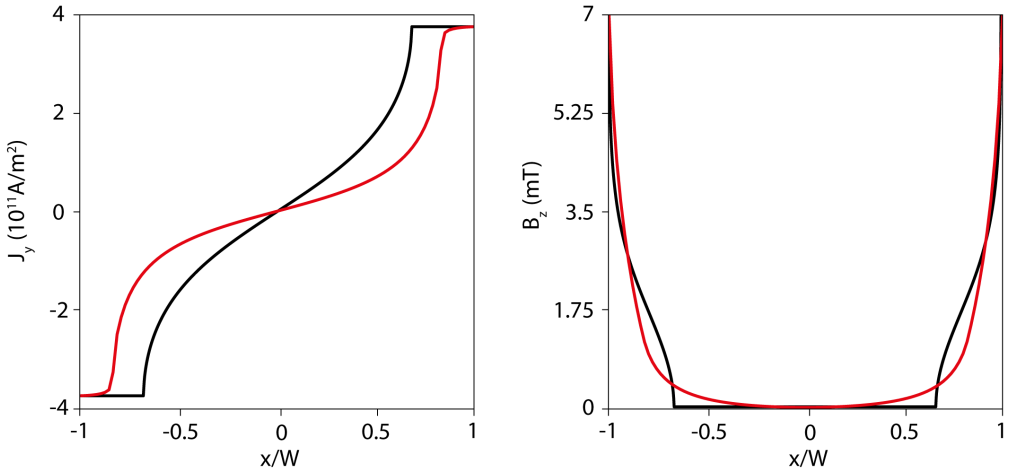

Figure 1.17: The current density (left) and magnetic (right) profiles, for both numerical (red) and analytic (black) calculation. Where W is the total width of the superconducting film and $B_a = 4$ mT.

$$\begin{aligned} B_z(x) &= B_{scale}|x|\sqrt{x^2 - a^2} \times \\ &\times \int_a^W \frac{ds}{(x^2 - s^2)\sqrt{s^2 - a^2}} \frac{J_c(B_z(s))}{J_c|_{B_a=0}} \quad \rightarrow \quad a < |x| \neq W \end{aligned} \tag{1.61}$$

The solution of this last integral equation can be achieved by numerical methods, but if we assume no field-dependent current density $J_c|_{B_a=0} = J_c(B_z(s))$, then, it is possible to obtain the analytic result for the equations for $J_y(x)$ and $B_z(x)$

presented in [19]. We can compare the numerical and analytic results reported in Fig.1.17, where one can observe the differences between the magnetic and current density profiles in the superconducting film. In the numerical case we considered the Kim model for the dependence of J_c from $B_z(x)$:

$$J_c(B_z(x)) = \frac{J_{c,0}B_0}{B_0 + |B_z(x)|} \tag{1.62}$$

where $J_{c,0}$ is the zero-field critical current density, and $B_0 = B_z(x)$, when $J_y(x) = J_{c,0}/2$, [27]. In the analytic case, we assume the thin film approximation, in which the current distribution can be assumed constant through the entire thickness.

External Current Density Contribution

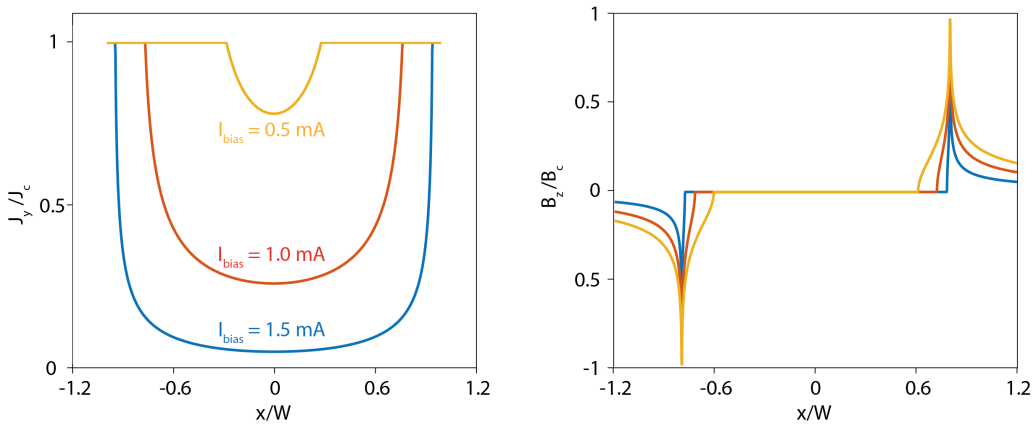

Figure 1.18: The graphs report the magnetic and current density profiles for a thin film superconductor with an applied bias current. The three profiles reported as examples are given with a bias current I_{bias} of $0.5 - 1.0 - 1.5$ mA. No external magnetic field is applied.

The presence of a bias current produces an asymmetric change in the current and field profiles. The equations which describe the contribution from a bias current I_{bias} are [24]:

$$j_y(x) = \begin{cases} \frac{2j_c}{\pi} arctan\left(\frac{u^2-b^2}{b^2-x^2}\right)^{1/2} & \rightarrow \quad |x| < b \\ j_c \quad \rightarrow \quad b < |x| < u \end{cases} \tag{1.63}$$

and

$$B_z(x) = \begin{cases} \frac{\mu_0 H_c x}{|x|} arctanh\left(\frac{x^2-b^2}{u^2-b^2}\right)^{1/2} & \rightarrow \quad b < |x| < u \\ \frac{\mu_0 H_c x}{|x|} arctanh\left(\frac{u^2-b^2}{x^2-b^2}\right)^{1/2} & \rightarrow \quad |x| > u \\ 0 \quad \rightarrow \quad |x| < b \end{cases} \tag{1.64}$$

with $b = u(1 - I_{bias}^2/I_{max}^2)$, $u = W/2$, $I_{max} = 2j_c u$ and $H_c = j_c/\pi$. In this context, the lowercase j stands for the sheet current density, used in the thin film approximation. This is a consequence of the assumption of constant $j_y(z)$ through all the thickness. In our study on pinning centers, we used both DC and AC currents bias to apply an extra term of the Lorentz force besides the one due to the Meissner screening effect. In case of an AC current the modulation of the force produces an oscillation of the magnetic flux in form of vortices, around an equilibrium position, which corresponds to the minimum of the potential energy of the pinning sites. In case of a DC current, depending by the amplitude is possible to force the flux close to one edge of the film and even to expel it above a certain threshold.

1.3.3 Magnetization Curve and Interpretation

Now that the critical state model and the analytic model of **J** and **B** are given, it is possible to follow the magnetization path of a superconductor under the effect of an external magnetic field. For this purpose, we use Fig.1.19 as reference to describe the hysteresis loop. Starting from a virgin state condition, once the field starts to increase, Meissner currents completely shield the sample and the magnetization M increases linearly with an ideal slope of $1/(4\pi)$ with B_a (in the real, case the Meissner slope is strongly dependent on the sample geometry). The slope starts to lose its linearity once B_{c1} is reached, and the magnetic flux starts to penetrate the specimen from the edges. We assume the ideal case in which the flux penetration process starts at the B_{c1}. In the real case, however, one has to consider also the contribution of other factors like the edge barriers. Such barriers can induce a higher value of the penetration field. Since the magnetic flux penetrates the sample, M decreases due to the decreasing demagnetization effect. Increasing further B_a the vortex density increases, but more slowly since the vortex-vortex repulsion has a rising contribution, and in the inner side of the sample, the quantized vortices try to self-reconfigure in a pattern with the minimum energy (which depends on the pinning potential distribution). Once $B_a = B_p$, the flux fully penetrates the film width, with $B_p \propto \mu_0 J_c/t$ the full-penetration field.

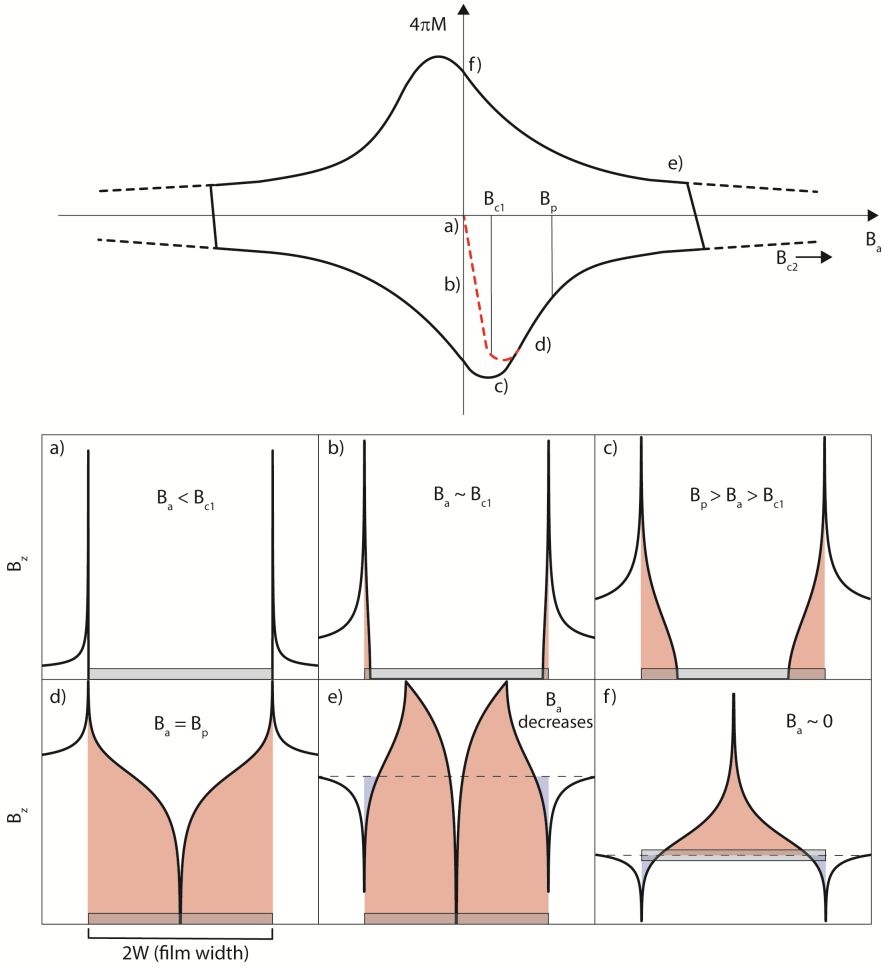

Figure 1.19: A magnetic hysteresis loop is given as example. The gray rectangle in each graph represents the film sample, while the blue and red shaded regions stand for the positive and negative magnetization contribution respect the external field sweep direction. On the loop path are highlighted the main points for the thin film behavior under the effect of a sweeping B_a. a) represents the complete shielding sate (starting from a virgin state). Increasing the field below B_{c1}, the flux weakly starts to penetrate from the edges b). Once $B_a = B_p$ the flux reaches the center of the specimen d). The change of the external field sweep direction generates an opposite current density which produces a magnetic moment with opposite direction from the edges e). At $B_a = 0$ T the field trapped inside the thin film corresponds to the remnant magnetization f), [28].

This field also defines the end of the virgin magnetization curve which is obtained with the zero field cooling technique. It can also be read as a bifurcation point between the virgin curve and a the envelope of the magnetization hysteresis loop. Let's assume that, after a certain value of $B_{c2} > B_a > B_p$, the external field is

reduced. This abrupt variation induces a current density with opposite orientation for a thin surface at the edges. This surface increase quickly but linearly in a reverse slope with the decrease of B_a (called Meissner slope), and crosses the 0 of magnetization, as one can see at the point e) in the magnetization loop in Fig.1.19. It means that the magnetic moments of both positive and negative current densities are balanced. In Fig.1.19 the two opposite magnetization contribution are represented by the blue and red regions. At $M = 0$ T the area defined by these two region is the same. At $B_a = 0$ T the trapped field corresponds to the remnant magnetization [28]. This surface increase quickly but linearly in a reverse slope with the decrease of B_a (called Meissner slope), and crosses the 0 of magnetization, as one can see at the point e) in the magnetization loop in Fig.1.19. It means that the magnetic moments of both positive and negative current densities are balanced. In Fig.1.19 the two opposite magnetization contribution are represented by the blue and red regions. At $M = 0$ T the area defined by these two region is the same. At $B_a = 0$ T the trapped field corresponds to the remnant magnetization [29].

Field Cooling and Zero Field Cooling

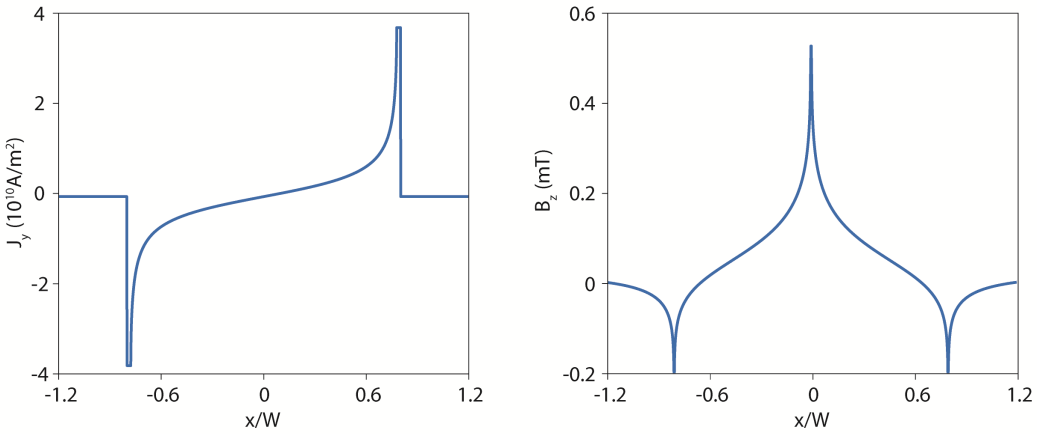

Figure 1.20: The graphs report the magnetic and current density profiles for a thin film superconductor initialized with FC technique at 1 mT.

For the purposes of this work, it is relevant to highlight how the zero field cooling (ZFC) and field cooling (FC) techniques were used in our experiment. ZFC was used only to recreate the virgin conditions for the magnetization transport measurements, to confirm the J_c in our sample [30]. Instead, the magnetic maps were measured after a FC initialization, with the exception of the Fig.1.11, where the

mixed state was obtained by classically increasing B_a. In FC case, the magnetization (and then the vortex density) is expected to be identical compared to the measurements done following the hysteresis loop (passing through the complete flux penetration state) from a ZFC initial condition, as shown by Koblischka et al. [31]. The field cooling initialization was used to initialize the mixed state at field values lower than the B_{c1}, which means that the flux trapped during the process is distributed in a close relationship with the pinning center distribution, indeed one main focus of our work was to observe the pinning distribution in the amorphous MoSi. This also explains why in the magnetic maps, reported in the third chapter, do not display any long-range order, and the vortex distribution appears random. In such a regime, the vortex nucleation has a strong dependence on the pinning potential, but (as will be shown later) the linear relation of the vortex density and the external applied field is still valid.

1.4 Potential Barriers and Thermal Motion

Until now the magnetic flux, penetrating the superconductor, has been studied in equilibrium or semi-equilibrium after or before changes of boundary conditions. We assumed that vortices are confined in their pinning potentials, but their dynamics are more complex and other factors have to be considered, such as thermal motion activation or tunneling phenomena. The thermal energy contribution has an important role for the purposes of this study, and it has to be considered for the effects of the slow energy relaxation, and the influence on the vortex dynamics. Moreover, this effect may produce a strong dissipation contribution, due to the thermally activated hopping of flux lines among different pinning potentials. Nevertheless, has to be considered the confinement of the vorteices motion, which arises from the sample boundaries. In the following sections we will present all the possible potentials which can confine and trap the vortices inside of a specimen, explaining which one of them have an influence on the sample that we have investigated.

1.4.1 Surface Barrier Contributions

The flux penetration and expulsion from a thin superconducting film follow the previously described magnetization loop. From that hysteresis loop we deduce some useful parameters in order to set up various phases during the external field sweep. One of them is B_{c1}, i.e. the field value at which the magnetic flux starts to penetrate the film edges. However, most vortex penetration occurs at higher or lower fields, as some side effects need to be considered in the analysis. The main factors are:

- Bean-Livingstone Barrier
- Geometrical Barrier
- Structural fabrication damage

In our analysis, we assume the last element to be negligible, while the first two play central roles for the vortex entrance delay. Due to the above mentioned FC trapping technique, one can find a concentration of flux (i.e. then vortex density) in the middle of the superconducting film, but is also important to consider whether the geometrical barrier or the Bean-Livingstone barrier can be ignored or not in the analysis.

Bean-Livingston Barrier

Bean and Livingston [32] claim that the superconducting specimen surface may be partly responsible for low-field hysteresis behavior, even in the case of an ideal defect-free sample. The core of this analysis involves two force contributions for vortices close to a specimen surface. One is the repulsive force, due to the shielding current density, induced by the external field, which gives an energy contribution:

$$E(x) = \Phi_0 B_a e^{-x/\lambda} \tag{1.65}$$

where x is the distance vortex flux from the sample edge. The second one is an attractive force towards the surface depending on the vortex-surface distance. This is produced by an image vortex with the opposite sign outside the sample, leading to the energy relation:

$$E(x) = \epsilon_v - \left(\frac{\Phi_0}{\lambda}\right)^2 \mathbf{K}_0 \left(\frac{2x}{\lambda}\right) \tag{1.66}$$

with $\epsilon_v = (\Phi_0/4\pi\lambda) log(\lambda/\xi)$ the vortex-line energy [3], x the vortex distance from the surface, ξ the coherence length, and $\mathbf{K}_0$ a Bessel function of the second kind [32]. It is possible to observe that the image term decreases exponentially for distances greater then ξ from the surface. Then, this energy relation describes an energy barrier which has a rising importance for fluxons close enough to the superconductor surface, while in $x >> \lambda$ situation, the repulsive term is dominant.

Geometrical Barrier

While the Bean-Livingston barrier is generated by the attraction of the penetrating flux to the sample surface (or edges in the case of thin films), the geometrical barrier is tightly related to the sample geometry as previously introduced. It means that the magnetic flux senses an extra energy term, which opposes the vortex penetration and is proportional to the demagnetization factor of the sample cross section [33]. This contribution affects the magnetic penetration field, which does not occur anymore at B_{c1} but at higher fields. As shown by Benkraouda et al.[34], the smoothness of the sample edges for a specimen affects strongly the curvature of the vortex flux lines, as a function of the distance from the surface. Similarly to the Bean-Livingston barrier case, it can be written in one-dimensional case:

$$E(x, B_a) = \epsilon_v l(x) - W(x, B_a) \tag{1.67}$$

where $l(x)$ is the length of the vortex flux line through the sample thickness,and $W(x, B_a)$ is the work done by the Meissner current to push a vortex from the edge

to a certain x distance inside the sample. All the dependency from the cross-section is carried by the $l(x)$ term and the recently described geometrical barrier due to thin flat geometry of the sample. Because of this dependence, the geometrical barrier becomes less relevant when the film reaches a thickness (t) much smaller than the penetration depth. Indeed this is the case reported in the third chapter for the MoSi experiment, where $t << \lambda$. Anyway, it is interesting to show the deviation of the vortex penetration magnetic field from the B_{c1} value, following the analysis proposed in [33].

$$B_p = B_{c1} \tan\left(0.36\frac{t}{W}\right) \sim 58mT|_{MoSi} \tag{1.68}$$

which gives for our case a demagnetizing factor $N_{deg} = 0.0512$. Unfortunately as already mentioned, in our case is not possible to apply the proposed model for the calculation of the reversible field,

$$B_{rev} = B_{c1}\left[0.65 + 0.12ln\left(\frac{t}{W}\right)\right] \tag{1.69}$$

since our sample exceeds the limiting condition of $t/W << 1$ (in our case the ratio is 0.0073).

Kuit Model

Through the development for the two energy barrier contributions, we just saw that, while the Bean-Livingstone barrier scales proportionally to λ, the geometrical barrier (which scale proportionally to t) can be neglected hereafter. In order to introduce an energy profile which can describe our experimental framework, it is useful to follow the model introduced by Kuit et al. [35] [36], where the Gibbs free energy form is used to define the one-dimensional energy function for a certain applied field, perpendicular to a thin film, sensed by a vortex in the film:

$$G(x) = \frac{\Phi_0^2}{2\pi\mu_0\Lambda} ln\left[\frac{3W}{\xi} sin\left(\frac{\pi x}{2W}\right)\right] \pm \frac{\Phi_0\left(B_a - n\Phi_0\right)}{\mu_0\Lambda} x(2W - x) \tag{1.70}$$

where n is the vortex density proportional to B_a, W is the film width, and Λ is the Pearl penetration depth. While the first term (self-energy term of a vortex) is independent of the applied field, the second term refers to the vortex-shielding current interaction, which depends on B_a. The first term can be associated to the Bean-Livingstone barrier and indeed it has a dome shape, and it decreases once $x \to 2W$ or $x \to 0$. Then, the work necessary to force a vortex from outside into

the thin film inside the superconductor, increases monotonically with the distance from the edges.

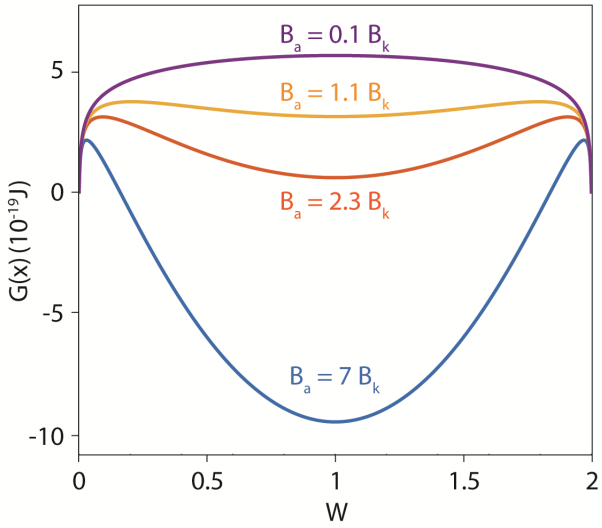

Figure 1.21: Four different potentials sensed by a single vortex in the MoSi strip with width $W = 8.9$ μm. The four cases represent four different stability conditions respectively$B_a \approx 7B_k, 2.3B_k, 1.1B_k, 0.1B_k$, with $B_k = 1.65\Phi_0/W^2$ the Kuit critical field [35]. Increasing the applied field, the potential becomes deeper and is less probable for the vortex to be expelled out from the film. It can be noted that thermal fluctuations become more relevant when the applied field is closer to B_k

1.4.2 Flux Creep

The critical state equilibrium described through the relation given by eq.1.52, does not take into account the thermal energy contribution. As mentioned above, the pinning force depends mainly on the material properties. The $J_c(B_a = 0)$ reaches only 20% of the depairing current density for the Cooper-pairs [23]. A further error in the $J_c(B_a = 0)$, is given by thermal activation processes. Anderson and Kim [37] proposed a model for the thermal activated jump of a vortex from its pinning potential U_p. Thermal energy produces an instability in the vortex position which can eventually lead it to climb over the potential wall. This probability is proportional to the Boltzmann formula $exp(-U_p/k_BT)$, which sets the jumping rate. This rate assumes an equiprobability in the jump direction, but if a current J is applied, an asymmetric contribution $U_p[1 \pm J/J_c|_{B_a=0}]$ emerges in the direction

of the Lorentz force:

$$R_- - R_+ = 2e^{-\frac{U_p}{k_B T}} sinh\left(\frac{JU_p}{J_c|_{B_a=0} k_B T}\right) \tag{1.71}$$

where R_- and R_+ are the jump rates for the two opposite direction for a negative and a positive Lorentz force:

$$R_- = e^{-\frac{U_p\left[1-\frac{J}{J_c|_{B_a=0}}\right]}{k_B T}} \tag{1.72}$$

$$R_+ = e^{-\frac{U_p\left[1+\frac{J}{J_c|_{B_a=0}}\right]}{k_B T}} \tag{1.73}$$

If we multiply the eq.1.71 for the material resistivity after the transition (ρ) and $J_c|_{B_a=0}$, we can obtain the electric field, which depends on the energy ratio between the pinning energy U_p and the thermal energy $k_B T$. We can distinguish two different cases. If the thermal energy is comparable to the pinning potential ($U_p << k_B T$), then the *sinh* in eq.1.71 can be assumed linear (since J cannot be higher than $J_c|_{B_a=0}$), and the electric field depends linearly on the current density, obtaining the so-called flux creep:

$$E(J) = 2\rho J \frac{U_p}{k_B T} e^{\frac{U_p}{k_B T}} \tag{1.74}$$

whereas, if the thermal energy is much lower than the pinning potential, the negative exponential of $sinh(x) = \frac{e^x - e^{-x}}{2}$ is negligible, and we can write:

$$E(J) = \rho J_c|_{B_a=0} e^{-\frac{U_p}{k_B T}} e^{\frac{U_p J}{k_B T J_c|_{B_a=0}}} \tag{1.75}$$

with ρ the material resistivity in normal state. The flux creep regime neglects the hopping against the Lorentz force in the first case, while a thermal contribution becomes more relevant in the opposite limit, indeed the pinning potential is comparable to the thermal energy. In the result reported in next chapters will be presented the effect of an AC and DC current contribution in a thermal activated regime, for the vortex hopping.

Experimental Setup

2.1 Introduction

This chapter introduces the experimental setup used to perform our measurements and the tools that we need to achieve the magnetic maps, presented in the third chapter. First, an overview of the measurement setup and the electronic components used to readout the probe signal is given. In the second part, the focus moves to the scanning probe technique itself, starting from what was already introduced in the first chapter for a generic SQUID. An example of measurement procedure is presented.

2.2 Cryostat and Microscope

Fig.2.1 reports an overview of the the main tools, which allow us to perform the measurements presented in the third chapter. The core of the microscope is placed in a ^{4}He cryostat. The entire cryostat is fixed in the center of an optical table sustained by a system of three supports, which allow to isolate the system from low frequency mechanical vibrations. At the bottom of the cryostat, a superconducting magnet is installed, and it is able to produce a DC magnetic field along the z axis up to ± 6 T. A picture of the entire structure of the probe is reported in Appendix E at 4.5, and it consists in 1.3 m of stainless-steel tube, which ends in a copper flange at which the microscope is bolted Fig.2.3(c). The copper flange of the low-temperature end of the tube, was designed to provide the microscope thermal contact in the liquid-^{4}He bath. A cylindrical stainless-steel can is sealed with Indium on this flange, ensuring a high-vacuum environment for the scanning probe apparatus. The top part of the tube is the room-temperature side, which

is composed of different flanges with electrical feedthroughs, which reach the top part for the entire tube's length.

2.2.1 Block Scheme

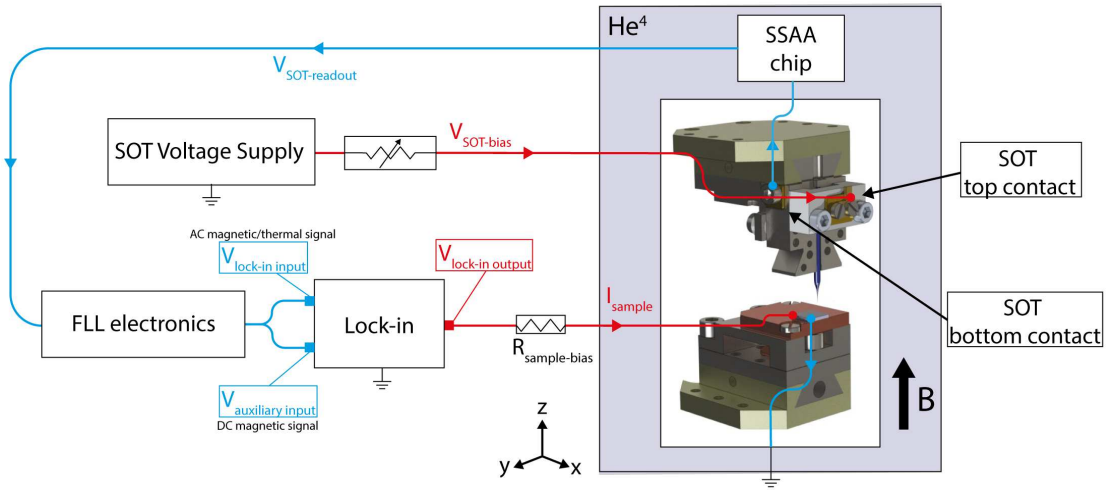

Figure 2.1: Experimental setup schematic. The input signals with respect to the sample-probe system are reported in red, while the outputs are reported in blue. The voltage output of the lock-in generates an AC current across the bias resistor, which is sent to the sample. The SQUIDs series array amplifier (SSAA) collects the measured SOT signal, and amplifies it through a feedback loop control (flux locked loop circuit: FLL). Finally, the AC component of the signal is demodulated by the lock-in input, while the DC component is sent through an auxiliary input of the lock-in.

The readout setup is summarized in Fig.2.1. A DC power supply (Yokogawa GS200) is used to send the bias current (I_{bias}) through the SQUID. The SOT senses the variation of the magnetic field over the sample, by the change of flux through the SQUID loop. This signal is sent through a DC SQUID series array amplifier (SSAA) chip, which is connected to a feedback circuit, more precisely a flux locked loop (FLL). FLL and SSAA amplify the SOT signal before sending it as input in the lock-in. The DC component of the SOT signal is sent to the lock-in auxiliary input, while the AC signal is demodulated through the lock-in input at the same frequency of the AC current sent through the sample from the lock-in output. The usual frequency range used for the AC measurements is $3-10$ kHz. The SSAA has an input sensitivity of $23\mu A/\Phi_0$ and a current noise of 10 pA/$\sqrt{Hz}$ at $4K$, while the FLL electronics has an analog output range of $\pm 13V$.

We have used a MFLI 500 kHz/5 MHz lock-in amplifier produced by the Zurich Instruments.

In this block scheme, we do not report the latest upgrade we developed for our probe, since it was not used for the results presented in this thesis. It consists in the coupling of the SOT probe with a qPlus mechanical resonator. Setup explanation and a measurement example are reported in Appendix H at 4.8.

2.2.2 Microscope Structure

The microscope structure is reported in Fig.2.3. Four non-magnetic springs hold the entire microscope structure, improving the vibration isolation and thus reducing the noise floor. The titanium core is encased in a set of copper plates, which, together with four soft copper braids, provide a good thermal coupling with the top copper flange, that is welded at the end of the cryostat probe. Indeed, this copper flange is in direct contact with the liquid ^{4}He in the cryostat. As explained in Fig.2.3(b), the copper frame holds the titanium core, on which one piezo motor set is mounted. We chose titanium due to its low response to magnetic fields and its negligible thermal contraction, which helps to not lose the SOT-sample alignment upon cool-down. The movement during the scanning measurements is performed by the sample, while the SOT stands at a fixed position. Through a PC self-programmed software interface, the scanner motion of piezo-stacks is controlled via 3 analog voltage outputs of a dedicated National Instrument 16−bit DAQ card.

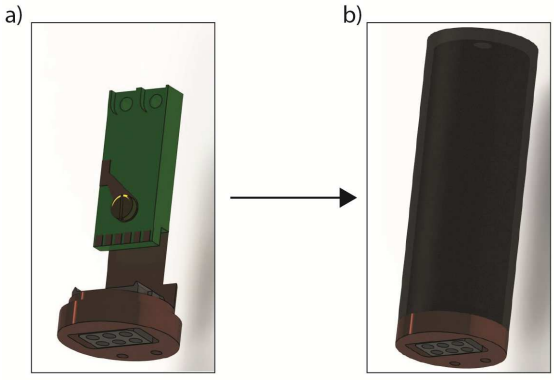

Figure 2.2: The SSAA chip is fixed on a copper support to boost the thermal coupling a). A cylinder of niobium cover the SSAA, in order to shield the SQUID array chip from external fields, since the Nb is superconductive at 4.2 K, and then it shows a perfect diamagnetism.

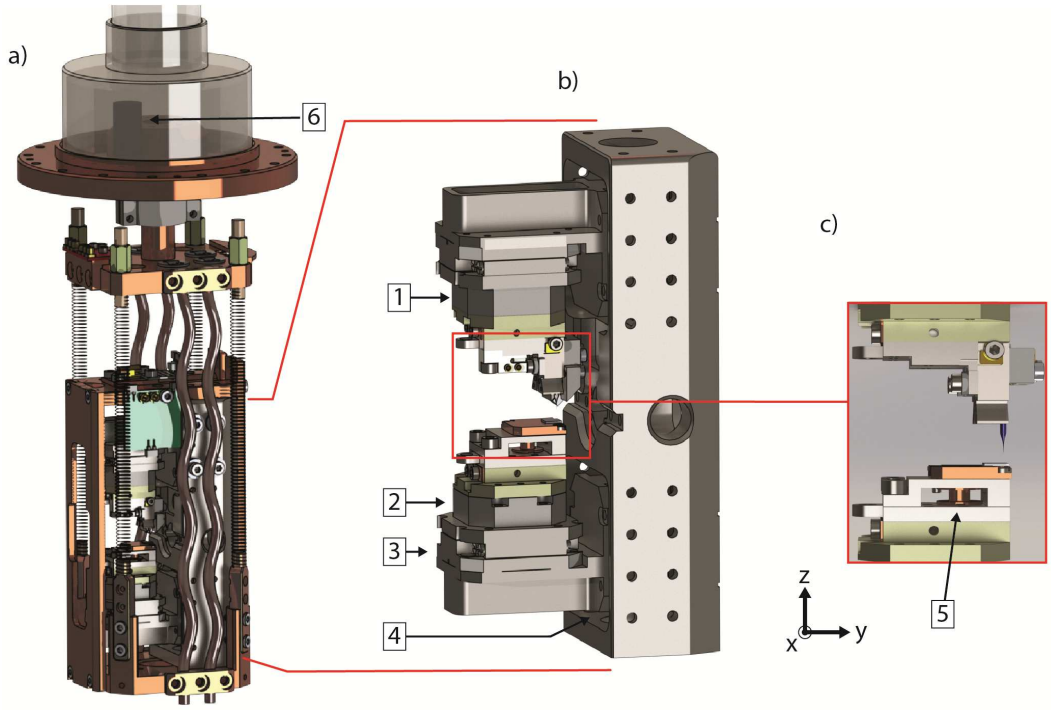

Figure 2.3: The image reports a 3D rendering of the microscope structure, which is the central part of our experimental setup.

a) reports an overview of the microscope settled in the final part of our cryostat probe. A copper frame (brownish colored parts) encases the microscope structure and is hanging through four springs at the final part of the probe. The springs are used for low mechanical frequencies isolation. On the top of the structure, we set the SSAA chip [6]. It was used copper to enhance the thermal coupling through the entire structure.

b) shows the titanium central core, on which is mounted a piezo motor set. It consists in a 2D-scanner [2] with a 37×37 μm^2 scanning range on x and y at 4.2 K, and two piezo positioners [4] (moving on z and y), connected with a L-shape titanium frame to a third positioner (x direction) [3], on which is fixed the 2D-scanner. The z fine movement is performed applying a DC voltage on the z positioner, with a small range extension (≈ 2 μm).

c) shows a zoom-in of the sample holder (bottom stack), and SOT holder (top stack). The bottom stack is mounted on the piezo motor set, which allows the movement of the sample respect to the probe, during the measurements. The top stack is fixed on the top to a titanium stage [1], which can be eventually substituted with a second piezo set for enabling the motion of the SOT probe. Underneath the sample holder is installed a lock heater [5], which can be used to locally heat up the sample.

The last important component in Fig.2.3(a), is the SSAA chip, and a 3D rendering zoom- in is reported in Fig.2.2. The chip is encased in a niobium (Nb) cylinder, that shields from the external magnetic fields and reduce the flux noise during the signal coupling between the SQUID array and the probe-signal carrier circuit, which is called input channel. This can be seen in Fig.2.4. This FLL setup is a commercial one, produced by Magnicon (model XXF-1).

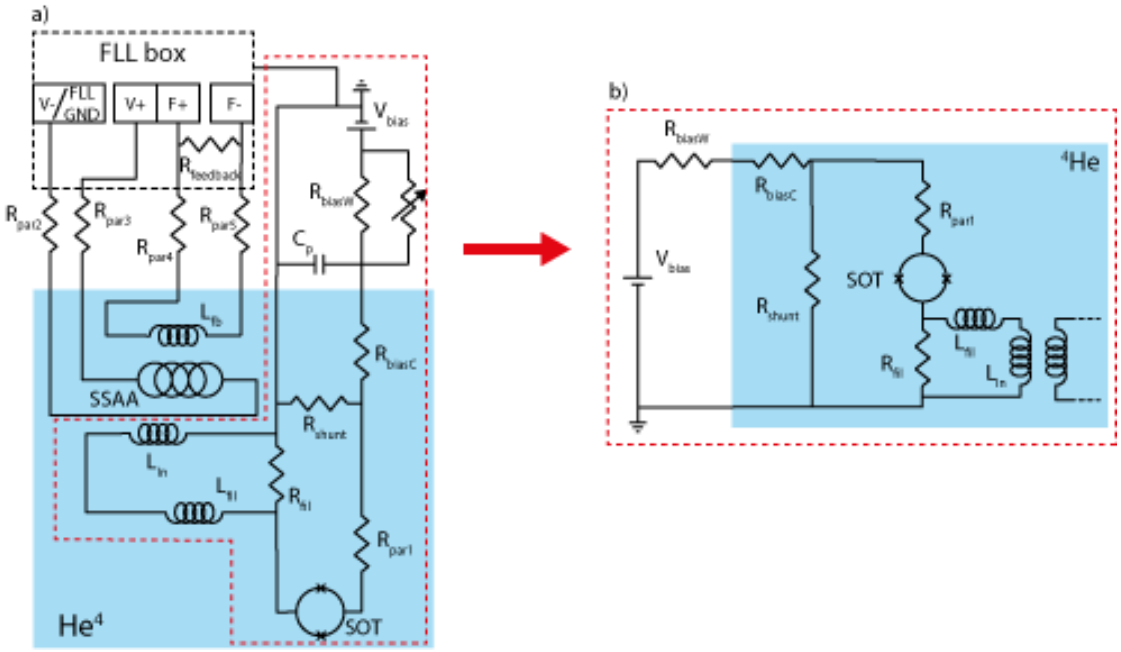

Figure 2.4: Diagram representing the probe circuit. The parasitic resistances are indicated with R_{parN}, with N the number of the line. The other elements are: shunt resistor $R_{shunt} = 3\ \Omega$, bias resistance (in the room temperature side) R_{biasW}, bias resistance (in the liquid ^{4}He side) R_{biasC}, low-pass filter resistance R_{fil}, low-pass filter inductance L_{fil}, input line inductance L_{in}, SQUID array $SSAA$, feedback line inductance L_{fb}, and bias voltage V_{bias}.

The reported circuit diagram highlights the most important parts of the SOT measurement circuit. In Fig.2.4(a), the entire measurement circuit is considered, whereas the red dashed contour refers only to the SOT circuit part, which can be translated in a more simple diagram, shown in Fig.2.4(b). Below, we want to explain point by point the readout procedure for the SOT signal:

- The V_{bias}, generated with the Yokogawa GS200 DC power supply, applies a voltage across the two bias resistors R_{biasW} and R_{biasC}, producing the bias current I_{bias}, which goes through the parallel between the SOT and the shunt resistor R_{shunt}.

- The amount of I_{bias} flowing in the SOT branch of the circuit depends on the SQUID state (superconducting or normal). We will develop this crucial point in the next section, using different models to explain the non-linear contribution given by the SOT.
- The current, which flows through the SOT, carries the magnetic flux information sensed by the probe. An input inductance L_{in} passes this signal to the squid array amplifier in the SSAA chip.
- The SSAA senses the change of flux, produced by the L_{in}, and this produces a change of voltage measured in the FLL box between $V+$ and $V-$ (see the black dashed contour in Fig.2.4(a)).
- As a feedback circuit, the FLL amplifies the voltage change of the SSAA, and through the flux line ($F+$ and $F-$), it sends back a current, which inductively (L_{fb}) compensates the change of flux sensed by the SSAA.
- The current sent back through the flux line, flows across a feedback resistor $R_{feedback}$, which gives us the resulting $V_{feedback}$ signal.
- The $V_{feedback}$ is the raw value that we plot during a measurement, as we will show in the last paragraph of this chapter. This voltage value is proportional to the magnetic field sensed through the SOT scanning probe.

Later, in the next section we will focus on the SOT circuital part (Fig.2.4(b)), omitting the FLL and SSAA parts in the model development.

2.3 SQUID-on-Tip Sensor

As one of the most sensitive magnetometers, superconducting quantum interference devices (SQUIDs) are typically applied for local measurements, miniaturizing their dimensions and implementing them on chips, in the most common planar configuration. In contrast, the device we use for our measurements is fabricated on the apex of a pulled quartz tip [38], allowing us to reach probe dimensions down to ~ 50 nm. The technique, which was developed by Finkler et al. [39], consists in depositing a nano-SQUID on the top of a quartz tip, and for this reason it takes name of SQUID-on-tip (SOT). Contrary to the common configurations, our setup does not require a pickup-coil far from the two Josephson junctions, for trapping the magnetic flux. The junctions are on the tip apex, in proximity of the investigated area, allowing us to perform both thermal and magnetic measurements. Moreover the planar geometry finds a strong downside in the tilt required for the SQUID chip to bring it close enough to the investigated sample. Indeed, due to their fabrication the planar SQUIDs are difficult to approach close to the sample. Even a small tilt would cause one side of the chip to touch though the SQUID is very far from the sample.

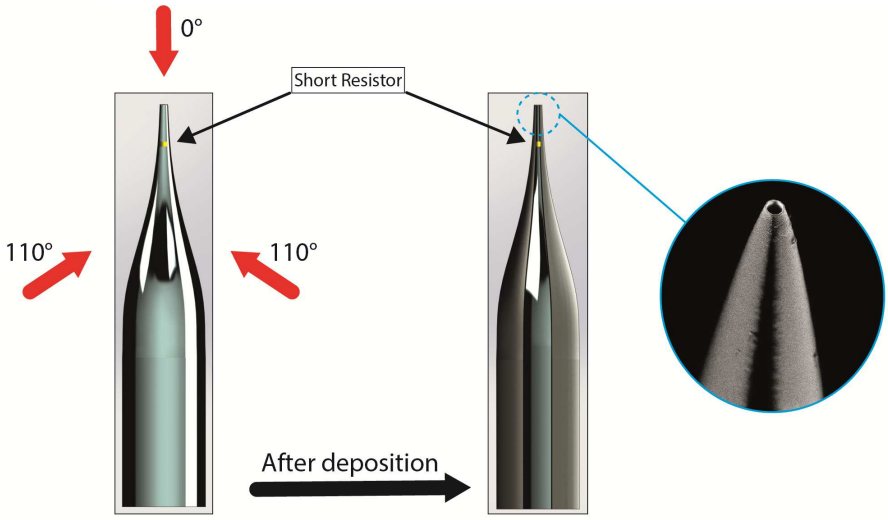

Figure 2.5: The image shows a 3D render of a pulled quartz tip before and after the Pb deposition process. Three different Pb evaporations are done at three different angles taking advantage of the cylindrical tip symmetry. An SEM image shows the apex of a real SOT fabricated in our lab.

2.3.1 SOT Fabrication

The SOT fabrication starts from pulling a hollow quartz tip with 1 mm outer diameter, with a high precision laser puller. The cylindrical geometry is kept until the very end of the tip, and depending on the puller parameters, it is possible to tune the final diameter of the tip down to $40-50$ nm. The tip diameter determines the sensitivity of the final SOT and its spatial resolution. In this sense, the choice of the diameter dimension is strongly dependent on the sample, that we want to investigate.

A three-stage gold (Au) e-beam evaporation, is needed to create two long gold pads on the opposite sides of the tip, creating the top and the bottom contacts with the tip holder (see Appendix at 4.6), using a self-made evaporation mask. The third Au deposition is needed to create a thin strip of gold at $1500-320$ μm from the tip apex, and it forms the short resistance in parallel to the SQUID. This short resistance has a strong influence on the SOT's characteristics, and sensitivity to magnetic field. Its main role is to reduce the hysteresis of the I-V curve during the current sweep up and down.

In the last fabrication step, a superconducting layer is evaporated on the final part of the tip at a base pressure of 2×10^{-8} mbar in a custom-made evaporator (see Appendix F at 4.6). The superconducting material used is lead (Pb). The sample holder is mounted on the very end of a rotateable sample stage (cold-finger), allowing to deposit Pb at different angles, as shown in Fig.2.5. The cold-finger has a hollow interspace, in which liquid-^{4}He flows, cooling down the SOT holder for thermal contact, and reducing the mobility of the hot Pb deposited on the quartz tip. This process allows to deposit Pb homogeneously, avoiding the formation of islands of superconducting material, which could eventually create multiple-junction effects, and affect the SOT characterization. The first two evaporations form two continuous superconducting strips, which connect the previously deposited gold contacts at the apex of the tip. Thanks to the cylindrical symmetry, two gaps are formed at opposite sides. With the third evaporation, the two Pb contacts are closed on the tip apex, forming two weak links (Dayem bridges), working as two Josephson junctions, and then forming a nano-SQUID. The thickness of Pb evaporated, as well the deposition angles, depend by the recipe used and the geometrical condition needed for the final SOT probe.

The SOT is tested in a test-probe setup, which resembles the microscope setup, and allows us to test the probe with the same working condition of temperature and applied magnetic field. Also the readout electronics are the same of the one described for the microscope. The test-probe is built to allow a quick cool-down and warm-up, boosting the characterization process speed. The maximum mag-

netic field possible in the test system is ±2 T. This is enough to characterize a SOT for the entire spectrum of applications achievable by our probe, since at field higher than $1 - 1.2$ T the SOT interference pattern starts to be suppressed, and permanent damage to the probe can occur at higher fields (see Appendix G at 4.7). Once an I-V curve for an SOT is obtained, an analysis of the electric behavior is needed.

2.3.2 Models for SOT Characterization

In this section we report the circuital description of our probe, together with two different approaches used to fit the characterization I-V curve for our SOT.

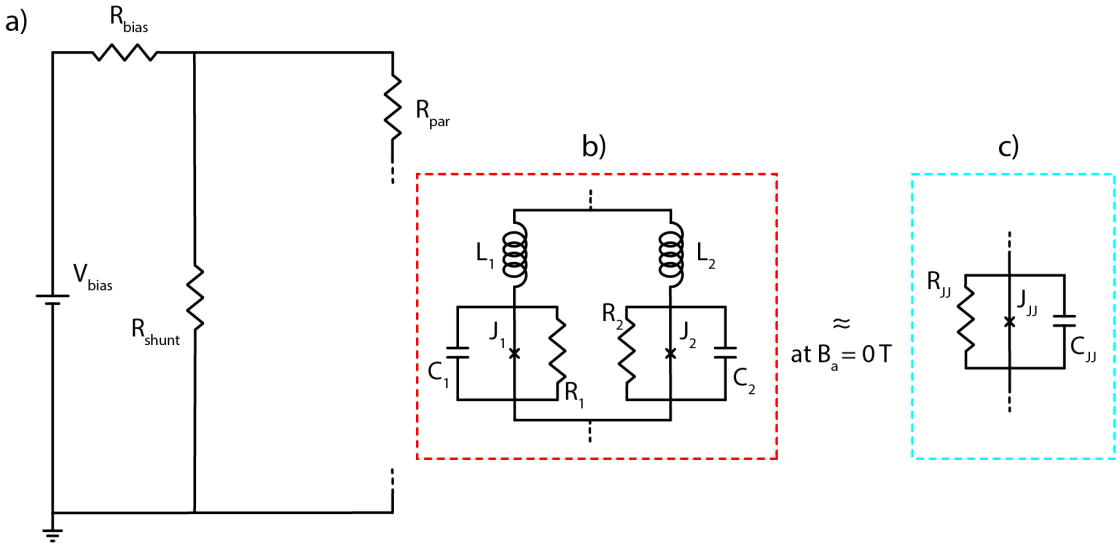

Figure 2.6: Circuit diagram of the SOT in our system. This diagram does not take into account the readout part, which is shown in Fig.2.4. While a) represent the general circuit structure, b) and c) are the two options, which one can consider, for closing the circuit a), depending by the model used. a) and b) represents, respectively, the equivalent RCSJ model for a SQUID, and a single junction. In the scheme we assumed the following definitions: single Josephson junction J_{jj}, single junction resistance R_{jj}, single junction capacitance C_{jj}, parasitic resistance R_{par}, bias resistance R_{bias}, shunt resistance R_{shunt}, SOT resistances R_1, R_2, SOT Josephson junctions J_1, J_2, SOT capacitances C_1, C_2, SOT inductances L_1, L_2, and voltage bias source V_{bias}.

Single Junction Model

Two main factors are interesting for our probe characterization: the first one is the SOT parasitic resistance, which is linked both to the line resistance, and the contact resistance between the SOT-holder clamps and the Au contacts on the quartz tip; the second factor is, the quasiparticle resistance of the SQUID, together with the short resistance in parallel. This last term influences differently the characteristics. Indeed, it depends on whether the SOT goes through the SC-normal state transition or not. An analytic model, can be used to study the SOT I-V characteristics, without considering the field contribution. This model simplifies the SOT as a single junction, and then it is possible to use the resulting equation as a fitting curve to compare the SOT zero-field I-V, deducing the values for the parasitic resistance (R_{par}) and the SOT resistance (R_{sot}). The following analysis was pioneered by Finkler [40]. Using the Kirchoff law it is possible to split the behaviour of the SOT depending on if the current is lower or higher than the critical value:

$$\begin{cases} V_{shunt} = \left(\frac{R_{shunt}R_{par}}{R_{shunt}+R_{par}}\right) I_{bias} & \rightarrow \quad I_{JJ} \leq I_c \\ V_{shunt} = (I_{bias} - I_{JJ})\, R_{shunt} & \rightarrow \quad I_{JJ} > I_c \end{cases} \tag{2.1}$$

where V_{JJ} is the voltage across the SOT plus the parasitic voltage, I_{bias} is the current flowing through the R_{bias} and I_{JJ} is the current though the Josephson junction. Referring to Fig.2.6(a)and(c), we consider:

$$R_{jj} = \frac{R_{short}R_{SOT}}{R_{short} + R_{SOT}} \tag{2.2}$$

with R_{short}, is the small Au strip resistance, evaporated close to the apex of the quartz pulled tip (see Appendix F at 4.6), and R_{SOT} is the quasiparticle resistance of the SOT. From this definition we can rewrite eq2.1:

$$\begin{cases} I_{JJ} = \frac{R_{shunt}}{R_{shunt}+R_{par}} \frac{V_{bias}}{R_{bias}} & \rightarrow \quad I_{JJ} \leq I_c \\ V_{shunt} = I_{JJ}\,(R_{par} + R_{JJ}) - R_{JJ}I_c sin(\delta) & \rightarrow \quad I_{JJ} > I_c \end{cases} \tag{2.3}$$

But, rearranging the second equation in 2.3, we obtain the ohmic component of the SOT current, which produces a voltage drop (eq.1.10), and then:

$$[I_{JJ} - I_c sin(\delta)]R_{JJ} = \frac{\hbar}{e^*}\dot{\delta} \tag{2.4}$$

The first equation in 2.3, gives a linear relation, which describes a complete absence of resistance through the SOT, with an angular coefficient depending on the

parallel between the shunt and the parasitic resistances. The second equation in 2.3 describes a non-monotonic and non-linear behavior. Indeed, we can rewrite it as:

$$I_{JJ}R_{par} + [I_{JJ} - I_c sin(\delta)]R_{JJ} = R_{shunt}\,(I_{bias} - I_{JJ}) \tag{2.5}$$

which can be rewritten as:

$$I_{JJ} = \frac{I_{bias}R_{shunt} + I_c R_{JJ} sin(\delta)}{R_{shunt} + R_{par} + R_{JJ}} \tag{2.6}$$

Then, using eq.2.4 in eq.2.5, one obtains the following differential equation:

$$\frac{\hbar}{e^*}\dot{\delta} + (R_{shunt} + R_{par})\, I_c sin(\delta) - \frac{R_{JJ}R_{shunt}}{R_{shunt}R_{par}R_{JJ}} I_{bias} = 0 \tag{2.7}$$

The form of this equation is: $a\dot{y} + bsin(y) - c = 0$, and it has the analytic solution of the following form:

$$y(t) = 2tan^{-1}\left[\frac{b + \sqrt{c^2 - b^2}tan\left(\frac{\sqrt{c^2-b^2}}{2a}t\right)}{c}\right] \tag{2.8}$$

The mathematical development for this equation is reported in [40], and we briefly report the main steps.

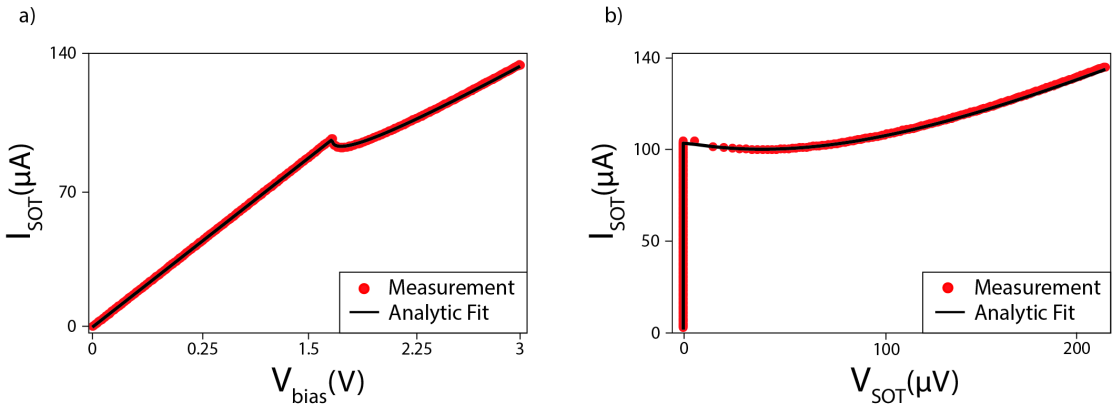

Figure 2.7: Data from the I-V characterization at $B_a = 0$ T of a SOT fabricated in our lab, compared to the single junction analytic model. a) The measured characteristic shows a non-zero voltage in the superconducting state before the transition, due to the parasitic and the quasiparticle resistances. b) Once these contributions are subtracted, the characteristic of the SOT itself is derived.

Summarizing, we find the solution for δ and its time derivative ($\dot{\delta}$) in the form of eq.2.8, then we can use the result in eq.2.7, obtaining a time-dependent solution

for $I_J J(t)$. If we average the solution over one period $[0, 2\pi]$, we can obtain the result for the single junction model, that is used to fit the SOT I-V characteristic curves for our probes. We report an example in Fig.2.7. The solution for $I_J J$ in function of V_{bias} is:

$$I_{JJ}(V_{bias}) = \begin{cases} A - B\sqrt{A^2 - I_c^2} & \rightarrow \quad A > I_c \\ A & \rightarrow \quad A < I_c \end{cases} \tag{2.9}$$

where we have defined:

$$A = \frac{V_{bias} R_{shunt}}{R_{bias}\,(R_{shunt} + R_{par})} \tag{2.10}$$

which results in the current flowing in the ohmic part of the circuit. And:

$$B = \frac{R_{JJ}}{R_{shunt} + R_{par} + R_{JJ}} \tag{2.11}$$

In Fig.2.7 the analytic model matches the data at $B_a = 0$ T with a good accuracy. As explained above, the two fitting parameters are the parasitic resistance and the junction resistance, and for this probe in particular we obtained the following values: $R_{JJ} = 3.1\Omega$, and $R_{par} = 5.6\ \Omega$. Going further in the given analysis, one can observe that eq.2.4 is a simplified version of eq.1.14, given in the first chapter, without considering the capacitance contribution. Considering the washboard potential analogy (see chapter one), the capacitance exclusion of this model assumes the case in which the particle is extremely overdamped, indeed the Stewart-McCumber parameter associated to a JJ tends to 0:

$$\beta_c \equiv \frac{2\pi}{\Phi_0} I_c R_{JJ}^2 C_{JJ} \rightarrow 0 \tag{2.12}$$

Then, the extremely overdamped JJ was considered in this model, and it can be summarized as an equivalent RSJ model (a reduced RCSJ model). The meaning of this approximation is linked to the hysteretic behavior of the SOT. If the inertial term $(\frac{\Phi_0}{2\pi} C_{JJ} \ddot{\delta})$ is neglected, then we assume that once the current is decreased below I_c, the particle is immediately trapped in a minimum of the washboard potential, and it causes no hysteresis in our probe. This is obviously an ideal case. A hysteretic behavior can not be excluded in a real SQUID, even in our shunted SOT. The β_c parameter depends linearly on the capacitance and critical current, and quadraticly on the resistance, but since the junctions of our probe consist of two Dayem bridges, the capacitance is really low. Thus, to lower the hysteresis, we can decrease both I_c or the R_{JJ}. Therefore, it is more effective to reduce the resistance by using a parallel short resistance. In case of a underdamped regime ($\beta_c >> 1$), a negative differential resistance emerges above the I_c, since an

AC contribution for the current produces a non-monotonic behavior, and a sharp transition occurs resolving in a signal jump of the I-V characterization curve [9]. The β_c parameters is not the only one which influences the characteristic of the probe.

SQUID Model

In Fig.2.6(a) and (b), a complete RCSJ model predicts the behavior of the SOT, presenting a more realistic configuration with two Josephson junctions in parallel. We now recall the Kirkhoff equation reported earlier, eq.1.19, and we reduce to a dimensionless form as defined in [9]:

$$\begin{cases} \frac{i}{2} + j = (1-\alpha_I)sin\delta_1 + (1+\alpha_R)\dot{\delta}_1 + \beta_c(1-\alpha_C)\ddot{\delta}_1 + i_{N,1} \\ \frac{i}{2} - j = (1-\alpha_I)sin\delta_2 + (1+\alpha_R)\dot{\delta}_2 + \beta_c(1-\alpha_C)\ddot{\delta}_2 + i_{N,2} \\ \delta_2 - \delta_1 = 2\pi\left(\Phi_a + \frac{1}{2}\beta_L j\right) \end{cases} \tag{2.13}$$

where Φ_a is the applied flux, $i = I/I_{cs}$ is the normalized current, β_L is the screening parameter, and α_I, α_R, α_C are the parameters which define the asymmetries between the two junctions relative to critical current, resistance and capacitance respectively. In this set of equations, the impedance values and current are averaged over the two junctions and than controlled by the $\alpha-$parameters.

$$\begin{cases} R_s = \frac{2R_1R_2}{R_1+R_2} \\ C_s = \frac{C_1+C_1}{2} \\ I_{cs} = \frac{I_{c,1}+I_{c,2}}{2} \end{cases} \tag{2.14}$$

The screening parameters β_L have the following form:

$$\beta_L \equiv \frac{2LI_{cs}}{\Phi_0} \tag{2.15}$$

This parameter is linked to the applied flux, and then it affects the SOT I-V characteristics in function of the interference-like modulation due to the magnetic field. Under the approximation of identical current passing through both branches of SOT, the inductance value can be calculate from β_L. Indeed the main effect of this parameter is the reduction of the amplitude modulation, showing a minimum of the characteristic interference pattern values different from 0. At $\beta_L = 1$ the modulation is reduced by the half, while for $\beta_L >> 1$ the modulation decreases as $1/\beta_L$. The previous considerations are valid when the SOT is in the superconducting state, but once the voltage drop arises across the two junctions,

then the two parameters β_L and β_c govern the SOT behavior. One can summarize these effects, well developed in [9], assuming a perfectly symmetric junctions ($\alpha_I = \alpha_R = \alpha_C = 0$) and noise free current ($i_{N,n} = 0$ with $n = 1, 2$). Moreover we can distinguish two main categories of behavior:

- Analytic solution is possible if we consider the following conditions on the parameters: $\beta_L << 1$, and $\beta_c << 0$. Then, we can reduce eq.2.13 to a simpler form:

$$\begin{cases} \frac{i}{2} \pm j = sin\delta_n + \dot{\delta}_n + \beta_c \ddot{\delta}_n \\ \dot{\delta}_1 = \dot{\delta}_2 \\ n = 1, 2 \end{cases} \tag{2.16}$$

  with few mathematical steps ([9]), one obtains the same form of the RCSJ model for a single junction. Then, in this limit one can achieve the following form for the I-V characteristic for the SOT:

$$V(I, \Phi_a) = \frac{R}{2}\sqrt{I^2 - \left[2I_{cs}\left|cos\left(\pi\frac{\Phi_a}{\Phi_0}\right)\right|\right]^2} \tag{2.17}$$

  The second term under the square root is the SOT current modulation given in eq.1.28. An example is given in Fig.2.8.

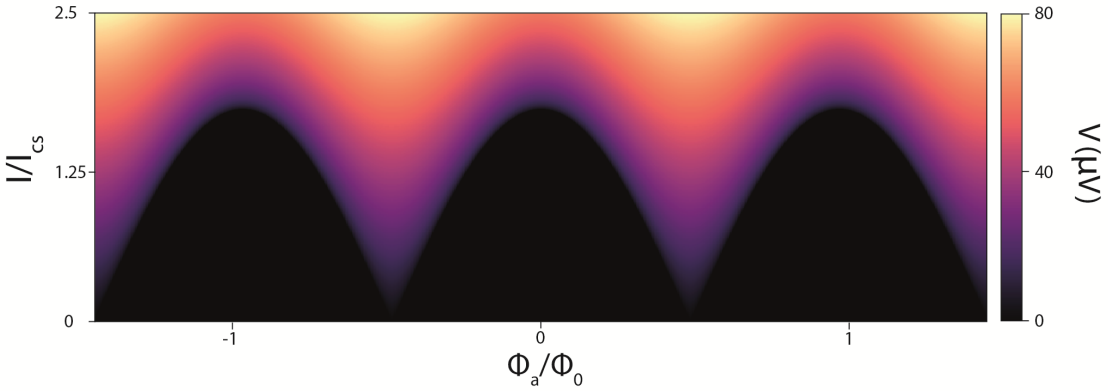

Figure 2.8: Analytic solution of the SOT I-V characteristic assuming $\beta_L << 1$, $\beta_c << 0$, $R_s = 2\Omega$, and $I_{cs} = 120$ μA. The plot represents the current-voltage characteristic as function of the normalized external magnetic flux (Φ_a/Φ_0) applied.

- Numerical solutions are required for any other case of the two main parameters β_L and β_c. Finkler et al.[40] studied the SOT case, and developed a model for the measurement circuital (similar to the one reported in Fig.2.6(a) and (b)), which consists of a set of six differential equations, where the complete circuit is involved in the analysis, included the two inductances (L_1

and L_2) for both the SQUID's branches. We refer to the Finkler's work for a more detailed explanation.

2.3.3 Measurement Procedure

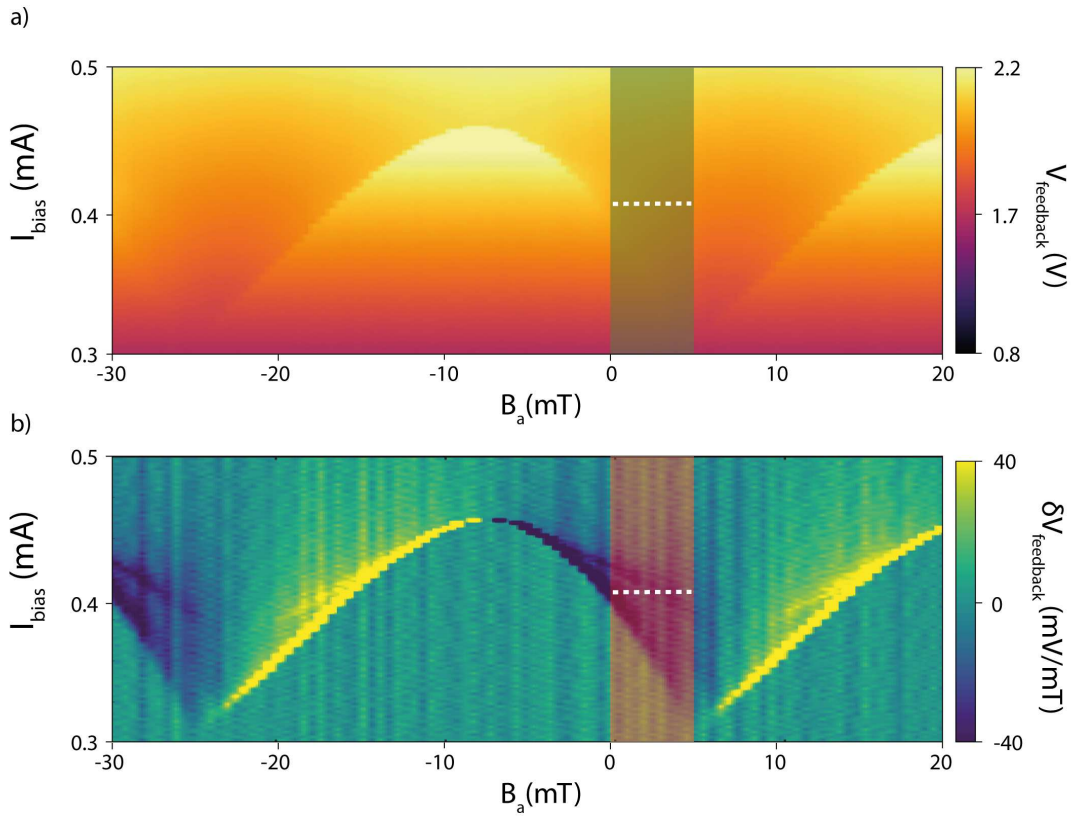

Figure 2.9: SOT characteristic I-V for the SOT used for the MoSi measurements a), and its derivative b). From the period we deduced a SOT diameter of 310 nm. The main feature of this SOT is the strong asymmetry of the field-dependent period. This was necessary to perform low field measurements and detecting at 0−field. The asymmetry was obtained using a modified *Pb* deposition recipe.

Here, how we characterize the SOTs used for the two experiments presented in this thesis. Due to different needs, the fabrication recipes used were modified to match the experimental working condition for the samples. For the MoSi investigation presented section 3.3, we needed sensitivity at zero applied magnetic field, because of the low field at which we were able to study the vortex density and dynamics

in the sample. To achieve that type of probe, we intentionally introduced a geometrical asymmetry between the two Josephson junctions, resulting a in a shift of the interference-like pattern of the SOT I-V characteristic in function of the magnetic field, as it is shown in Fig.2.9. The hysteresis of this probe is small enough to be negligible, and it is a indication of a small Stewart-McCumber parameter ($\beta_c << 1$). Moreover, considering the observation made in the previous paragraph, the calculated screening parameter is $\beta_L \approx 1$, resulting in a SOT inductance of $L_s \approx 2.3$ pH.

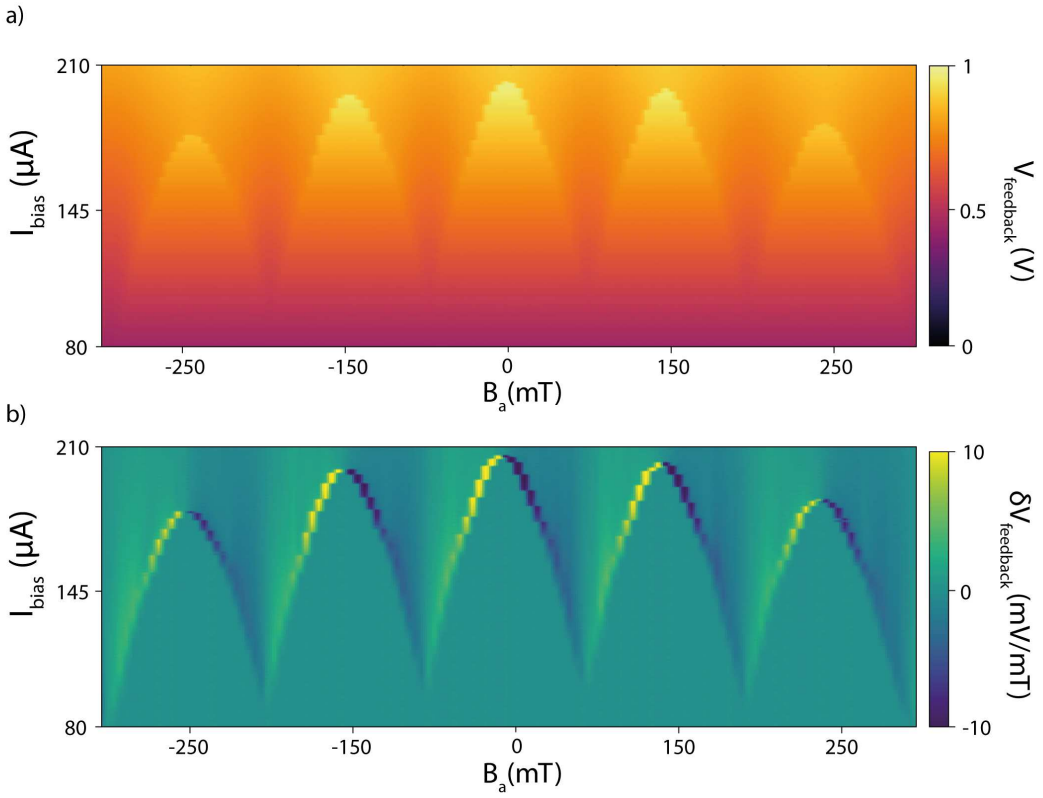

Figure 2.10: The image reports the I-V characterization in function of B_a a), and its derivative b), for the SOT used for the CoFeB nanotube investigation, with a 150 nm diameter. Is possible to observe that the squid has a symmetric period, and then a lower sensitivity around 0 T as well as in the area close to $\frac{\Phi_a}{\Phi_0} = N\frac{1}{2}$, with $N = [0, 1, 2...]$.

For the CoFeB nanotube experiment presented in section 3.2, we needed a probe able to reach higher magnetic fields without occurring in the field suppression (see Appendix G at 4.7). Reducing the SOT diameter in the pulling phase of the fabrication, we obtained a more stable SQUID for higher magnetic field values, and in parallel we also improved the spatial resolution, which results in a larger

period of the interference-like pattern, as can be seen in Fig.2.10. The downside of this probe was the lower sensitivity compared to the one used for the MoSi sample, and the calculation parameters result in $\beta_c << 1$, and $\beta_L \approx 0.38$.

Once the working temperature and pressure are reached, a further characterization is needed. For the following part we consider the I-V characterization in Fig.2.9. The first derivative gives us the information about the most sensitive working areas for our probe.

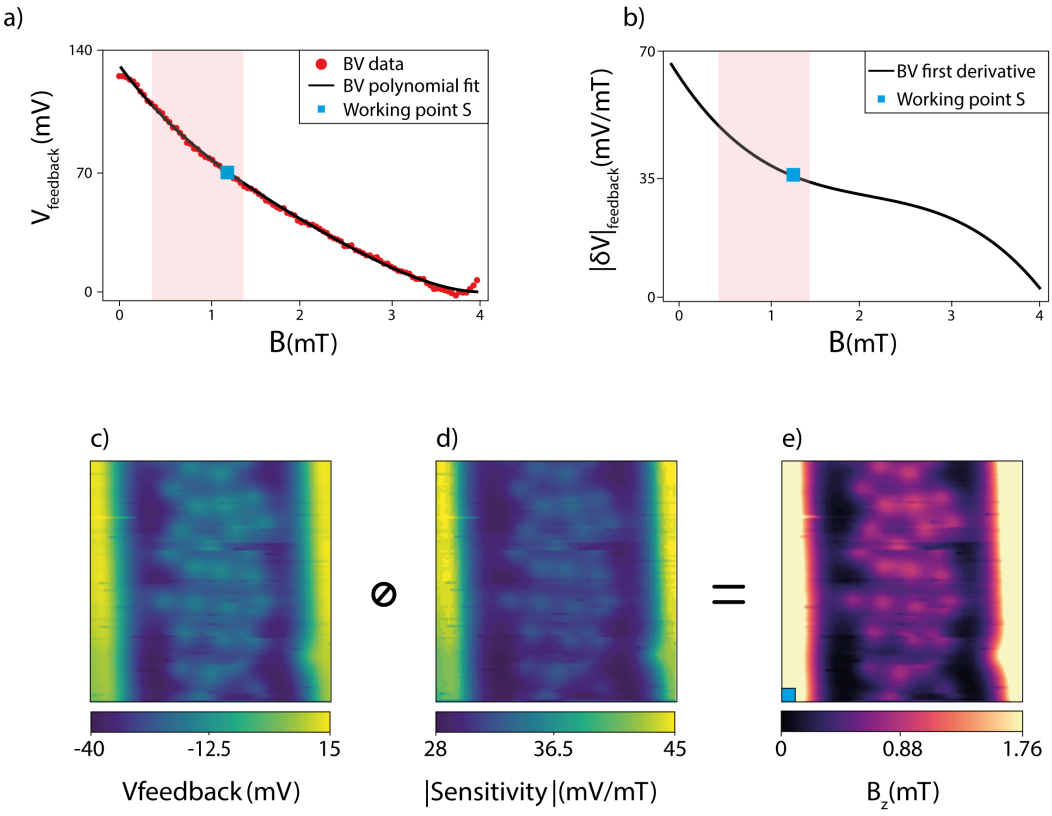

Figure 2.11: The B-V characterization is fitted with a polynomial curve a), and the absolute value of its first derivative shows the magnetic sensitivity of the probe for the chosen B_a range and fixed bias voltage applied to the SOT b). The initial working point for our SOT is highlighted with the blue square, and it corresponds to the initial point for the scan map e). The two light-red areas in a) and b), show the change of the magnetic signal and sensitivity during a magnetic map scan over the sample. The SOT scans over the sample and it measures a map of $V_{feedback}$ values c), then we create a sensitivity map d). The Hadamard division of these two matrices results in the magnetic map e).

A lower sensitivity requires a higher integration time for the measured signal (both DC and AC), on each point of the magnetic map, dilating the measurement time. In order to explain the measurement process, we summarize all the steps involved in one measurement of a DC magnetic map, using Fig.2.9 ans Fig.2.11 as reference.

- From the SOT characterization in Fig.2.9, we select the highlighted area as a good sensitivity spot for our probe. The white dashed line corresponds to the I_{bias} that we send through the SOT. Once the I_{bias} is fixed, we need to characterize with more precision the behavior of the SOT as function of B_a. In this particular case, we have chosen $B_a = [0 - 4]$ mT range.

- In Fig.2.11(a), the B-V characteristic consists in the output signal ($V_{feedback}$) as function of B_a. $V_{feedback}$ is the output of the flux locked loop (FLL) circuit, which amplifies the signal sensed by our SOT, as explained in the first section of this chapter.

- Fig.2.11(b) shows the absolute value of the B-V first derivative with respect to the magnetic field. This is the sensitivity in mV/mT, and we can deduce few observations. In case we can approximate the B-V to a linear behavior, we have little changes of the sensitivity values. This can happen in two ways: first, if the B-V itself is highly linear for the magnetic field range chosen; second, if we investigate a sample region where the change of the magnetic field, sensed by the SOT, is so small that we can approximate the B-V as a linear function. In these two cases, we can assume the value of sensitivity for our probe as a constant, but for all the other cases we need to develop a different approach, which keeps into account a relevant sensitivity change allover the map.

- Following the last consideration of the previous point, we need to avoid any loss of information during the measurement. Once we obtain a $V_{feedback}$ map/matrix from our scanning SOT, we can link these values to the corresponding change of magnetic field in the B-V function, and then, we can deduce the corresponding sensitivity value for each $V_{feedback}$ matrix element, thus building the sensitivity matrix.

- The Hadamard division between the $V_{feedback}$ matrix and the sensitivity matrix gives the DC magnetic map, as shown in Fig.2.11c), d), and e). We subtracted the minimum value of the resulting matrix to set the starting value of the colorbar on 0. The calculation of each element for the final matrix can be summarized as follow:

$$B_z(i,j) = \frac{V_{feedback}(i,j)}{|S(i,j)|} - min[B_z] \quad \forall \quad \begin{cases} i = [1,..,N] \\ j = [1,..,M] \end{cases} \tag{2.18}$$

where i and j are the matrix indexes, and $N \times M$ is the matrix/map dimension.

The process just explained uses as example a magnetic DC measurement, but this method is used as well for the magnetic lock-in measurements for the AC signals. We can conclude with few considerations about the choice of the right working point (i.e. $[I_{bias}, B_a]$), which is not trivial. Indeed one can assume that the highest sensitivity point on the curve is the best working point. Actually few elements have to be kept in consideration:

- Sample interaction with B_a. If the sample produces a strong stray field, or it distorts the magnetic flux lines, then the probe can detect a large change of signal, which can shift the working point in a region of low sensitivity, or in a region not included in the B-V characterization curve. In order to avoid this problem one can use previous measurements or simulations, improving the quality of the working point choice in order to keep the change of the magnetic signal inside the B-V desired region. Usually in our experiment we provide many different B-V curve for different $[I_{bias}, B_a]$ ranges.
- In case the initial working point chosen for a map is to close to the end of a B-V function, we can obtain a sensitivity map which present a saturated area. This represents a loss of information, since we do not know the behavior if the B-V for the corresponding field variations.
- Zero-sensitivity regions. The most direct problem emerges if the working point considered is too close to a zero-sensitivity region, where the SOT is in the superconducting state for the given values of $[I_{bias}, B_a]$, and then it does not show any dependency by the trapped flux.

In conclusion, one can consider the example reported in Fig.2.11. The sensitivity map (2.11(b)) shows a clear minimum surface, so called sensitivity floor. In this case, magnetic field sensitivity is at least 28 mV/mT and up to 45 mV/mT depending on the position.

Results

3.1 Introduction to Results

The first chapter presented the main theoretical tools used for the investigation of the MoSi sample, and the probe, that we have used for SPM measurements, while the second chapter provided a description of the experimental setup and a deeper analysis of the SOT probe as highly sensitive magnetometer. This third chapter presents two main works developed in the last two years.

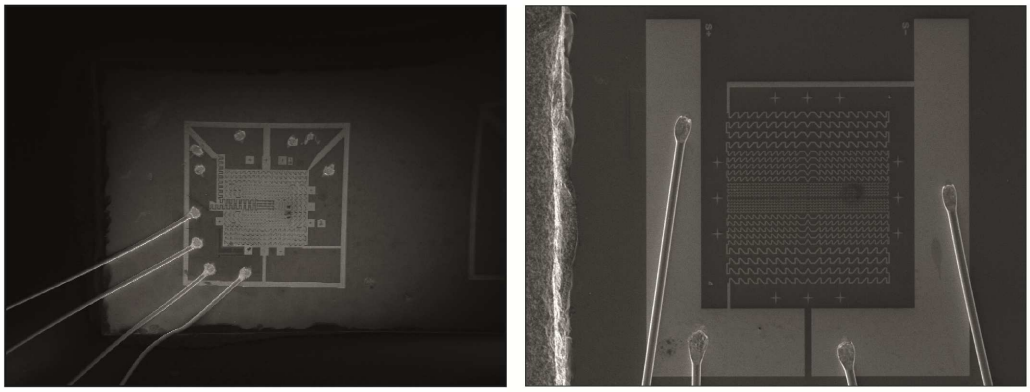

Figure 3.1: Scanning electron micrograph overviews of the two sample investigated in this chapter. MoSi sample on the left, and CoFeB nanotubes on the right.

For this reason, this chapter is split in a first section, where we present results on detection of the stray field, produced by CoFeB nanotubes under the effect of an external magnetic field, and a second section where we discuss the investigation of superconducting MoSi thin films and the behavior of vortices therein.

3.2 CoFeB Nanotubes

As mentioned before, magnetic measurements on these nanostructures were done for two reasons. First, we wanted to test the potential of our magnetic SPM technique on a sample and second, we wanted to confirm the existence of exotic magnetization states in CoFeB nanotubes previously shown by XPEEM measurements [41,42]. The constant need for magnetic storage-technology miniaturization, provides a strong motivation for the optimization of nanomagnetic structures. Indeed, the nano-magnets' large surface-to-volume ratio makes them susceptible to roughness, exterior defects, and imperfections. This problem results in a poor control of the magnetic domains, which can lead to a complicated and not reproducible switching processes [43]. One approach to address these challenges is to use nanomagnets that support remnant flux-closure configurations.

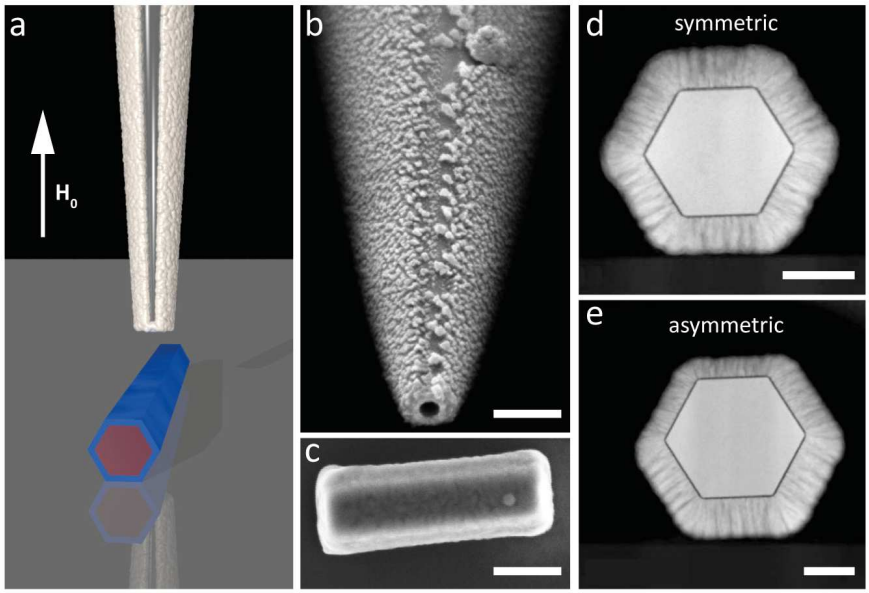

Figure 3.2: Experimental setup. (a) Schematic drawing showing the scanning SOT, a FNT lying on the substrate, and the direction of H_0. The CoFeB shell is depicted in blue and the GaAs core in red. Pb on the SOT is shown in white. SEMs of the (b) the SOT tip and (c) a 0.7 μm long FNT. (d,e) Cross-sectional HAADF STEMs of two FNTs from a similar growth batch as those measured. The scalebars represent 200 nm in (b,c) and 50 nm in (d,e).

The resulting absence of magnetic charge at the surface reduces its role in determining the magnetic state and can yield stable remnant configurations with

both fast and reproducible reversal processes. In addition, the lack of stray field produced by flux-closure configurations suppresses interactions between nearby nanomagnets [44]. To achieve this goal, core-free shapes have been considered, like rings [45, 46] and tubes [47]. These shapes are meant to host a vortex-like fluxclosure configurations with magnetization pointing along their circumference. Indeed, the lack of a magnetic core removes the dominant contribution to the exchange energy, which otherwise compromises the stability of vortex states.

In this section, we present a first measurement of the stray field, using our SOT probe, produced by ferromagnetic nanotubes (FNTs) under the effect of an external magnetic field. These images show the extent to which flux closure is achieved in FNTs of different lengths as they are driven through magnetic reversal. Together with the magnetic images taken, micromagnetic simulations of the stray field have been used as comparison. While there have been many theoretical studies on the configurations supported in FNTs [47–55], experimental images of these states have been so far limited in both scope and detail. The great advantage in using the SOT technique, is the ability to collect high resolution spatial information about the stray field, which is not possible with techniques like cantilever magnetometry [56, 57], SQUID magnetometry [58, 59], or magnetotransport measurements [60, 61], and thanks to this advantage, ultimately, it was possible to confirm that these nanostructures can be induced in a flux-closed configuration..

3.2.1 Sample Fabrication

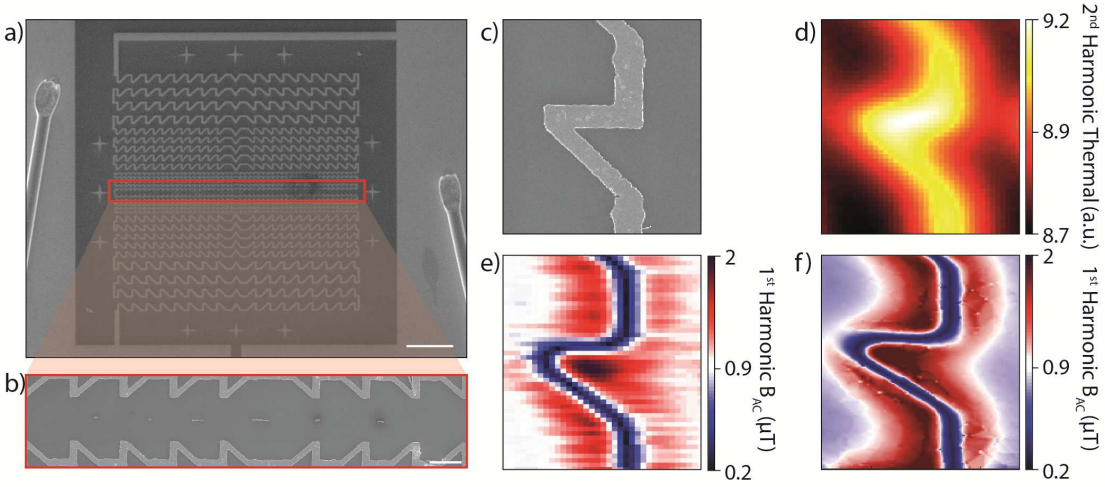

Figure 3.3: a) A sample overview taken by SEM (scalebar 150 μm). The serpentine-like pattern was used as marker for navigation over the sample, with our probe. An AC bias current I_{AC} was applied. Lock-in measurements were performed in order to detect both the Biot-Savart magnetic signal e), and the second harmonic thermal signal, which maps the local temperature gradients, as shown by Halbertal et al. [62] d). Finite element simulations of the serpentine were used to set a sample-probe working distance f). c) a serpentine branch, used as reference for the magnetic, thermal, and simulation maps (d-f)). In the middle of the marker serpentine, we placed the CoFeB FNTs. b) a zoom-in of the SEM image, shows the length and the position of each nanotube investigated (scalebar 10 μm).

The FNT samples are made of a nonmagnetic GaAs core surrounded by a 30 nm-thick magnetic shell of CoFeB. Fig.3.2, shows examples of the sample's hexagonal cross-section, for some of the FNTs characterized. The cores of nanotubes are grown by molecular beam epitaxy on SI (111) substrate, with Ga droplets as catalist [63]. The CoFeB layer has been magneton-sputtered onto GaAs nanowires (NWs), producing an amorphous shell [57], trying to avoid magnetocrystalline anisotropy [63–65]. Nevertheless, Baumgaertl et al. [61] have shown that a small growth-induced magnetic anisotropy is unavoidable. During CoFeB sputter deposition, the wafers of upright and well-separated GaAs NWs are mounted with a 30° angle between the long axis of the NWs and the deposition direction. The wafers are then continuously rotated in order to achieve a conformal coating. In order to obtain NTs with different lengths and well-defined ends, we cut individual NTs into segments using a Ga FIB in a scanning electron microscope. From.Fig.3.2 is

possible to observe the defect-free surfaces of a FNT (images taken with scanning electron micrographs, SEM), with a roughness less than 2 nm, and showing cross-sectional high-angle annular dark-field (HAADF) scanning transmission electron micrographs (STEM) of two FNTs from the same growth batch as those measured, highlighting the possibility for asymmetry due to the deposition process. Previous dynamic cantilever magnetometry measurements, show for these FNTs a saturation magnetization $\mu_0 M_s = 1.3 \pm 0.1$ T. The aspect ratio for these FNTs has been measured as the ratio between the diameter, which spans between 200 and 300 nm, and the length, ranging over 0.4 and 7 μm. In particular, different lengths were planned, and tuned cutting the FNTs in segments with focused ion beam (FIB).

The SOT, used for this experiment, has an effective diameter of 150 nm, as extracted from measurements of the critical current I_{SOT} as a function of a uniform magnetic field $H_0 = H_0\hat{z}$ applied perpendicular to the SQUID loop. At the operating temperature of 4.2 K, pronounced oscillations of critical current are visible as a function of H_0 up to 1 T. Maps of the magnetic stray field produced by individual FNTs are made by scanning the FNTs lying on the substrate in the xy-plane 300 nm below the SOT sensor. The measured flux then represents the integral of the z-component of the total magnetic field over the area of the SQUID loop. By subtracting the contribution of H_0, we isolate the z-component of stray field, H_{dz} integrated over the area of the SOT at each spatial position.

3.2.2 Dipole-Like States

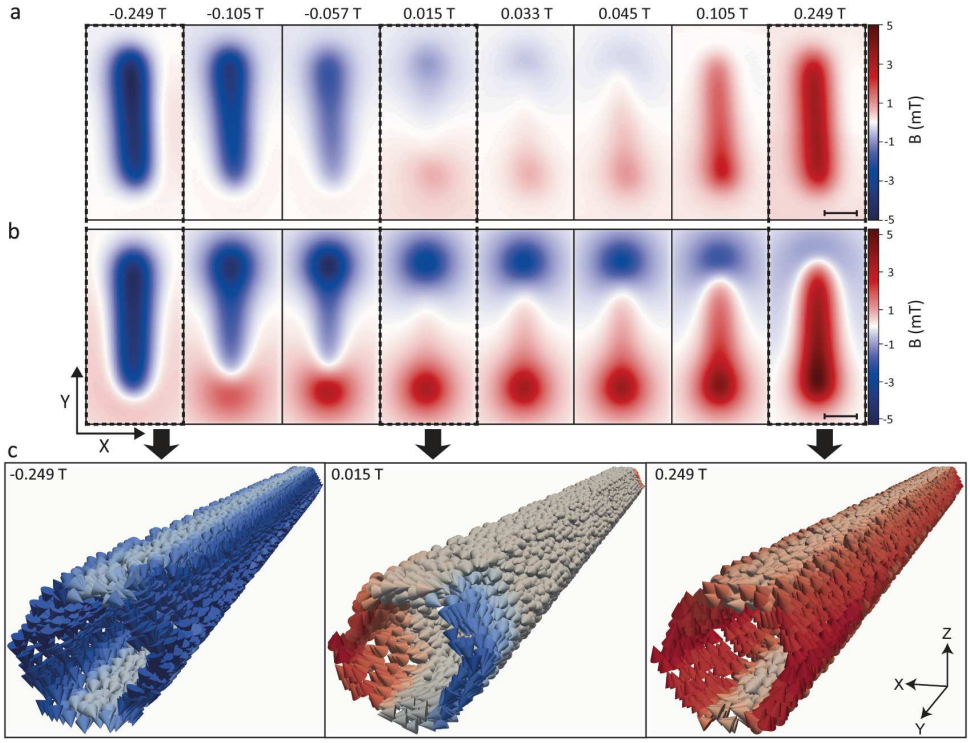

Figure 3.4: Magnetic reversal of a 4 μm long FNT ($l = 4.08$ μm, $d = 260$ nm) in a field H_0 applied perpendicular to its long axis. Images of the stray field component along $\hat{z}$, H_{dz}, in the xy-plane 300 nm above the FNT for the labeled values of $\mu_0 H_0$ (a) as measured by the scanning SOT and (b) as generated by numerical simulations of the equilibrium magnetization configuration. The dashed line delineates the position of the FNT. The scalebar corresponds to 1 μm. (c) Simulated configurations corresponding to three values of H_0. The middle configuration, nearest to zero field, shows a mixed state with vortex end domains of opposing circulation sense. Arrows indicate the direction of the magnetization, while red (blue) contrast corresponds to the magnetization component along $\hat{z}(-\hat{z})$.

The stray field behavior of FNTs shows a strong dependence on the length of each nanotube. Above a certain length, FNTs show a dipole behavior during the magnetization process at the sweeping of the external field. Referring to Fig.3.4, one can observe the stray field maps of a 4 μm long FNT for a series of fields $\mu_0 H_0$ increased from -0.6 to 0.6 T. The maps reveal a reversal process consistent with a rotation of the net FNT magnetization. At $\mu_0 H_0 = -249$ mT and at

more negative fields, H_{dz} is nearly uniform above the FNT, indicating that its magnetization is initially aligned along the applied field and thus parallel to $-\hat{z}$. As the field is increased toward positive values, maps of H_{dz} show an average magnetization $\langle M \rangle$, which rotates toward the long axis of the FNT. Near $H_0 = 0$, the two opposing stray field lobes at the ends of the FNT are consistent with an $\langle M \rangle$ aligned along the long axis. With increasing positive H_0, the reversal proceeds until the magnetization aligns along $\hat{z}$.

In Fig.3.4, the magnetic maps are plotted next to micromagnetic simulations, performed with the software package Mumax3 [66], which employs the Landau-Lifshitz micromagnetic formalism with finite-difference discretization. The simulations match closely the measurements, moreover the sample magnetization is given for three different external fields, -0.249, -0.015, and 0.249 T respectively (see Appendix A at 4.1). These configurations present a non uniform configuration. In the central part of the FNT, the magnetization of the different facets in the hexagonal FNT rotates separately as a function of H_0, due to their shape anisotropy and their different orientations. As H_0 approaches zero, vortices nucleate at the FNT ends, resulting in a low-field mixed state, that is, a configuration in which magnetization in the central part of the FNT aligns along its long axis and curls into azimuthally aligned vortex domains at the ends. A similar behavior was obtained with a 2 μm long FNT with a similar cross-section. The progression of the stray field in function of H_0 follows closely the one of the 4 μm FNT.

3.2.3 S-Shape States

In this section, measurements of the stray field produced by the 0.7 μm long FNT are reported. As it can be seen in Fig.3.5, this sample exhibits a different stray field progression. Starting from a negative field, the FNT shows a persistent negative single-lobed signal. $\langle M \rangle$ does not show any sign of rotation along the easy axis (y-direction), until $\mu_0 H_0 = -15$ mT. Close to zero field, the stray field map is characterized by a s-shape pattern. Indeed one can observe that a s-like zero-field line appears. Further increase of $\mu_0 H_0$ again produces a single-lobed stray field signal, but with positive sign.

In order to infer the magnetic configuration of the FNT, we simulate its equilibrium configuration as a function of H_0 using the sample's measured parameters: $l = 0.7$ μm, $d = 250$ nm, and $t = 30$ nm. For a perfectly hexagonal FNT with flat ends, the simulated reversal proceeds through different, slightly distorted global vortex states, which depend on the initial conditions of the magnetization. Such simulations do not reproduce the s-like zero-field line observed in the measured stray-field maps. However, when we consider defects and structural asymmetries

likely to be present in the measured FNT, the simulated and measured images come into agreement. In these refined simulations, we first consider the magnetic dead-layer induced by the FIB cutting of the FNT ends as previously reported [67–69]. We therefore reduce the length of the simulated FNT by 100 nm on either side. Second, we take into account that the FIB-cut ends of the FNT are not perfectly perpendicular to its long axis (see Appendix B at 4.2).

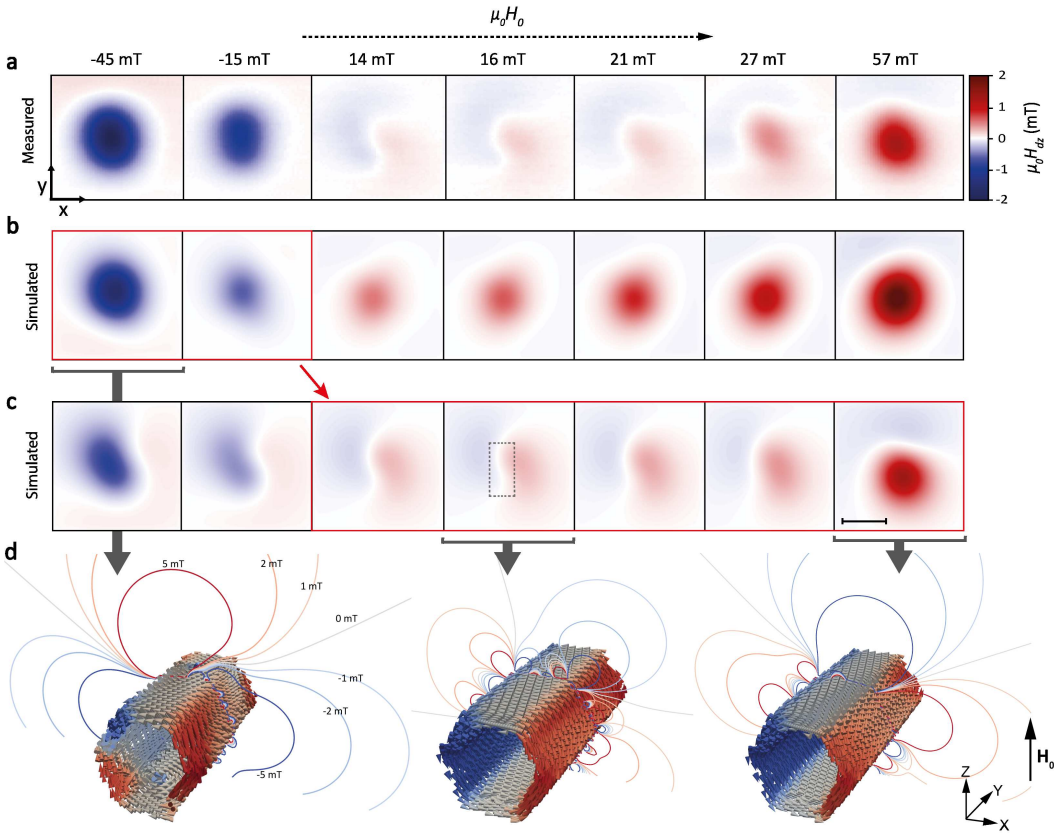

Figure 3.5: Magnetic reversal of a 0.7 μm long FNT (l = 0.69 μm, d = 250 nm) in a field applied perpendicular to its long axis. Images of the stray field component along $\hat{z}$, H_{dz}, in the xy-plane 300 nm above the FNT for the labeled values of H_0 (a) as measured by the scanning SOT. (b,c) Numerical simulations of H_{dz} produced by two progressions of equilibrium magnetization configurations with different initial conditions. The dashed line delineates the position of the FNT and the scalebar corresponds to 0.5 μm. (d) Magnetization configurations and contours of constant H_{dz} corresponding to three values of H_0. The configuration on the left is characterized by two vortices in the top and bottom facets, respectively. The middle and right configurations are distorted global vortex states. Arrows indicate the direction of the magnetization, while red (blue) contrast corresponds to the magnetization component along $\hat{z}(-\hat{z})$.

SEMs of the investigated FNT show that the FIB cutting process results in ends slanted by 10° with respect to $\hat{z}$. Finally, we consider that the 30 nm thick hexagonal magnetic shell may be asymmetric, that is, slightly thicker on one side of the FNT due to an inhomogeneous deposition, for example, Fig.3.2(e). After these modifications, the simulations presented four different possible stray field progression depending on initial conditions. Two of them shown a stray field signal matching the measurements. The measured stray-field images are consistent with the series shown in Fig.3.2(b) for negative fields ($\mu_0 H_0 = -45, -15$ mT). As the applied field crosses zero (-15 mT$\leq \mu_0 H_0 \leq 14$ mT), the FNT appears to change stray-field progressions. The images taken at positive fields (14 mT$\leq \mu_0 H_0$) show patterns consistent with the series shown in Fig.3.2(c). The magnetic configurations corresponding to these simulated stray field maps suggest that the FNT occupies a slightly distorted global vortex state. Before entering this state, for example, at $\mu_0 H_0 = -45$ mT, the simulations show a more complex configuration with magnetic vortices in the top and bottom facets, rather than at the FNT ends. On the other hand, at similar reverse fields, for example, $\mu_0 H_0 = 57$ mT, the FNT is shown to occupy a distortion of the global vortex state with an tilt of the magnetization toward the FNT long axis in some of the hexagonal facets.

3.2.4 Anomalous States

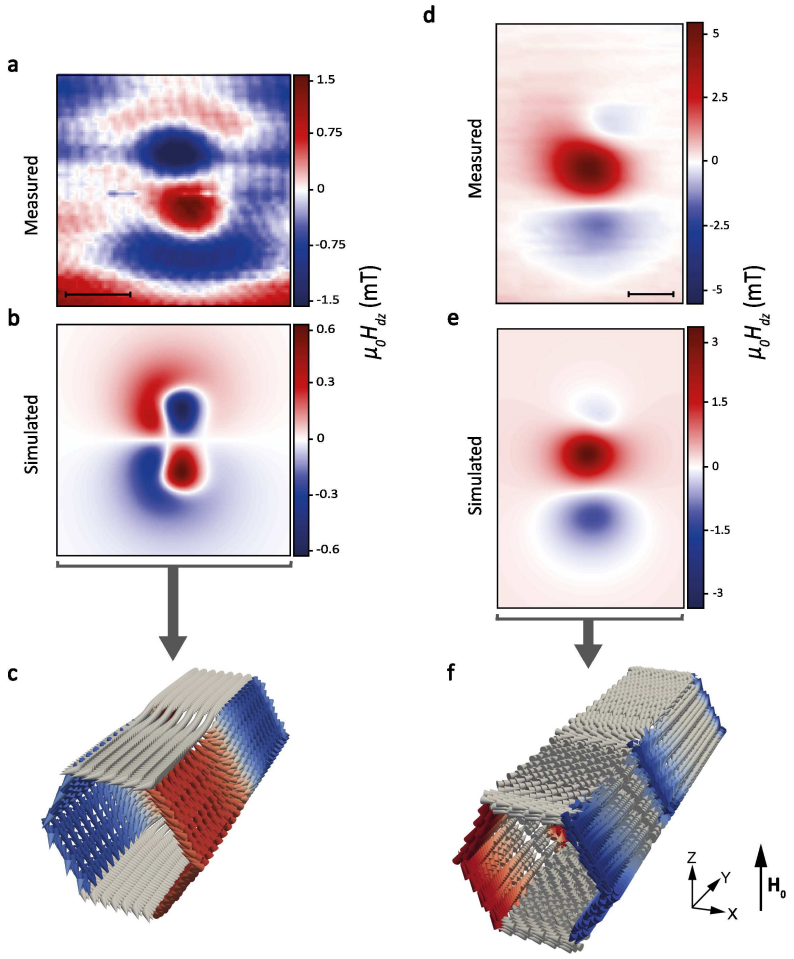

Figure 3.6: Anomalous stray-field patterns found at low applied field. (a) Stray-field pattern of the 0.7 μm long FNT ($l = 0.69$ μm, $d = 250$ nm) at $\mu_0 H_0 = 20$ mT. (b) Similar map produced by an opposing vortex state, shown schematically in (c) and observed near zero field by Wyss et al.[41] (d) Stray-field pattern of the $1\mu m$ long FNT ($l = 1.05\mu m$, $d = 250nm$) at $\mu_0 H_0 = 21$ mT. (e) Similar field map produced by a (f) multidomain mixed state with vortex end domains and opposing axial domains separated by a vortex wall. The scalebar corresponds to 0.5 μm. In (c,f), arrows indicate the direction of the magnetization, while red (blue) contrast corresponds to the magnetization component along $\hat{z}$.

As a last result, it is interesting to know the existence of anomalous states for some minor loop measurement of FNTs, with $l \leq 1\mu m$. Micromagnetic simulations were

not able to reproduce such stray field patterns. In Fig.3.6 two cases are reported, for a 0.7 μm and 1 μm FNTs length. For the first one, the magnetic map was taken at $\mu_0 H_0 = 20$ mT, while for the second one $\mu_0 H_0 = 21$ mT. These maps are significantly different from the previous cases, and no equilibrium magnetization configuration was found in order to generate these stray field patterns.

We tested a few idealized configurations in search of possible matches. In particular, the measured pattern shown in Fig.3.6(a) is similar to the pattern produced by an opposing vortex state. This configuration, shown in Fig.3.6(c), consists of two vortices of opposing circulation sense, separated by a domain wall. It was observed with XMCD-PEEM to occur in similar-sized FNTs in remnance at room temperature. The pattern measured in Fig.3.6(4e) appears to match the stray-field produced by a multidomain state consisting of two head-to-head axial domains separated by a vortex domain wall and capped by two vortex ends, shown in Fig.3.6(f).

Although these configurations are not calculated to be equilibrium states for these FNTs in a perpendicular field, they have been suggested as possible intermediate states during reversal of axial magnetization in a longitudinal field. The presence of these anomalous configurations in our experiments may be due to incomplete magnetization saturation or imperfections not taken into account by our numerical model.

Final Observations

At the end, using the scanning SQUID's ability to make images as a function of applied magnetic field, we reveal the progression of stray-field patterns produced by the FNTs as they reverse their magnetization. Future scanning SOT experiments in parallel applied fields could further test the applicability of established theory to real FNTs. While the incomplete flux closure and the presence of magnetization configurations not predicted by simulation indicate that FNT samples still cannot be considered ideal, scanning SOT images show the promise of using geometry to program both the overall equilibrium magnetization configurations and the reversal process in nanomagnets. Further observations and considerations are reported in the conclusions in last chapter of this thesis.

3.3 MoSi Superconducting Thin Film

Nowadays, type II superconductors are involved in many applications, which span from research for industry, to technological experimental setup implementations. Main examples are the superconducting magnets which can reach high magnetic fields (T) thanks to the zero dissipation current, flowing through the coils. Further examples, from the research point of view, are given by superconductors used in single photon detectors or for superconducting qubit setups. In any of these applications and more, the use of type II superconductors became relevant due to their high H_{c2}, compared to the H_c of type I. This higher tolerance of external magnetic field is linked to the mixed state introduced in the first chapter. The motion of vortices causes emerging dissipation which can result in measurement noise or, under certain conditions, in an avalanche state which can cause easier the superconducting state to collapse [70]. The motion of vortices inside the SC, is tightly related to the average force of the pinning centers in the material itself.

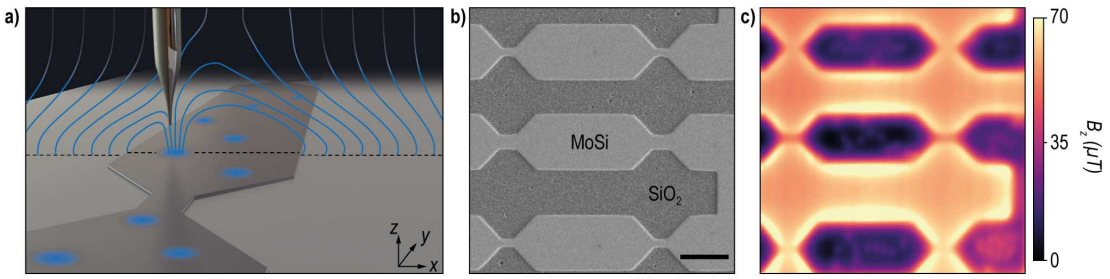

Figure 3.7: Setup and MoSi sample. (a) Schematic diagram of scanning SOT tip above superconducting MoSi wire with vortices. (b) Scanning electron micrograph (SEM) and (c) scanning SQUID image of the investigated region. Color-scale contrast in (c) corresponds to the out-of-plane magnetic field $B_z(x, y)$ measured by the SOT in an out-of-plane applied field of $B_a = 1.5$ mT. Dark areas of low Bz are due to the Meissner screening of the MoSi film, while bright dots indicate the penetration of flux in the form of superconducting vortices. Scale bar: 10 μm.

The dissipative motion of vortices, driven by flowing electrical current, destroys the material's ability to carry current with zero resistance. By controlling the pinning of vortices, they can be immobilized, thereby restoring the superconducting state. Optimized pinning [71–79], and other methods of arresting vortex motion [80] have been used to extend the coherent dissipation-free superconducting state to high critical current densities, fields, and temperatures. The microwave response of superconductors is also affected by the high-frequency dynamics of vortices [81].

Vortex trapping contributes to loss in microwave resonators and conditions the performance of the circuits used as qubits in superconducting quantum computers [82]. Evidence has also emerged that superconducting vortices play a significant role in superconducting nanowire single photon detectors (SNSPDs) [83], whose high speed, detection efficiency, and low dark count rates make them attractive for a wide variety of applications. In particular, vortices are likely involved in both the mechanism used for the detection of photons, and in the generation of dark counts.

This section presents an investigation of individual vortices at the nanometer-scale in thin film MoSi, and their response to applied magnetic fields, focusing also on their dynamics and their relation to the pinning potentials. Indeed, spatial maps of the magnetic field above patterned MoSi wires are collected as a function of applied field and reveal the presence of individual vortices and their pinning sites. The vortex motion study was performed by imaging of individual superconducting vortices in amorphous thin-film MoSi with the SOT technique introduced in the second chapter. We characterized the pinning centers in this sample using the Field Cooling (FC) technique under certain conditions, which will be presented further in this chapter. From this study, we were able to classify different types of pinning sites as a function of their strength, and we were able to link each of these categories to a different behavior, like the presence of a long-lasting metastable vortex configuration or a thermal activated motion.

3.3.1 Sample Fabrication

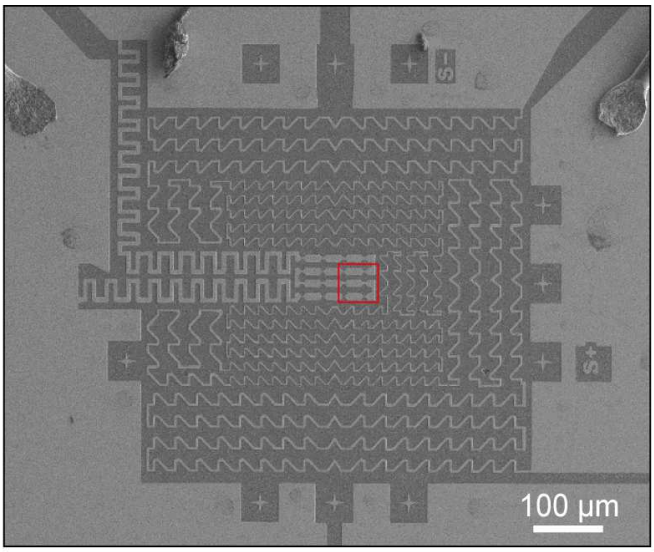

Figure 3.8: Wide-field SEM of the MoSi sample. The red highlighted square indicates where the magnetic maps were taken. Moreover it corresponds to the magnetic map reported in 3.7.

The 65 ± 5 nm-thick $Mo_{0.76}Si_{0.24}$ film is deposited onto an SiO_2 substrate by cosputtering with a DC and rf bias on Mo and Si targets, respectively. The thickness is determined using atomic force microscopy (AFM) and SEM, while the concentrations of Mo and Si are measured by x-ray photoelectron spectroscopy (XPS) [84]. The film is patterned into a series of meandering wires over a 500×500 μm^2 area by a combination of electron-beam lithography and reactive ion etching. The SEM image in Fig.3.8, shows both the sample and the marker serpentine used for SOT navigation, similarly to the CoFeB experiment. In this case the serpentine has been fabricated with the same material of the sample. In order to confirm the high purity of the MoSi wafers, we perform X-ray photoelectron spectroscopy (XPS) characterization of MoSi film used to produce the wire samples (Fig.3.9). Besides the two elements constituting the samples (Mo and Si), only oxygen and carbon are measured. Their presence is due to contamination as the samples are exposed to air during the process. Two fine scans of the Mo_3d and Si_2p regions are done to identify the different chemical states and are fitted to provide the most accurate composition calculations as possible. Both Mo and Si are found in a MoSi alloy state (227.6 and 99 eV, respectively) and oxide state (2232.2 and 102 eV, respectively), where the latter is expected due to air exposure. In terms of ele-

mental composition, the surface is composed of 24 at. % of Si for 76 at. % of Mo. The sample thickness was measured with a combination of different techniques, as shown in Fig.3.11. From both, contact-profilometer, and deg 45-tilted SEM, we were able to define the portion of MoSi damaged by the etching procedure. AFM helped us to confirm the estimations, and to refine the thickness at 65 ± 5 nm.

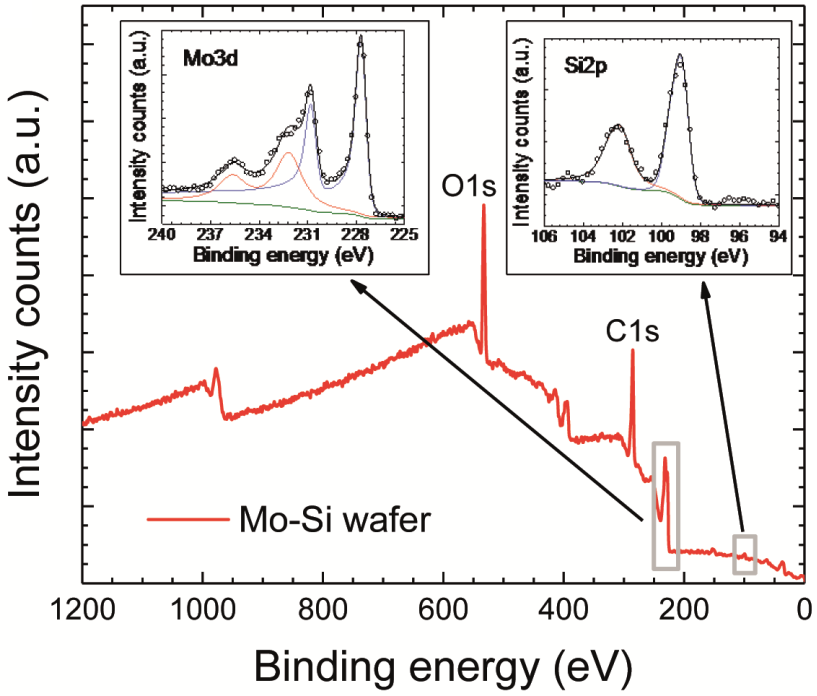

Figure 3.9: XPS characterization of the MoSi film shown in red. Two narrow scans of the Mo3d and Si2p regions are shown as insets. The shown spectra are normalized for comparison. The open circles are the measured data and the black lines correspond to the sum curve of all components represented in colored lines.

Through the SEM observation of the specimen surface, for both sample, and marker serpentine, we verified the presence of imperfections and damage. As one can notice, looking in Fig.3.10, holes are sporadically spread over the surface, in random way. These defects often correspond to strong pinning centers, with a deep pinning potential, as will be shown later. Moreover is possible to notice, that the edges are jagged. The possible influence of these edges, in the following magnetic profile analysis, has been considered through model parameters modifications, in function of empirical observations. Magnetic maps, in a complete virgin state after ZFC, were compared to the SEM images, in order to refine the Meissner shielding model used for the field screening calculations. This information is introduced

through the sample width as a fitting parameter. From these observations we deduce that the damaged area reduces the width of the superconducting film by ~ 150 nm.

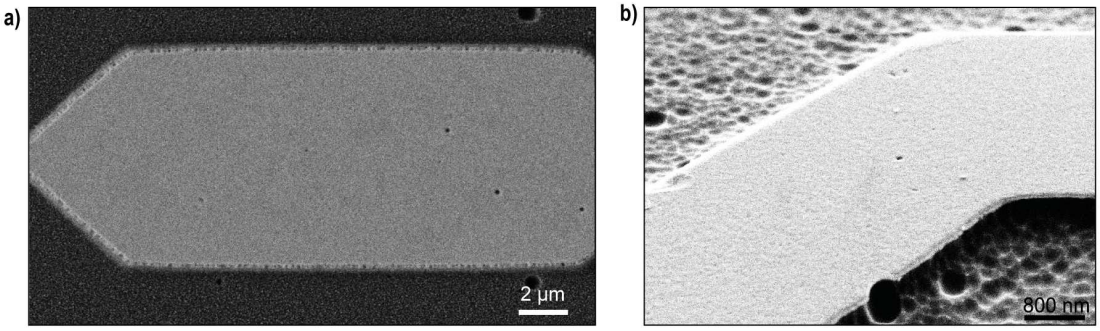

Figure 3.10: SEMs of MoSi sample with perpendicular top view a), and a tilted stage view, with an angle of $\sim$ deg 45 b).

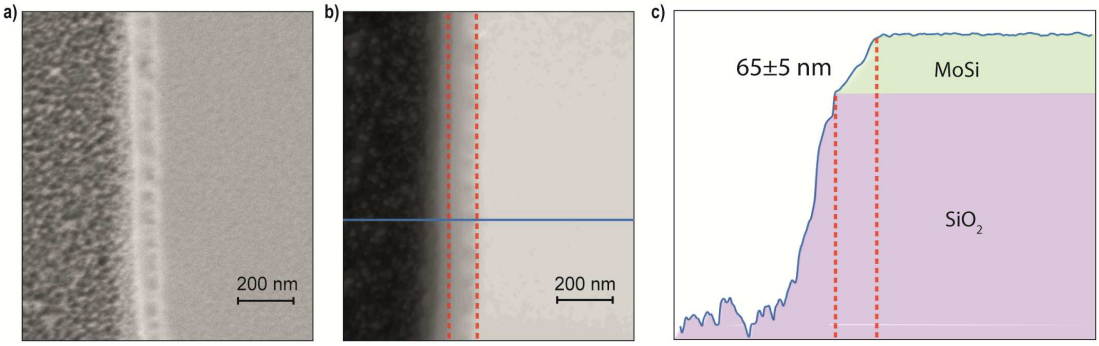

Figure 3.11: SEM and AFM of MoSi sample. a) SEM of an edge of the MoSi wire. The dark region is SiO2 and the light region is the MoSi. b) AFM image of the same region with dark contrast corresponding to low parts of the sample and light contrast to high parts of the sample. c) Line cut of the AFM in b).

3.3.2 Field Cooling at Low Field Regime

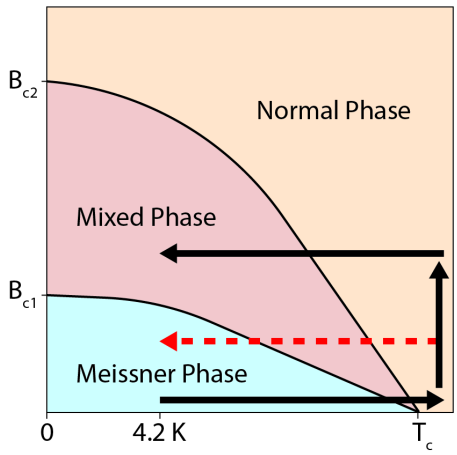

Figure 3.12: The diagram reports the three different phases for a type II superconductor as function of external magnetic field and temperature. This simple diagram is useful to describe the Field Cooling initialization procedure, modifying T and B to follow the path described by the black arrows. The red dashed arrow shows the initialization for low fields below B_{c1}, exploiting the residual magnetization presented in the first chapter to explain the presence of vortices despite B_a is not in the mixed state phase.

Before the comparison between the magnetic profile measured across the film and the fitting model it is useful to highlight the role of the FC technique, which has been use to initialize the vortex state in our sample. Fig.3.12 is a qualitative phase diagram (as a function of B_a and T) for a typical type II superconductor and helps to explain the FC initialization of the vortex state in our sample. Following the black arrows path, we warm up the sample with a local heater above T_c, and the film occurs in a complete transition in the normal state; at $T > T_c$, we apply an external field $B_a < B_{c2}$ and, keeping constant the field, we lower the temperature until $4.2K$ to freeze the magnetic flux in the mixed state. This is the usual initialization, that we also have performed at different fields, but our main observations on the MoSi film are taken initializing the vortex state below B_{c1} (red dashed arrow for the last initialization step). Indeed, as explained in the first chapter, the FC initialization produces an amount of residual magnetization, which in our case translates in non-zero vortex density, within the MoSi film. In the low field regime, in which we performed our measurements, this can not be neglected. The way that we used the FC initialization below B_{c1} is easily achievable with a simple process. Let's assume that we are working far below the threshold of the vortex entrance field, and the vortices, that we have in the FC initialized mixed

state emerge only from the interaction given by B_a and the strongest pinning centers in our sample. Therefore, after the initialization, if we increase B_a, but staying below the B_{c1}, we should not be able to see any vortex entrance from the sample edges, and the vortex density n_v should be stable.

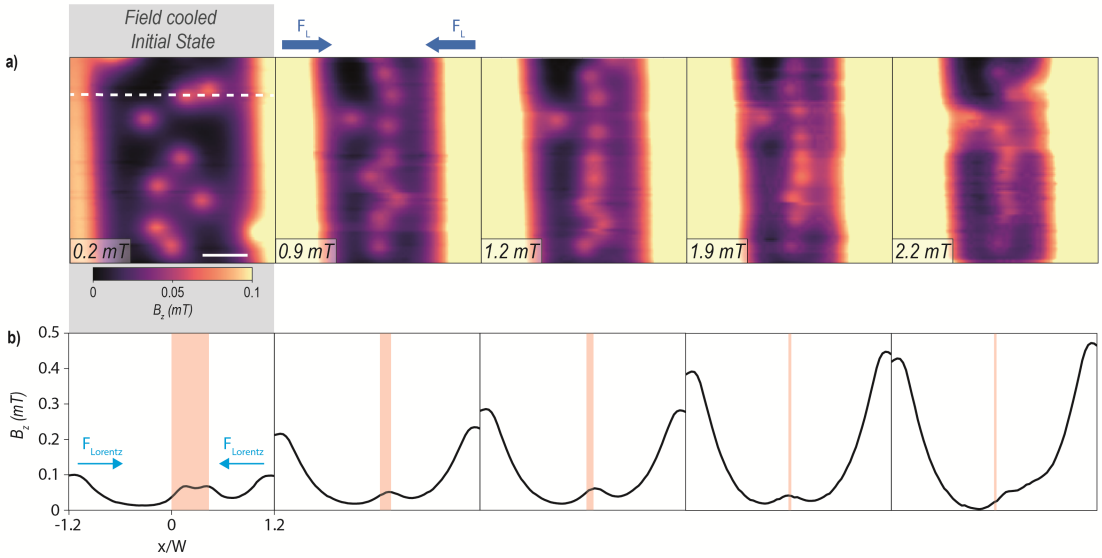

Figure 3.13: The sequence a) show the "squeezing" of the vortices, with a fixed colorbar in order to emphasize their motion under the Lorentz force effect. The intensity of the external field B_a shielded by the superconductor increases, and it saturates the colorbar, while the vortices maintain the same intensity. The dashed white line in the first map of a) represents the line of data, which are presented in b). These linecuts show the motion of the vortices towards the middle part of the MoSi film (difference highlighted by the red area), and the increase of the shielding effect and consequent flux line accumulation at the edges of the sample.

This behavior is shown in Fig.3.13. An almost constant vortex density does not imply that there is no vortex motion. Indeed, increasing B_a, produces an increase of the shielding current. Following the penetration flux model in the first chapter, an increasing current translates in a stronger Lorentz force, that drives the vortices towards the middle of the strip. It is possible to observe in Fig.3.13, that no nucleation from the edges is occurring in the raising of B_a. In Fig.3.14(a), more detailed maps of $B_z(x, y)$ taken after field cooling at $B_a = 0.5$ mT show a few isolated vortices. Line cuts across the MoSi wire through the center of a single vortex are shown for different z in Fig.3.14(b), and the dependence of the field as a function of z directly above the vortex is shown in Fig.3.14(c). These data are well fit by a model considering both the Meissner screening of the film [85] and the

field produced by a perpendicular vortex in a film such that its thickness $t << \lambda$ (thin-film limit) [18], as first described by Pearl [16] and Carneiro and Brandt [14] (see Appendix D at 4.4). Fits to these two effects measured at different z allow us to independently determine the Pearl length $\Lambda = 1\lambda^2/t$, and thus λ, as well as the real tip-sample spacing z for each measurement. At $4.2K$, we find $\Lambda = 8.1 \pm 0.9$ μm and a bulk $\lambda = 510 \pm 10$ nm, which agrees with measurements by Kubo of films with similar concentration and thickness [86].

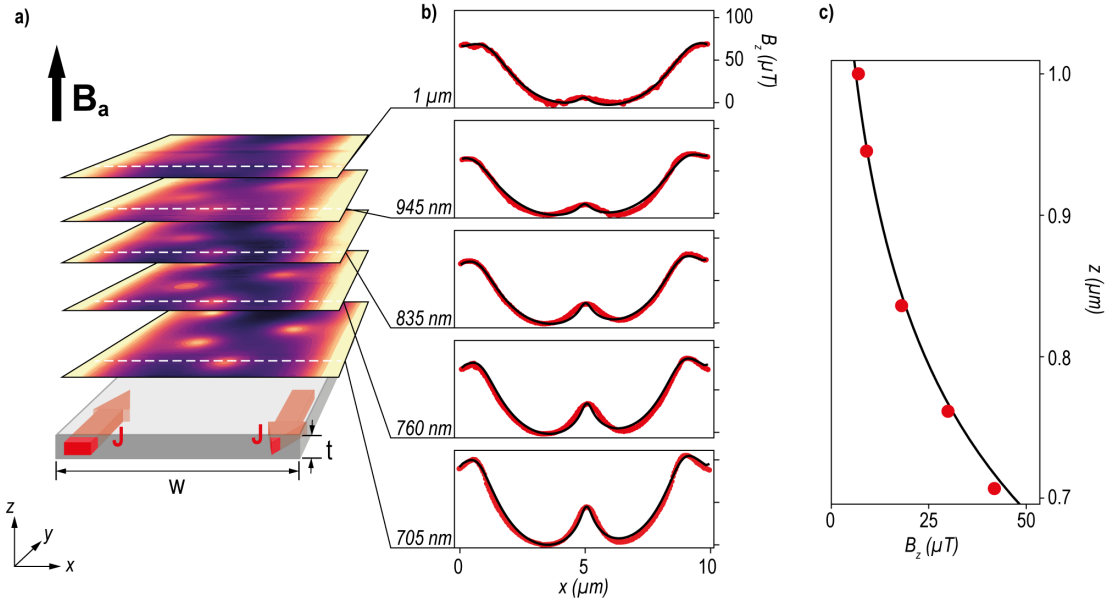

Figure 3.14: Fits to Pearl and Meissner models. (a) Schematic drawing of the MoSi wire with 2D measurements of $B_z(x, y)$ and (b) line cuts of $B_z(x)$ through a single vortex at different z (labeled) after field cooling at $B_a = 0.5$ mT. (c) Magnetic field directly above the vortex as a function of the tip-sample distance z, $B_z(z)$. Red dots in (b) and (c) represent measurements and black lines fits.

3.3.3 Dependence of Vortex Density on External Field

One of the main properties of the vortex trapping/nucleation is their density in function of the external applied magnetic field. By field cooling with different values of B_a, we initialize different vortex densities in the MoSi film, as shown in Fig.3.15.

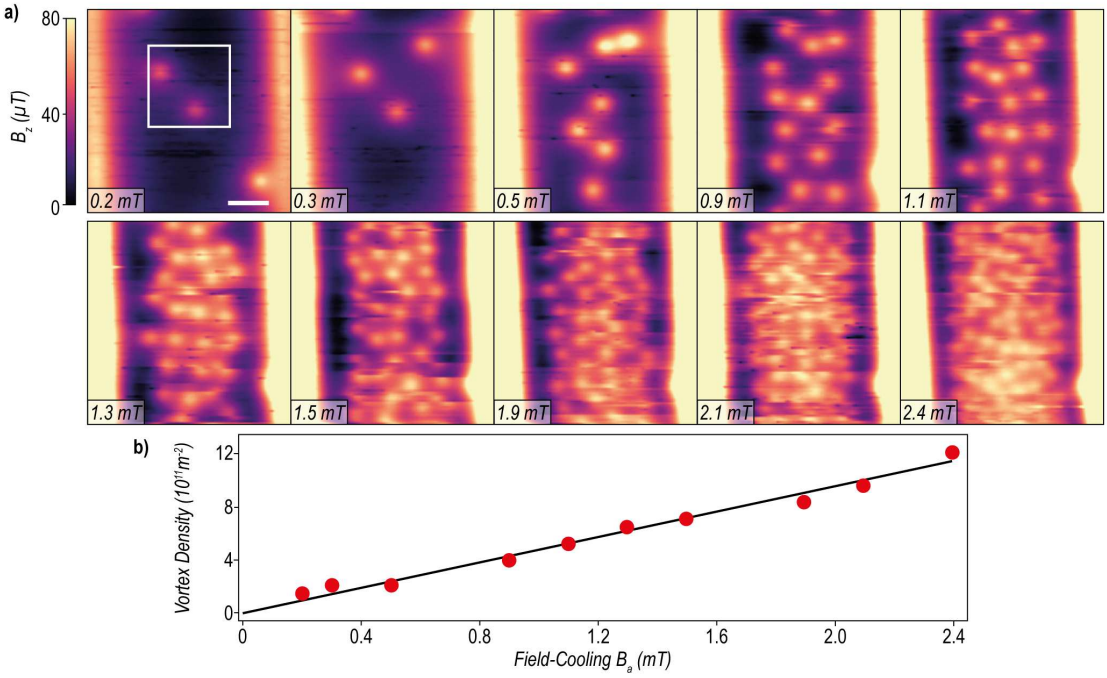

Figure 3.15: Vortex density as a function of applied field. (a) Maps of $B_z(x, y)$ taken at $z = 705$ nm over a MoSi wire segment after field cooling with increasing B_a, shown in the bottom-left corner of each image. Scale bar: 2 μm. (b) Vortex density in a 4×4 μm area at the center of the MoSi wire, delineated by the white box in (a), plotted as a function of the field-cooling field B_a. Data are shown as red dots, while the expected B_a/Φ_0 dependence is shown as a black line.

In the central region of the widest part of the wire, the measured vortex density depends linearly on B_a with slope given by Φ_0^{-1}, where $\Phi_0 = h/(2e)$ is the magnetic flux quantum, h is Planck's constant, and e is the elementary charge. In fact, the density should go as $(B_a - B_K)/\Phi_0$, where B_K is a critical induction below which no vortex trapping occurs, but because $B_K << B_a$ in our experiments, the measured results match theoretical predictions [35] as well as previous measurements in similar Nb [87] , yttrium barium copper oxide (YBCO) [35], and Pb [88] wires. This behavior corresponds to the vortex density expected when the total flux

through the film above T_c nucleates into vortices and is trapped within the film. However, when the entire area of the MoSi wire is considered, including the edges, the measured vortex density is significantly less than the full above-T_c flux density. The images of $B_z(x, y)$ in Fig.3.15 show vortex-free regions near the sample edges, which shrink with increasing B_a, as also observed in Pb films by Embon et al. [89]. This nonuniform vortex density, which is concentrated in the center of the wire, reflects the reduced effective width compared to the wire width, in which vortices can be trapped by the Meissner screening currents. In thin-film wires whose width $w >> t$, the screening current density decreases slowly from the edges, pushing vortices into the central part of the wire [19, 24, 33, 89]. As a result, flux threading the sample near its edges above T_c is subsequently expelled upon cooldown.

3.3.4 Inflated States and Vortex Expulsion

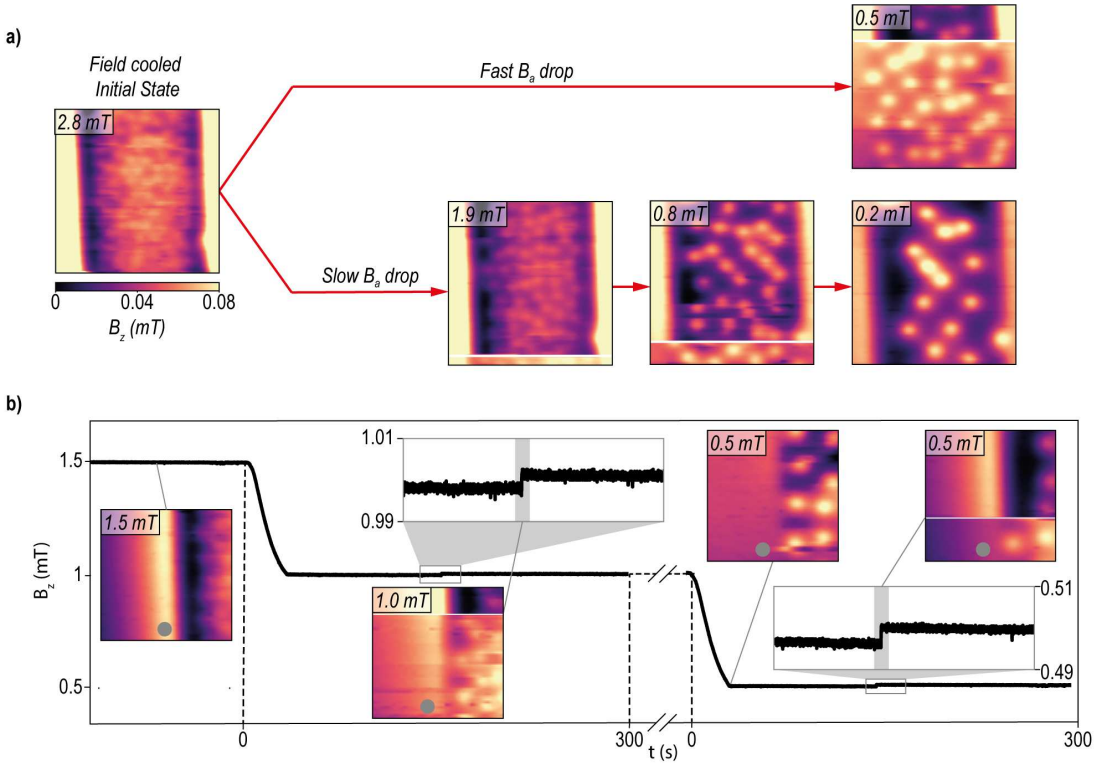

Figure 3.16: "Inflated" metastable vortex configurations. (a) Left image shows a map of $B_z(x, y)$ 705 nm over a MoSi wire segment after field cooling at $B_a = 2.8$ mT. The image on the top right shows a measurement of the same area immediately after a decrease of B_a to 0.5 mT in 30 s. The 10×10 μm^2 images are taken line-by-line in a total time of 260 s, with x as the fast axis (71 lines at 3.7 s/line). The white line represents the moment at which we observe a discontinuous change in the vortex configuration. The bottom-right images are taken at three fields as B_a is reduced from 2.8 to 0.2 mT. (b) $8.25 \times 8.25 \mu m^2$ images of $B_z(x, y)$ near the wire edge, each taken in a total time of $245s$ (51 lines at 4.8 s/line). (b) The leftmost image shows the configuration after field cooling at $B_a = 1.5$ mT. Other images show subsequent configurations after decreasing Ba to 1 mT and then to 0.5 mT. The plot displays B_z as a function of time at the position indicated by the gray circle, showing both the reduction in B_a and the signatures of vortex expulsion, which are highlighted in the zoomed-in sections. Note that the flux measured at this position (gray circle) and the spatial maps do not correspond to simultaneous measurements; they correspond to measurements carried out under the same initialization conditions. Therefore, the gray lines connecting the 2D maps to various points along the plot are meant to indicate similar events in different experimental runs, not two measurements of the same event.

In order to investigate the potential that traps the vortices, after field cooling we image the vortex configuration upon the reduction of B_a. The left panel of Fig.3.16(a) shows an image of $B_z(x, y)$ after field cooling at $B_a = 2.8$ mT to 4.2 K. The panels on the right show the same region immediately after ramping the applied field down to lower B_a at constant temperature. In the case shown in the top half of Fig.3.16(a), the field is ramped down $B_a = 0.5$ mT in 30 s and the 10×10 μm^2 image is taken line-by-line in a total time of $260s$ with x as the fast axis. Towards the end of the image, after 200 s, we observe a sudden change of the vortex configuration. The system goes from an inflated state, in which vortices appear in the previously unoccupied edge region, to a state similar to that observed after field cooling, containing fewer trapped vortices and vortex-free edges. Upon further repeated imaging, the second configuration is always observed, except for small changes due to thermally activated vortex hopping, which will be discussed in the next section. In the bottom half of Fig.3.16(a), the field is reduced in three steps to $B_a = 0.2$ mT, with similar discontinuities marking a transition between inflated and equilibrium states showing up in the images taken at $B_a = 1.9$ and 0.8 mT. The panels of Fig.3.16(b), showing a 8.25×8.25 μm^2 view of $B_z(x, y)$ near the wire edge, display similar behavior 190 s after B_a is reduced from 1.5 to 1.0 mT and 320 s after it is subsequently reduced to 0.5 mT. In particular, we note that in the inflated states observed at 1.0 and 0.5 mT, the vortices in the edge region appear pinned to the same set of pinning sites. Such vortex expulsion behavior is observed repeatedly for similar intervals of B_a and over similar time scales at constant temperature.

To confirm that transitions from the inflated state to the final state are not induced by interactions with our scanning tip [90], we carry out the same measurements with the SOT at a fixed position, just outside the edge of the sample, as marked by the gray circles in Fig.3.16(b). Once again, B_a is reduced at a constant temperature and the resulting field B_z next to the wire is plotted as a function of time in the main part of Fig.3.16(b). After the initial reduction due to the ramping down of B_a, B_z is constant until around 150 s, when it increases in a sudden step. This increase corresponds to the expulsion of the extra vortices present in the inflated state (for an other example see Appendix C at 4.3. Vortex expulsion with similar time scales is observed upon repeated experiments and for different fields. Since this behavior corresponds to what was observed in the scanning experiments, we rule out interactions with the tip as the trigger for the observed flux expulsion. Although strong interactions were previously observed between vortices in YBCO and a magnetic force microscopy tip [91], the much weaker stray fields produced by our SOT tip produce a negligible perturbation to each vortex, calculated to be less than 10 fN following the procedure described by Embon et al. [88].

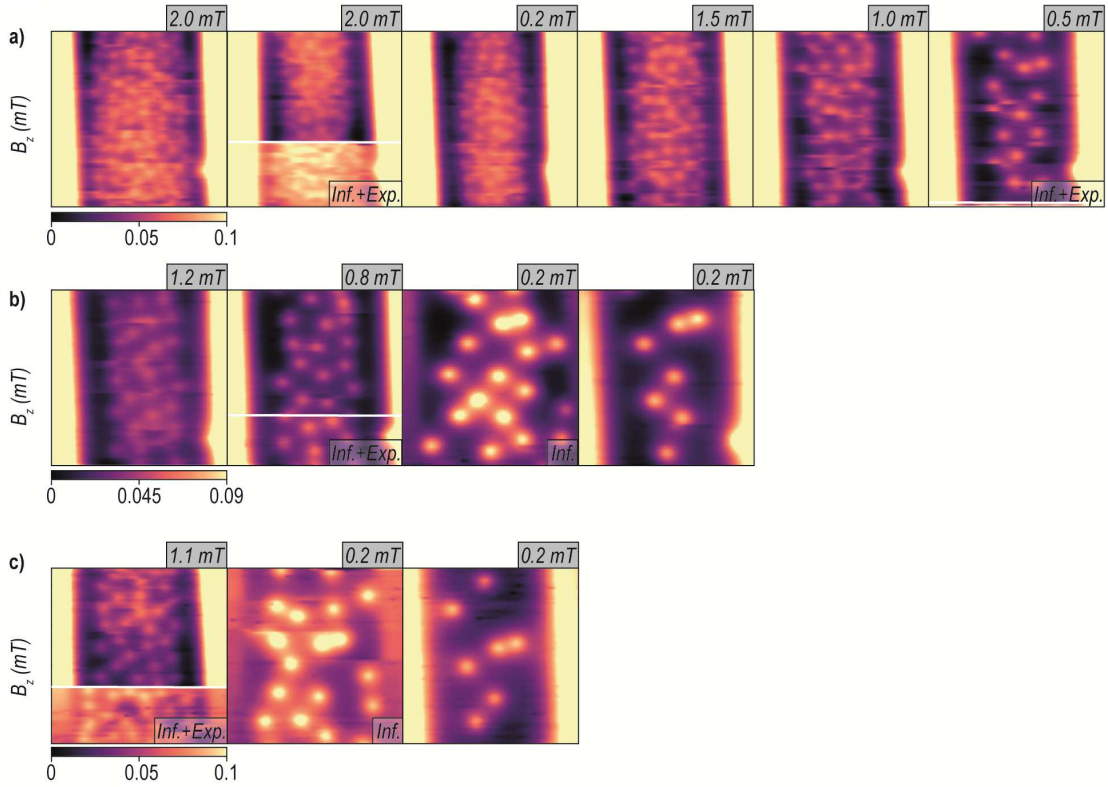

Figure 3.17: Three different external field sweeps, which present one or more inflated states followed by a vortex expulsion. The white lines indicate the moment when the vortex expulsion occurs, during the scan. The scan direction is line by line from bottom to top, and from left to right. Eventually, the vortex expulsion can occur between two scan runs, like in b) at 0.2 mT, or c) at 0.2 mT. In this case the vortex configuration appears drastically changed from one scan to another. Another interesting observation, which characterize the inflate state, is the brighter signal of vortices compared to the signal, produced by the distorted flux lines at the sample edges.

3.3.5 Pinning Center Classification

The presented measurements were used to categorize the pinning centers in our sample, and to produce an analysis of the pinning energies. To simplify, we divided the pinning potential in three different categories:

- Strong Pinning Centers: no dynamics are observed by either thermal or external excitation.
- Medium Pinning Centers: motion can be driven by external excitation.
- Weak Pinning Centers: thermally driven motion observable.

Strong Pinning Centers

In this group we identified the most strongly pinned vortices. These vortices show no motion, neither for thermal activation nor for external inputs, like the application of AC or DC currents. These quantized fluxes are fixed regardless the external field applied after the FC initialization. They disappear only above B_{c2}, or applying an opposite sign field, large enough to contrast completely the remanent magnetization.Usually, these type of pinning sites are patterned intentionally during the sample fabrication in order to avoid any dissipation, which can affect the results of a superconductivity-based devices, like SNSPDs or superconducting qubit. In the MoSi sample, these pinning centers can be visible also by SEM images, e.g. Fig.3.10, where we found a local correspondence between the vortex presence, and holes on the surface. In the magnetic maps reported in this thesis some of the strong pinning centers are easily recognizable, since they are able to trap the magnetic flux even in areas where the vortex presence would not be allowed, e.g. in proximity of the film edges (see Fig.3.13(a)).

Medium Pinning Centers

Although many pinning sites exhibit thermally activated vortex hopping, some sites do not, pointing to deeper trapping potentials. We further investigate these sites by driving vortex motion using an AC current I_{AC} applied along the y direction (long direction of the wire). This current results in an ac Lorentz force $F_{AC} = \frac{I_{AC}}{w}\Phi_0$ on each vortex along the x direction. F_ac drives oscillations of the vortices around their equilibrium positions. The resulting motion can be measured using the scanning SOT as either a blurred vortex image in $B_z(x, y)$, as shown in the left panel of Fig.3.18(b), or, more clearly, as a dipolar signal in the magnetic field produced by the sample at the frequency of the ac current drive $B_{z,AC}(x, y)$,

as shown in the right panel [88]. The amplitude of this signal reflects the size of the oscillation and the gradient of the static field $B_z(x, y)$ produced by the vortex.

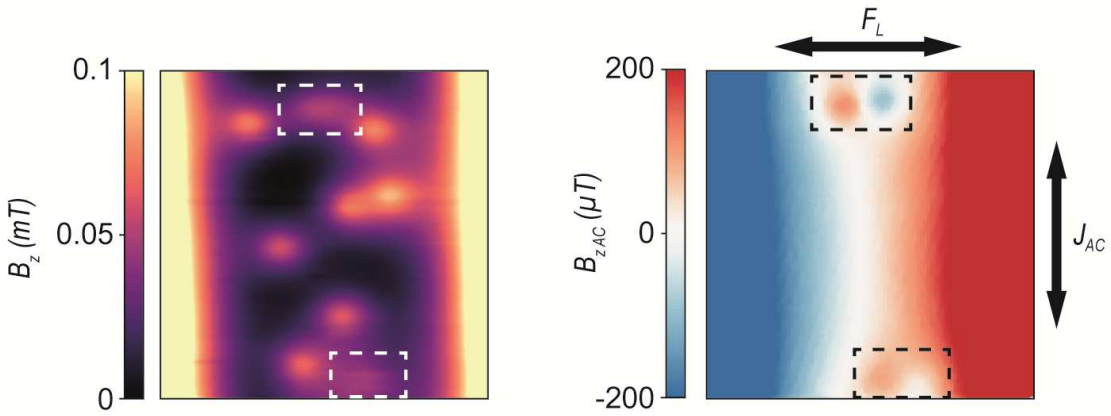

Figure 3.18: Pinning strength. The image is a map of $B_z(x, y)$ at $z = 705$ nm over a MoSi wire segment after field cooling with $B_a = 0.8$ mT, in presence of an ac applied current along $\hat{y}$, producing a F_{AC} along $\hat{x}$. The right image shows $B_{z,AC}(x, y)$, which is measured simultaneously. The highlighted areas show vortices which oscillate as a result of F_{AC}. Scan area 10×10 μm^2.

Vortices at different pinning sites respond differently to F_{AC}, indicating the varying strength of the pinning potentials throughout the sample. At $B_a = 0.9$ mT, weak pinning sites (30%), showing thermally activated hopping, are induced to jump from site to site by F_{AC} with amplitudes in the 100-fN range. Strong pinning sites (50%) show no measurable response to this F_{AC}. Intermediate pinning potentials (20%) show oscillatory responses to the F_{AC}. From the strength of F_{AC}, we extract effective pinning spring constants of around 0.6 μN/m. Compared to similar measurements in Pb films, these potentials are 100 times shallower (less curvature), indicating their larger spatial extent and weaker strength. By increasing Lorentz force up to a maximum value F_{AC}, max at which these vortices escape from their pinning sites, we can integrate and estimate the depth of the potential well, typically obtaining $E_{pin} \approx 60$ meV.

Weak Pinning Centers

The presence of thermally activated vortex hopping at 4.2 K is evident from repeated imaging of $B_z(x, y)$ at equilibrium. As shown in Fig.3.19, certain vortices are seen to jump between neighboring pinning sites within a single image or between successive images. The former effect is evident in the discontinuities between

one x line and the next, while the latter can be seen when a vortex changes position between images. These jumps occur on a time scale ranging from a few to a few hundred seconds. Given this time scale and the similar time scale of the metastable configuration held together by pinning sites at the sample edges, we estimate the depth of these pinning potentials E_{pin} using the Boltzmann formula for a thermally activated hopping rate: $\nu_{hop} = \nu_0 e^{-\frac{Epin}{k_B T}}$, where k_B is the Boltzmann constant, T is the temperature, and ν_0 is the attempt frequency. Solving for E_{pin}, we find an energy between 4 and 12 meV, whose uncertainty results from the imprecisely known ratio of $\frac{\nu_0}{\nu_{hop}}$ (ν_{hop} ranges from a few mHz to 1 Hz, while ν_0 is assumed to lie between 105 and 1012 Hz [3, 90]). These weak pinning sites are therefore not strong enough to freeze vortex motion at 4.2 K and thus provide a path through which the system can eventually find its equilibrium configuration.

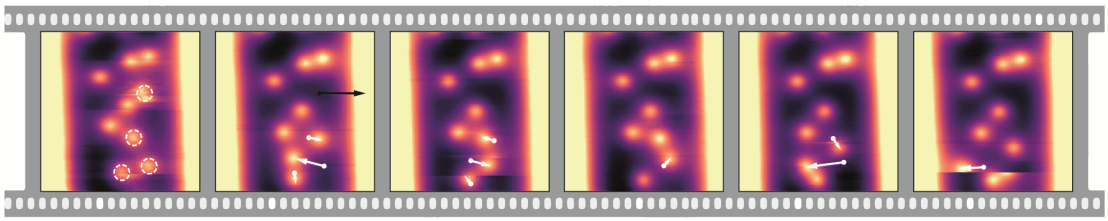

Figure 3.19: Thermally activated vortex hopping. Maps of $B_z(x, y)$ at $z = 705$ nm over a MoSi wire segment after field cooling with $B_a = 0.8mT$. Each $10 \times 10\mu m^2$ image is of the same region and is taken one after the other line-by-line in 260 s with x as the fast axis (71 lines at 3.7 s/line). Circles and arrows highlight vortices hopping between neighboring pinning sites.

As B_a is increased, we note that pinning sites displaying thermally activated hopping occur more frequently from 25% of pinning sites at $B_a = 0.6$ mT to up to 85% at $B_a = 1.5$ mT. As the vortex density increases, stronger vortex-vortex interactions, which have a long-range $1/r$ force in thin films, destabilize an increasing number of vortex pinning sites. As the field-cooling field Ba is increased, the proportion of pinning sites showing thermally activated vortex hopping increases. The increasing vortex density results in stronger vortex-vortex interactions, which destabilize more and more vortex pinning sites. This effect can be observed in Fig.3.21, which shows three sequences of images taken one after the other for three different field-cooling fields $Ba = 0.6, 0.8$, and 1.0 mT. Each frame requires 153 s to measure, and successive images are taken immediately after the previous image finishes. As shown in Fig.3.20, the proportion of pinning sites showing thermally activated vortex hopping, $R = \frac{n_m}{n_t}$, where n_m is the density of vortices showing thermally activated hopping and n_t is the total vortex density, increases with Ba until nearly all vortices show thermally activated behavior.

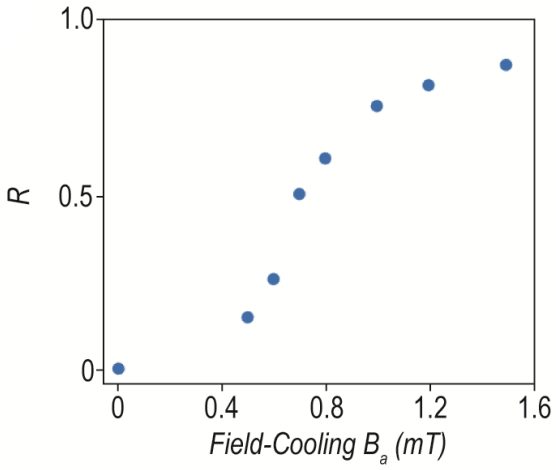

Figure 3.20: Proportion vortices showing thermally activated hopping as a function of B_a in measurements like those shown in Fig.3.21.

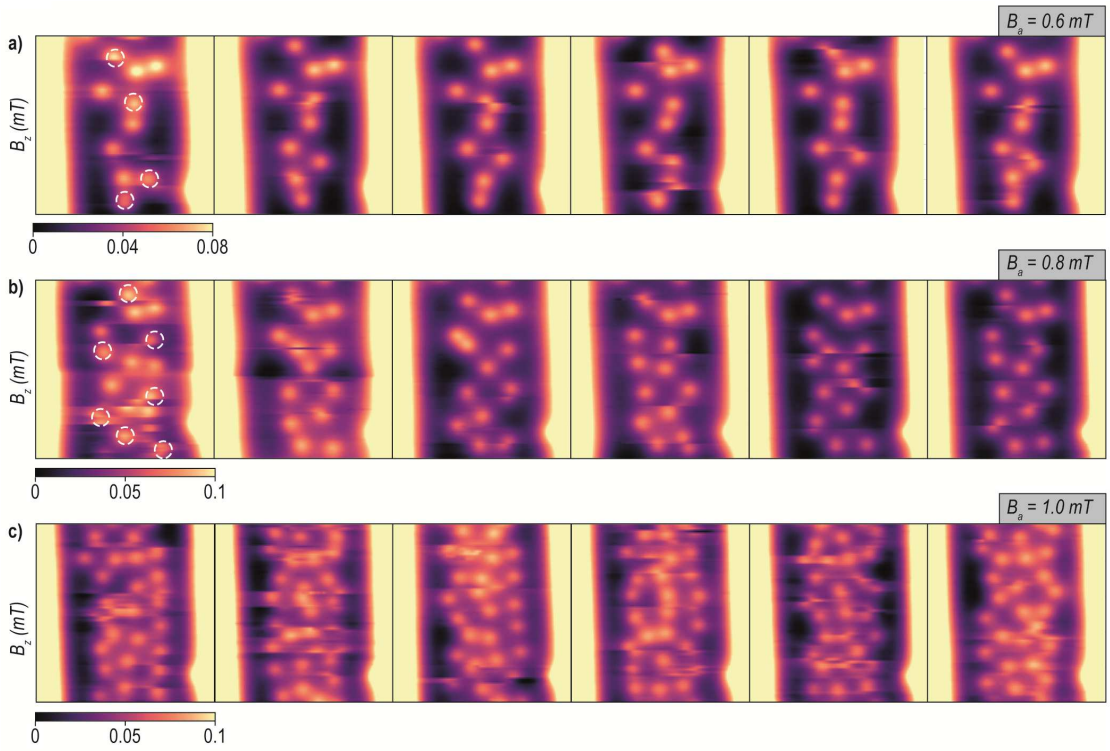

Figure 3.21: Dependence of thermally activated vortex hopping on applied field. (a-c) Time series of images of $B_z(x, y)$ taken at three different field-cooling fields B_a. Dashed circles in (a) and (b) highlight vortices which hop in subsequent frames. Given the large proportion of vortices hopping in (c), we do not highlight them there.

Conclusions

The high magnetic and thermal sensitivity, together with a tunable spatial resolution, makes the SOT one of the most powerful SPM magnetometer techniques for cryogenic measurements. In this work we have shown its potential, presenting two experimental results which span on different aims, and requiring different approaches from both the theoretical and experimental point of view. In the following, we want to summarize the results and conclusions for each experiment, and then we will give an outlook for possible future applications and improvements.

Conclusions for CoFeB FNT Study

From previous experiments [41], it emerges that, for FNTs of cross-sectional dimensions between 200 and 300 nm, and longer than 2 μm, the equilibrium remnant state at room temperature is the mixed state, while shorter FNTs favor global or opposing vortex states. With our experiment for the first time, we confirmed these observations in individual FNTs, by mapping their magnetic stray field, rather than their magnetization. In this way, we directly image the defining property of flux-closure configurations, that is, the extent to which their stray field vanishes. Indeed, we find that the imperfect geometry of the FNTs causes even the global vortex state to produce stray fields on the order of 100 μT at a distance of 300 nm. Finer control of the sample geometry is required in order to reduce this stray field and for such devices to be considered as elements in ultrahigh density magnetic storage. Nevertheless, the global vortex is shown to be robust to the imperfections of real samples; despite slight distortions, it continues to be dominated by a single azimuthally aligned vortex.

Conclusions for Thin Film MoSi Study

Our scanning SOT experiments, because of the sensor's combination of high spatial resolution and high magnetic field sensitivity, reveal images of individual super-

conducting Pearl vortices in amorphous MoSi thin films. In addition to providing a measure of the penetration depth of the film, we directly observe their thermally activated hopping at 4.2 K. Since the vortices are not completely frozen onto their pinning sites, we are able to estimate the depth of the weakest pinning potentials and observe metastable vortex configurations present for tens of seconds before the system reaches equilibrium. The dynamic nature of the vortex configurations in MoSi at 4.2 K may have implications for SNSPDs and other devices fabricated from such films. The thermally activated vortex hopping observed here may be a source of residual dark counts in SNSPDs. Our experiments also make plain the necessity of further reducing the density of unintentional pinning sites by improving sample quality. In order to aid in the optimization of MoSi-based superconducting devices, future scanning SQUID studies should aim to study different MoSi films grown under different conditions.

During our work, on both the results presented, we had the opportunity to spot the strongest and weakest points of our technique, allowing us to study many possible improvements for our probe. As said the strong sensitivity itself is the main advantage for this technique. As explained in the second chapter, the SOT configuration, with the SQUID's junctions in the sample proximity, has a strong benefit in the ability of collecting thermal measurements as shown by Halbertal et al.[92]. Indeed, the two weak links forming the two Josephson junctions are locally close to the sample, contrary to the planar SQUIDs, where the two junctions are far from the superconducting pick-up loop, which traps the magnetic flux. Since the superconducting state is broken easier through the Dayem bridges than on the rest of the superconducting part of the probe, the thermal energy produced by the sample, influences the critical current at which the transition occurs, and showing then a temperature dependence. This sample-probe thermal coupling is dependent on the sample-probe distance and the vacuum quality inside the microscope. The second element is the reason to introduce a small amount of ^{4}He as exchange gas to enhance the coupling. This thermal sensing resulted an important advantage during the MoSi experiment, where the local or global transition from superconducting state to normal state is followed by a sudden appearance of dissipation phenomena.

One of the main downsides we have spotted for our probe is the complication of driving the SOT sensor in proximity of the sample, avoiding possible contacts. Due to the quartz structure of our tip, the probe is really fragile, and in contrast with other techniques, even a soft crash can destroy completely our sensor. To solve this problem we took inspiration from the work made by Zeldov group, developing our own version of a SOT coupled to a mechanical resonator, using a tuningfork with qPlus configuration. Some early results are presented in Appendix H at 4.8, where

we were able to use our SOT, coupled with a qPlus (qSOT), for both magnetic and non-contact AFM measurements on a niobium sample. The qSOT will allow us to tune and control the probe-sample distance, and our intention is to implement as a standard feature in our experimental setup.

A second downside is the strong oxidation of the Pb layer, which is deposited, as core part of the SQUID, on the apex of our quartz pulled tip. This oxidation prevents us from the possibility to work on our SOT at lab conditions (e.g. temperature and humidity), longer than $30 - 45$ minutes. This means that, at the end of fabrication process, we need to minimize the time in air of our probe. This obstacle influences the time we can use during the mounting procedure in our microscope, and it does not leave room for many mistakes. Among the possible solutions, that we are going through to solve this problem, we are considering to change the superconducting material to deposit on the quartz tip. This possible solution would also bring other side advantages, since a different superconductor means different environment working conditions (e.g. T_c, J_c, B_c, etc.). At the end, we want to outlook to next possible application for our probe. We are considering the investigation of many interesting samples, on which the scientific community is focused on. Possible examples are:

- Twisted bi-layer graphene. It is one of the most intriguing materials, which recently captures the attention of the scientific community, showing superconducting state under certain fabrication and experimental conditions. Previous measurements done on mono-layer graphene samples, for the investigation of quantum Hall state and the dissipation created by the edge currents [93–95], allow to assume the SOT as a powerful tool for the investigation on the new physics behind these new devices.

- Magnetic skyrmions. These topological protected spin textures are one of the most recently studied topics in the solid state physics [96–99]; while the theoretical physics is highly prolific on this topic [100, 101], the SOT technique, with its high sensitivity and sub-100 nm resolution would be able to measure their magnetic configurations and their stray field. The fast scanning procedure presented in this thesis highlights how also the skyrmion dynamics is open for investigations.

- SNSPDs devices. These devices reached a high efficiency ($> 90\%$) at wide ranges of wavelengths (from x-rays to mid-infrared) and low dark count rate (< 1 Hz) in recent years [102–104]. In this work has been shown the high flux sensitivity and resolution of the SOT scanning probe, which provides an unparalleled tool for studying vortex dynamics, potentially improving our understanding of their complex interactions. Controlling these dynamics in

amorphous thin films is crucial for optimizing SNSPDs (the most efficient of which are made from MoSi, WSi, and MoGe) because vortices are likely involved in both the mechanism used for the detection of photons and in the generation of dark counts [83].

Besides the reported examples, other experiments are under consideration in our laboratory, as the study of superconducting proximity effects or the superconducting-ferromagnetic interaction in multilayer samples, without losing the focus on possible improvements and technical upgrades for out SOT scanning probe itself.

Appendices

4.1 Appendix A: Mumax3 Simulations

To simulate the CoFeB FNTs, we set $\mu_0 M_S$ to its measured value of 1.3 T and the exchange stiffness to $A_{ex} = 28$ pJ/m. The external field is intentionally tilted by deg 2 with respect to $\hat{z}$ in both the xz- and the yz-plane, in order to exclude numerical artifacts due to symmetry. This angle is within our experimental alignment error. The asymmetry in the magnetic cross-section of an FNT, seen in 3.2 1e, is generated by removing a hexagonal core from a larger hexagonal wire, whose axis is slightly shifted. In this case, the wire's diameter is 30 nm larger than the core's diameter and we shift the core's axis below that of the wire by 5 nm. In order to rule out spurious effects due to the discretization of the numerical cells, the cell size must be smaller than the ferromagnetic exchange length of 6.5 nm. This criterion is fulfilled by using a 5 nm cell size to simulate the 0.7 μm long FNT. For the 4 μm long FNT, computational limitations force us to set the cell size to 8 nm, such that the full scanning field can be calculated in a reasonable amount of time. Given that the cell size exceeds the exchange length, the results are vulnerable to numerical artifacts. To confirm the reliability of these simulations, we perform a reference simulation with a 4 nm cell size. Although the magnetic states are essentially unchanged by the difference in cell size, the value of the stray field is altered by up to 10%.

4.2 Appendix B: SEM FNTs

In the first experiment presented, we shown the stray field produced by CoFeB nanotubes under the effect of an external magnetic field. We needed a precise selection of nanotubes lengths for the investigation. Thus we used focused ion bean technique (FIB) to cut the nanotubes for the wanted length, as shown in Fig.4.1.

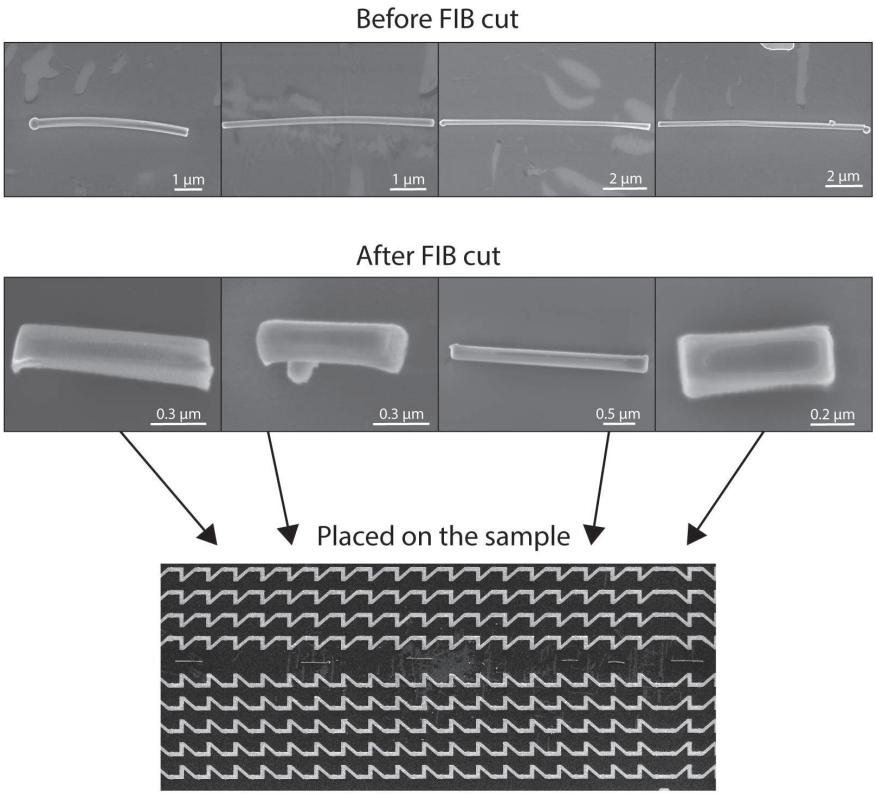

Figure 4.1: SEM images of the CoFeB nanotubes investigated in the first experiment, before(first line) and after (second line) the FIB cut. Last image shows their position in the middle of the marker serpentine, which we used for navigation with the SOT.

4.3 Appendix C: Vortex Expulsion Graphs

In the MoSi experiment description in the third chapter we presented the vortex expulsion phenomenon, which we observed at different rates and conditions. Anyway, in Fig.3.16(b), only one example of parallel measurements is reported. In the following image we want to present other example to extend the overview.

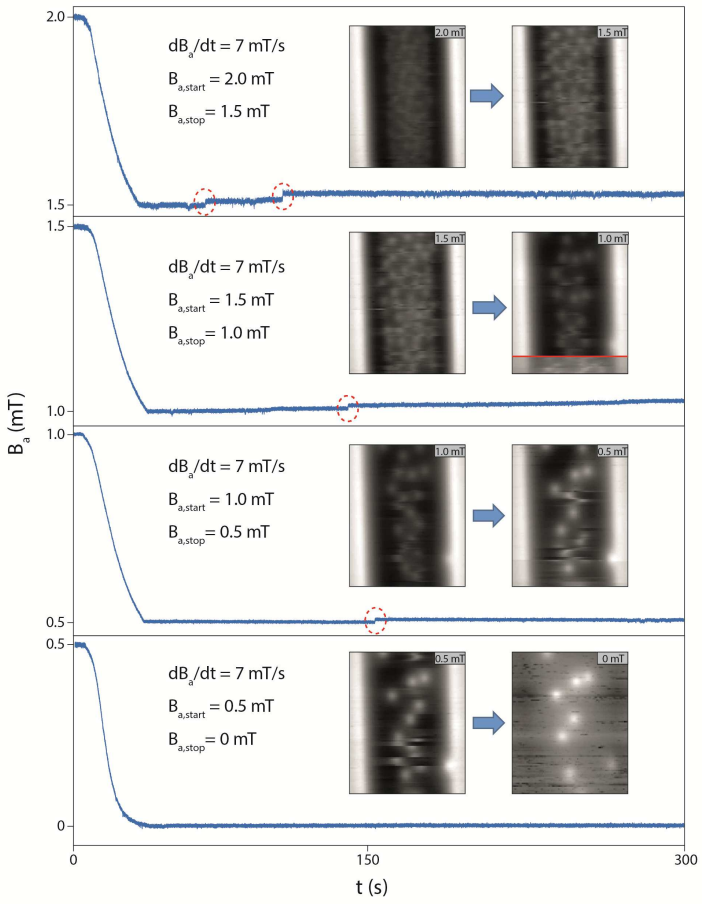

Figure 4.2: Examples of vortex expulsion process, measured at different initial ($B_{a,start}$) and final ($B_{a,stop}$) magnetic fields, and for different field reduction rates. For each of these examples, we report both the images taken before and after the expulsion occurred, and the fixed position measurements over 5 minutes.

4.4 Appendix D: Model for Magnetic Field Above Thin-Film Wire

The model used to fit the spatial dependence of B_z above the superconducting MoSi wire considers the wire's expulsion of flux due to the Meissner effect and the field produced by a superconducting vortex in the Pearl limit. By summing the resulting field profiles, we model the 1D profile shown in Fig.3.14(b) and Fig.3.14(c), which cut through the center of the field produced by a single vortex in the wire. The model for the field produced by Meissner screening follows Brisbois et al. [85]:

$$B_{z,Meissner}(x,z) = 1 + \frac{1}{\pi}\int_{-\frac{w}{2}}^{\frac{w}{2}} \frac{(x-s)sds}{\left[(x-s)^2+z^2\right]\sqrt{\left(\left(\frac{w}{2}\right)^2 - s^2\right) + \frac{8a\lambda^2}{\pi t}}} \tag{4.1}$$

The model for the field produced by the superconducting vortex is based on Pearl's model, because the wire thickness is much less than the penetration depth ($t << \lambda$) [14, 16]:

$$B_{z,Vortex}(x,z) = \Phi_0 \int_{-\frac{1}{L}}^{\frac{1}{L}} \frac{d^2k e^{ik\cdot x}}{4\pi^2\left(1+\frac{4k^2\lambda^4}{t^2}\right)} f(k,z) \tag{4.2}$$

where $f(k,z) = c_1 e^{-kz}$ above the film, i.e., for $z > 0$, where 0 is the surface of the film. c_1 depends on the film thickness t:

$$c_1(k) = \left[(k+\rho)\,e^{\rho t} + (k-\rho)\,e^{-\rho t} - 2k\right]\frac{\rho}{c_2} \tag{4.3}$$

$$c_2(k) = (k+\rho)^2\,e^{\rho t} - (k-\rho)^2\,e^{-\rho t} \tag{4.4}$$

$$\rho = \sqrt{k^2 + \left(\frac{2\lambda^2}{t}\right)^2} \tag{4.5}$$

4.5 Appendix E: Microscope Pictures

In the second chapter, we presented a 3D rendering of the microscope in Fig.2.3, that we used during the experiment presented in this work. Here, we show the actual picture of the microscope.

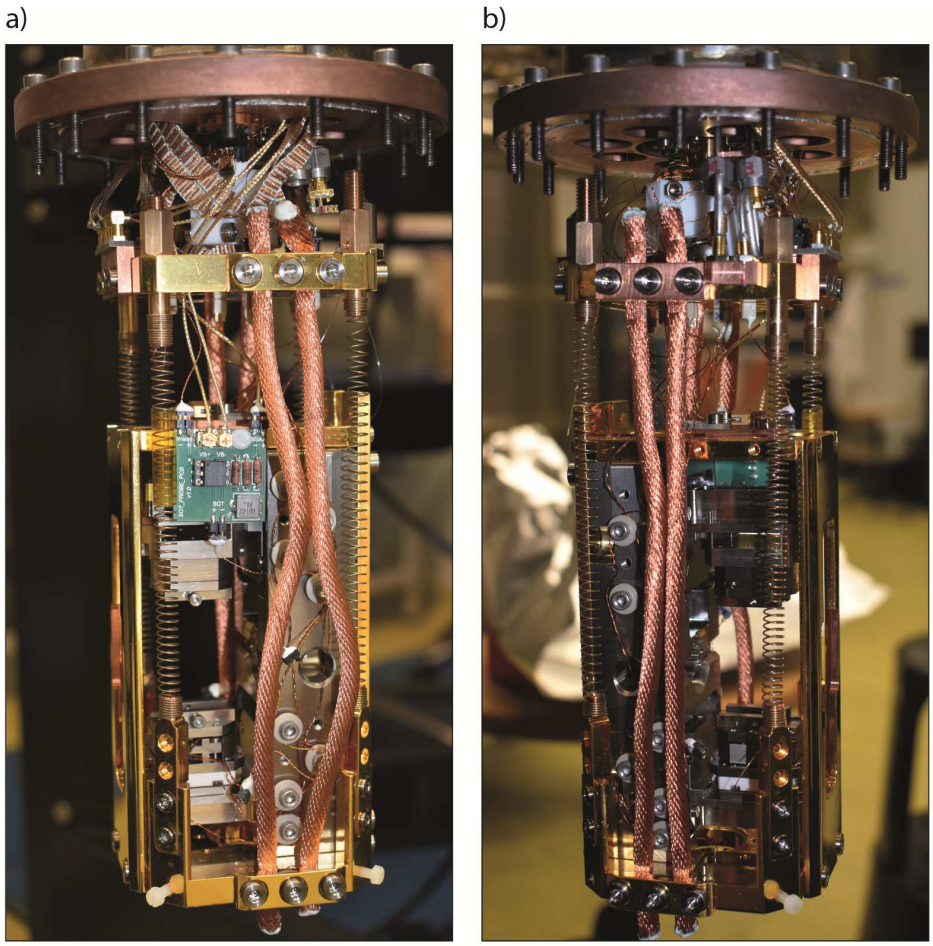

Figure 4.3: The figure shows two pictures of the microscope used for both the experiments presented in this thesis. a) right side, and b) left side.

4.6 Appendix F: SOT Fabrication

As explained in the second chapter, the SOT fabrication consists in many steps, ans two of them regard two different evaporation processes. The first evaporation is made in a commercial e-beam evaporator, and it allows us to deposit two long Au contacts along the pulled quartz tip, and an Au short close to the apex of the tip, as shown in Fig.4.4. The second type evaporation is made in a custom-made evaporator reported in Fig.4.5. During this process we evaporate the Pb on the final part of the tip, which forms the SQUID on the tip's apex.

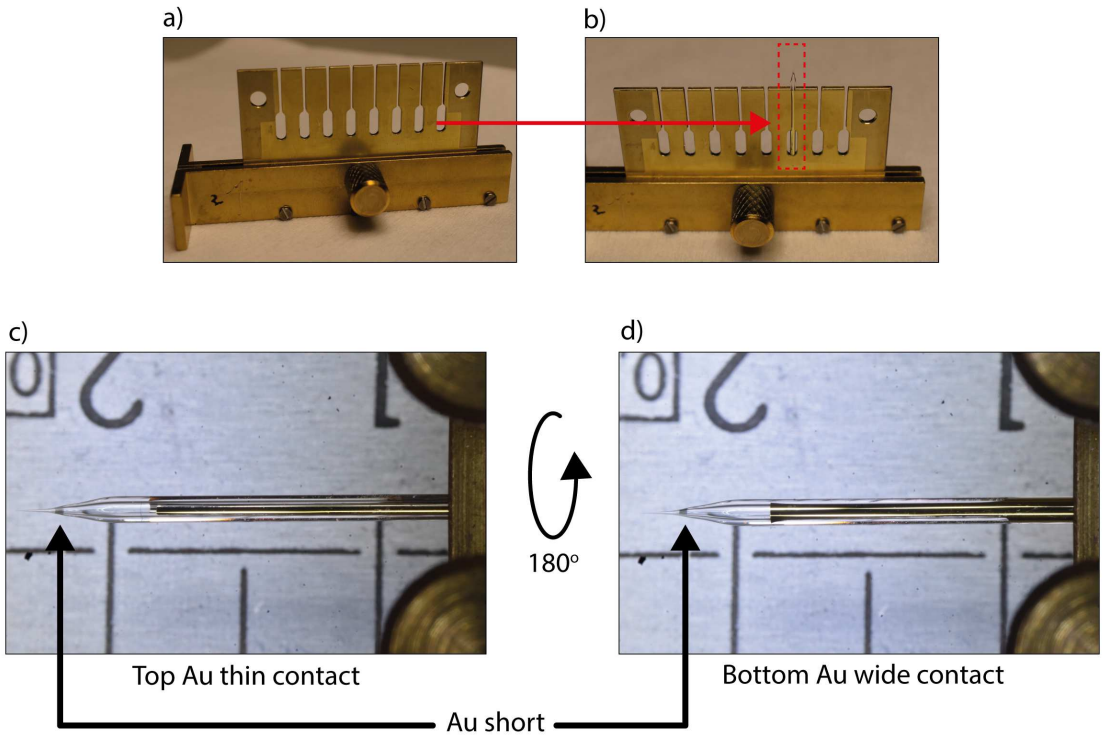

Figure 4.4: In the first line of this image, we show two pictures of the evaporation mask used for the gold evaporation. a) is the grid which can guest a set of 8 quarts tips, and in b) is shown an example of how a tip is fitting in the mask frame. In the second line of the image, we show a zoom-in of a quartz tip after the Au evaporation. c) the top Au contact is smaller to prevent shorts in the SOT holder used to mount in the microscope. d) shows the bottom Au contact. In both c) and d) is visible the Au short evaporated close to the apex.

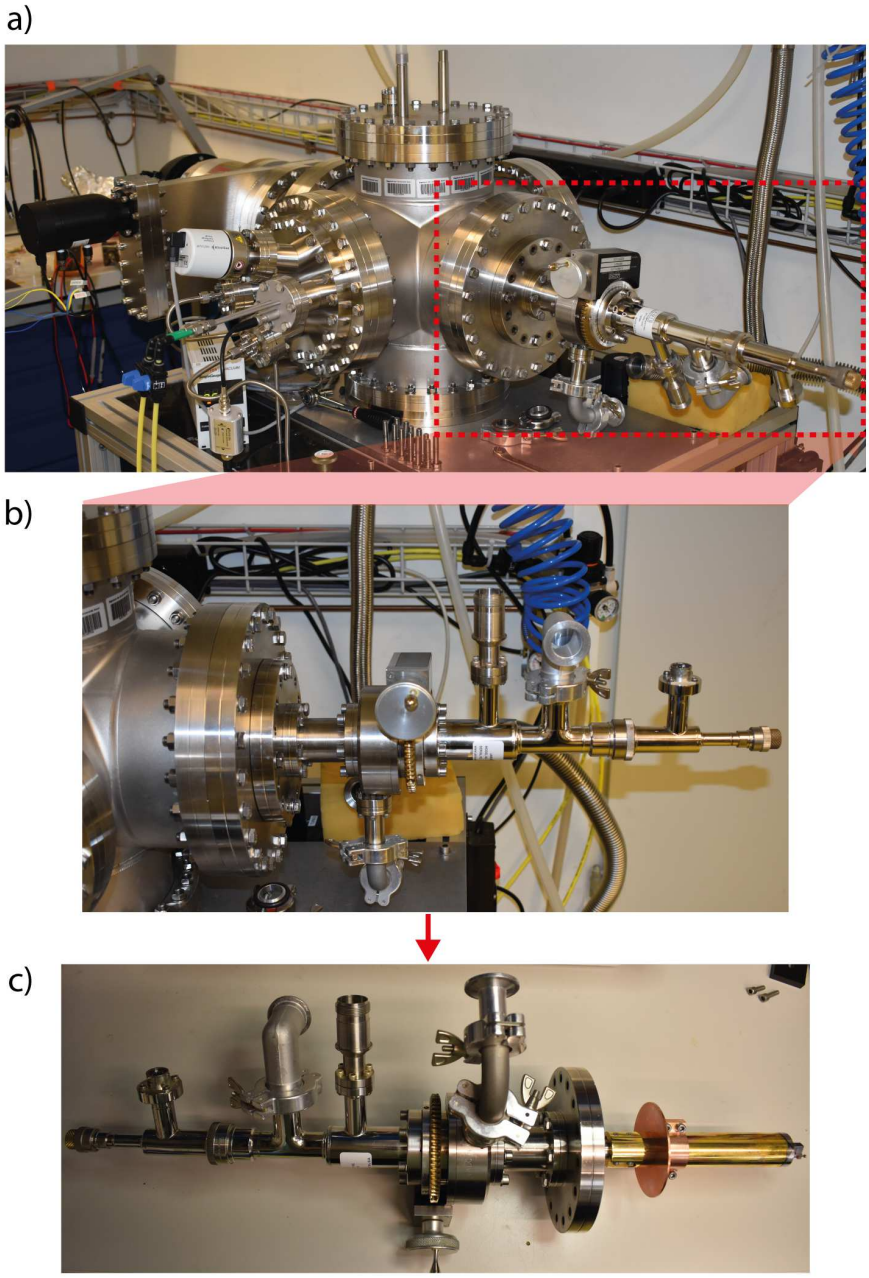

Figure 4.5: a) shows an overview of the custom-made lead evaporator. b) focus on the so-called cold finger, in which ^{4}He flows through an interspace and keep the inner part at 4.2 K. c) shows the dismounted cold finger. In the last part a stage for the tip holder is mounted. The cold finger is projected in order to allow the rotation of the entire stage, once it is mounted in the evaporator.

4.7 Appendix G: High Fields SOT Suppression

The field dependence of the SOT I-V shows a interference pattern suppression for high fields. As shown in Fig.4.6, the critical current stops to follow the classical interference pattern, and it shows a reduced value for the maxima and minima of the pattern. If we go to even higher field we can see the total suppression of the critical current oscillations, and consequently, the lost of sensitivity.

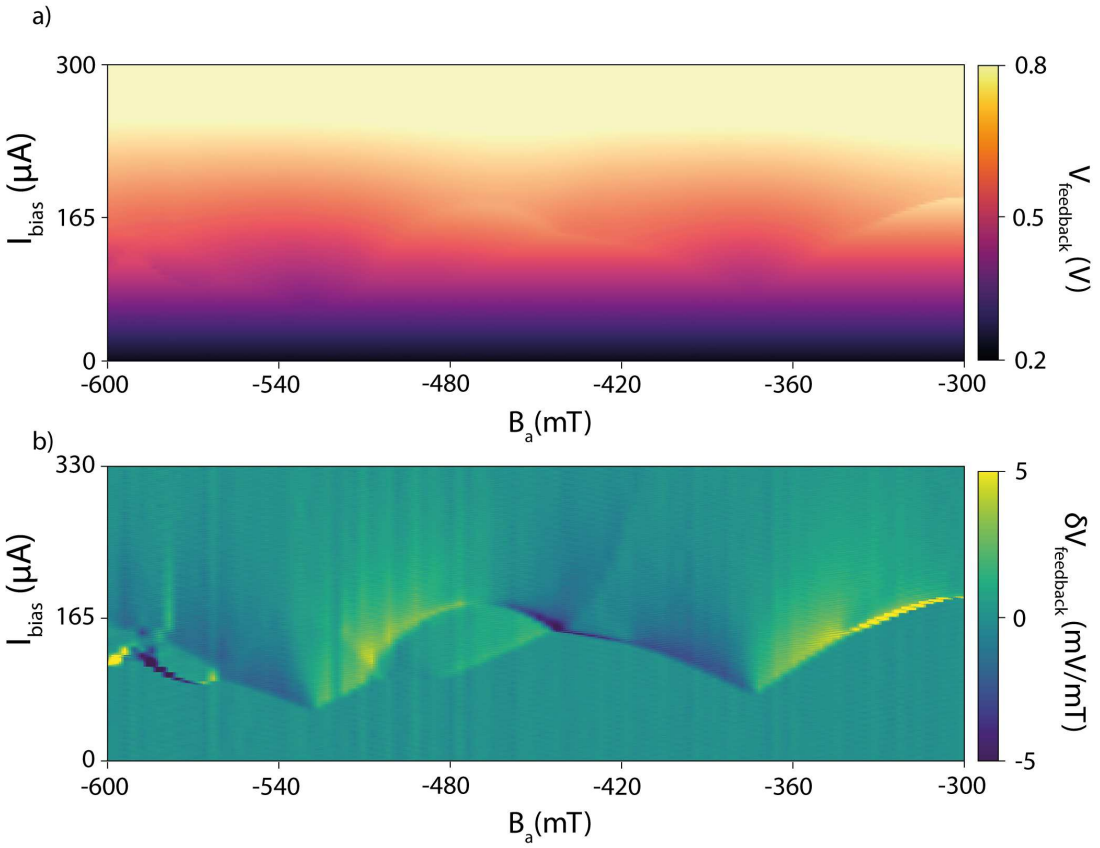

Figure 4.6: Interference-like pattern a), and its derivative b) for the SOT used in the CoFeB nanotube experiment. This characterization is done at higher field in order to detect the operable range of the probe. Increasing the external field B_a above $\approx$ 420 mT, yields to a suppression and underdumping phenomena in the SOT.

4.8 Appendix H: qSOT setup as AFM

In the second chapter, we introduced the experimental setup, including one of the last features, that we developed later. Indeed, the following setup implementation was not used for the measurements presented in this thesis. Nevertheless we introduced this probe upgrade as a self-consistent result, which will be applied in the next future in every planned experiment. This probe upgrade consists in the coupling of our probe, with a qPlus mechanical resonator. In Fig.4.7, we report the 3D rendering of our probe. Differently from the previous SOT setup, a titanium slider is added on the top of the SOT holder, and it uses two main insulating guides to drive the shift only in the direction perpendicular to the SOT length.

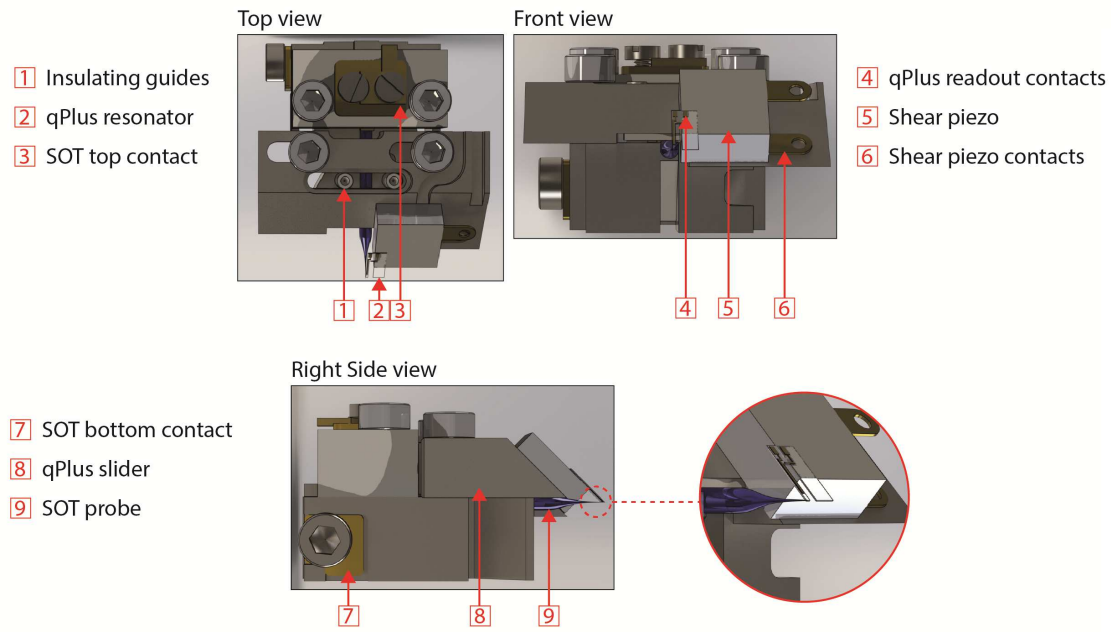

Figure 4.7: Three different view of our qSOT, which present all the components of the probe older. The qPlus is glued on a shear piezo, mounted on a titanium slider, which can slide on the direction normal to the SOT length. Two screws on the top of the slider fix its position once the coupling between the qPlus prong and the apex of the tip is done. The zoom-in show that the coupling occurs in the very last part of the SOT apex (below 200 μm). The coupling is done with a custom-made manipulator stage.

On the top of the titanium slider, we mounted a shear piezo (Thorlabs PL5FBP3), and on top of it, we glued a nanomechanic qPlus sensor. Differently from other similar setups [93–95], in a driven oscillation this nanomechanical sensor produces vibrational modes only on one prong, while the second wider one is completely

fixed on the piezo insulating surface. Our intention was to avoid the collective displacement, and the consequent readout, of the two vibrating prongs for a classic tuningfork. The readout focus is only on the prong which has to be coupled with the SOT.

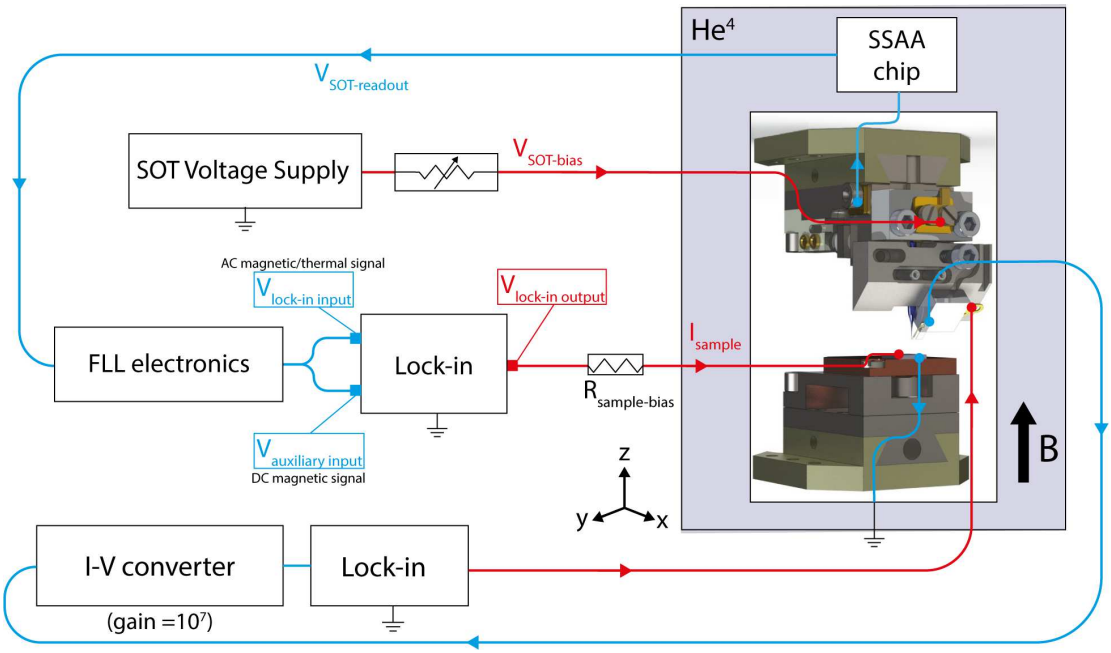

Figure 4.8: The block scheme reproduces the same setup of the one in Fig.2.1, in the second chapter. We added another input/output line, plus the updated rendering for the probe, which consists in the addition of the titanium slider on the top of the SOT probe. A voltage output is sent to the piezo from the lock-in. The shaking of the piezo produces a displacement of the qPlus resonator. Two golden contact on the qPlus provide a capacitative readout of the resonance frequency, and this signal is amplified and converted by an I-V converter, before sending it as input in the lock-in.

The updated version of the block scheme of Fig.2.1 is reported in Fig.4.8 and includes an extra iput/output line for the driving of the shear piezo and the readout of the qPlus resonator coupled to the SOT sensor. The shear piezoelectric stack is driven with a lock-in output AC voltage at the qPlus resonance frequency. The qPlus shakes coherently with the shear piezo and, two thin gold strips deposited aside the qPlus prong, provide a capacitive readout of the frequency and amplitude. The low current signal is amplified by an current-voltage converter with a gain of 10^7, and then is sent in the lock-in input. During the SOT-sample approach, the the phase and frequency shifts are monitored with a PLL control, while a PID allows us to work in a constant amplitude regim, which allows us to observe the

dissipation behavior. Once the qSOT approaches closer than $20 - 30$ nm from the sample surface, both dissipation and frequency sense a drastic shift due to the qSOT-sample force interactions. This process allows us to bring our SOT probe safely close to the area that we want to investigate.

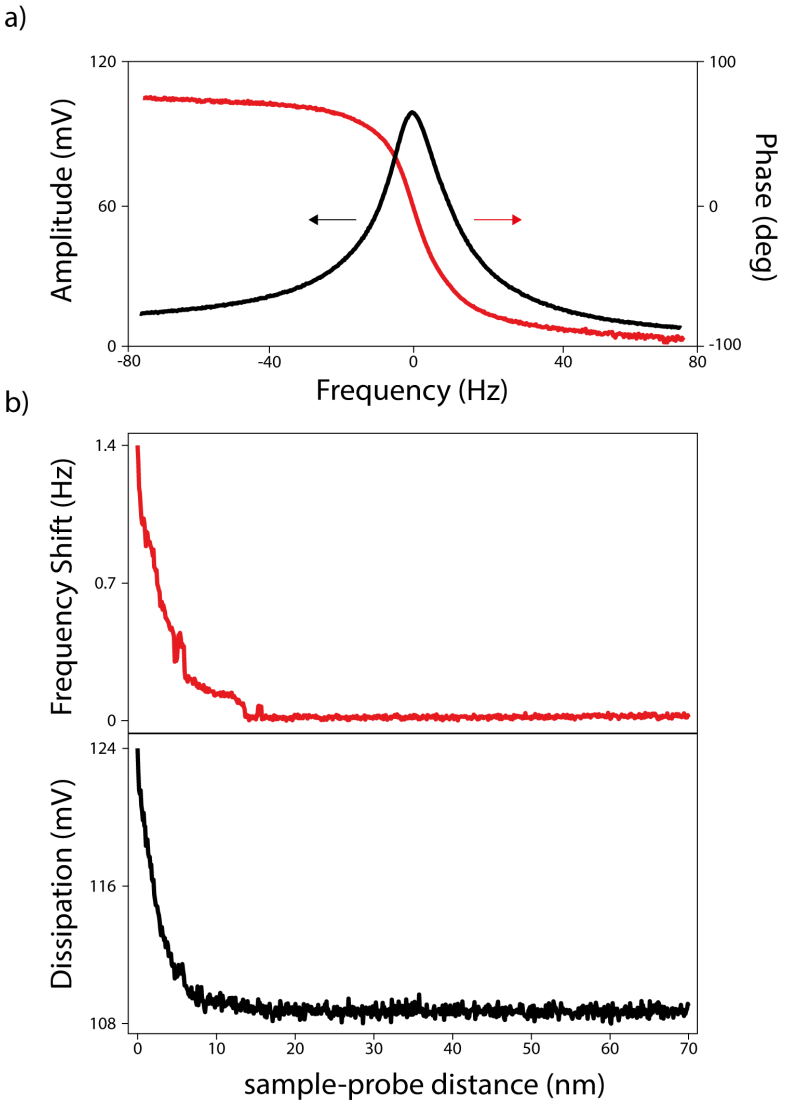

Figure 4.9: a) shows the resonance frequency and the phase for the qSOt used for the data presented in Fig.4.10. The resonance frequency for the qSOT is 34.709 kHz, and its Q-factor 2476 at 4.2 K. b) shows the frequency curve (top), and dissipation curve (bottom) approaching closer to the sample surface with our probe.

Once the oscillating qSOT is below 20 nm distant from the sample, we retract

the probe until we reach a safe distance. This safe distance depends from many factors, e.g. the sample morphology, the cleanliness of the sample from debris or fabrication residues, sample tilt, etc. Then, magnetic and thermal measurements can be done at constant sample-probe distance. Even considering the safe distance, many unexpected events can result in a probe crash. To avoid that, the qPlus has an extra PID safe condition, which produce the immediate retraction of the qSOT if a frequency shift, or dissipation shift is detected. An example of both magnetic map and AFM map are reported in Fig.4.10. First, we measured at constant-high, the DC magnetic signal of the niobium strip sample, then we performed AFM non-contact measurements to investigate the sample morphology.

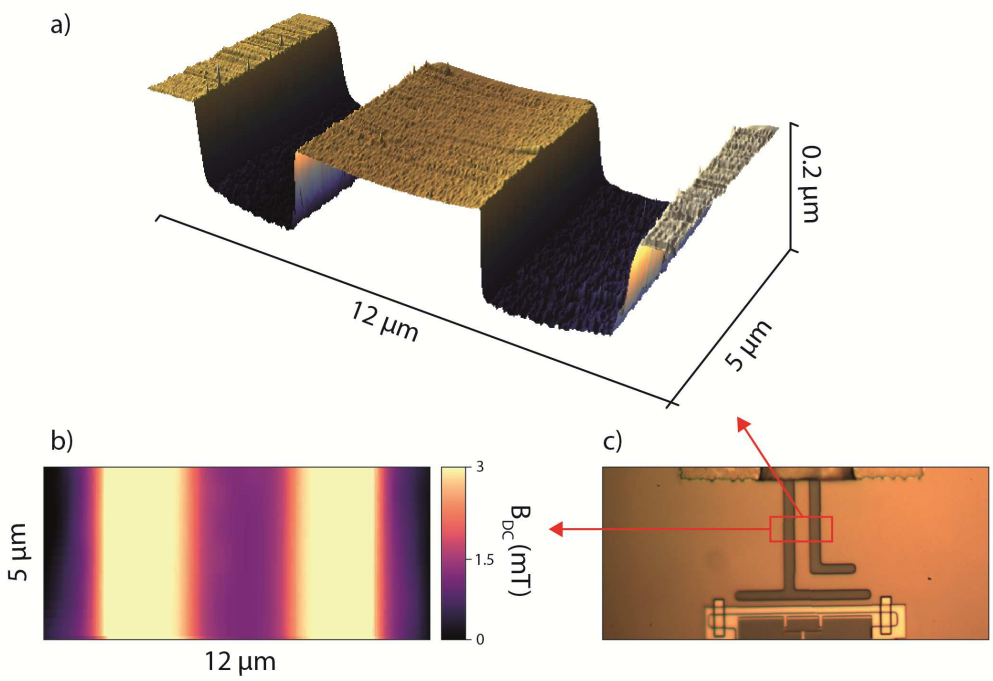

Figure 4.10: A non-contact AFM image a), taken with our qSOT above the a niobium wire, shown in c). Together with the AFM map, we were able to measure the magnetic field response (B_{DC}) in an applied external field of $B_a = 1.5$ mT, where the Meissner effect is shown b).

Bibliography

[1] Richard L. Liboff and Gregory K. Schenter. Electron-phonon scattering contributions to metallic resistivity at 0 K. *Phys. Rev. B*, 54(23):16591–16601, December 1996.

[2] Jack Bass, William P. Pratt, and Peter A. Schroeder. The temperature-dependent electrical resistivities of the alkali metals. *Rev. Mod. Phys.*, 62(3):645–744, July 1990.

[3] Michael Tinkham. *Introduction to Superconductivity*. Dover Publications, 2 edition, June 2004.

[4] Michael Cross. Superconductivity: Ginzburg-Landau Theory. page 7.

[5] E. H. Brandt, G. P. Mikitik, and E. Zeldov. Two regimes of vortex penetration into platelet-shaped type-II superconductors. *J. Exp. Theor. Phys.*, 117(3):439–448, September 2013.

[6] K V Bhagwat and P Chaddah. Magnetization curves of hard superconductor samples with non-zero demagnetization factor. *Pramana - J Phys*, 33(4):521–540, October 1989.

[7] Mathieu N. Grisolia, Antonio Badia-Majos, and Cornelis Jacomius van der Beek. Imaging flux distributions around superconductors: Geometrical susceptibility in the Meissner state. *Journal of Applied Physics*, 114(20):203904, November 2013.

[8] L G Aslamazov and Yu N Ovchinnikov. Josephson Effect in Superconductors separated by a Normal Metal. page 6.

[9] A.I.Braginski J.Clerke. *The SQUID Handbook*. WILEY-VCH.

[10] V. G. Kogan, V. V. Dobrovitski, J. R. Clem, Yasunori Mawatari, and R. G. Mints. Josephson junction in a thin film. *Phys. Rev. B*, 63(14):144501, March 2001.

[11] M. Feynman R. Leighton, R. Sands. *The Feynman Lectures on Physics*. Pearson/Addison-Wesley, 1963.

[12] Aaron Kraft, Christoph Rupprecht, and Yau-Chuen Yam. Superconducting Quantum Interference Device. page 6, 2017.

[13] E. H. Brandt. Geometric edge barrier in the Shubnikov phase of type-II superconductors. *Low Temperature Physics*, 27(9):723–731, September 2001.

[14] Gilson Carneiro and Ernst Helmut Brandt. Vortex lines in films: Fields and interactions. *Phys. Rev. B*, 61(9):6370–6376, March 2000.

[15] M Cyrot. Ginzburg-Landau theory for superconductors. *Rep. Prog. Phys.*, 36(2):103–158, February 1973.

[16] J. Pearl. Current distribution in superconducting films carrying quantized fluxoids. *Appl. Phys. Lett.*, 5(4):65–66, August 1964.

[17] J. R. Kirtley. Fundamental studies of superconductors using scanning magnetic imaging. *Rep. Prog. Phys.*, 73(12):126501, 2010.

[18] F. Tafuri, J. R. Kirtley, P. G. Medaglia, P. Orgiani, and G. Balestrino. Magnetic Imaging of Pearl Vortices in Artificially Layered (Ba $_{0.9}$ Nd $_{0.1}$ CuO $_{2+x}$) m / (CaCuO $_2$) $_n$ Systems. *Phys. Rev. Lett.*, 92(15):157006, April 2004.

[19] E. Zeldov, John R. Clem, M. McElfresh, and M. Darwin. Magnetization and transport currents in thin superconducting films. *Physical Review B*, 49(14):9802–9822, April 1994.

[20] J. McDonald and John R. Clem. Theory of flux penetration into thin films with field-dependent critical current. *Physical Review B*, 53(13):8643–8650, April 1996.

[21] C. P. Bean. Magnetization of Hard Superconductors. *Physical Review Letters*, 8(6):250–253, March 1962.

[22] Ernst Helmut Brandt. Superconductors of finite thickness in a perpendicular magnetic field: Strips and slabs. *Phys. Rev. B*, 54(6):4246–4264, August 1996.

[23] Daniel H. Arcos and Milind N. Kunchur. Suppressed flux motion in magnesium diboride films. *Phys. Rev. B*, 71(18):184516, May 2005.

[24] Ernst Helmut Brandt and Mikhail Indenbom. Type-II-superconductor strip with current in a perpendicular magnetic field. *Physical Review B*, 48(17):12893–12906, November 1993.

[25] G. W. Swan. Current Distribution in a Thin Superconducting Strip. *Journal of Mathematical Physics*, 9(8):1308–1312, August 1968.

[26] P. N. Mikheenko and Yu E. Kuzovlev. Inductance measurements of HTSC films with high critical currents. *Physica C: Superconductivity*, 204(3):229 – 236, 1993.

[27] Y. B. Kim, C. F. Hempstead, and A. R. Strnad. Critical Persistent Currents in Hard Superconductors. *Phys. Rev. Lett.*, 9(7):306–309, October 1962.

[28] Kirensky Institute of Physics Federal Research Center KSC SB RAS and Gokhfeld Denis M. Analysis of Superconductor Magnetization Hysteresis. *J. Sib. Fed. Univ., Math. phys.*, 11(2):219–221, May 2018.

[29] Muyong Kim, Heeyeon Park, Chan Kim, Sang-Kook Park, and H.-C. Ri. The relation between local hysteresis losses and remanent magnetic fields in HTSC films. *IEEE Trans. Appl. Supercond.*, pages 1–1, 2016.

[30] John R. Clem and Zhidong Hao. Theory for the hysteretic properties of the low-field dc magnetization in type-II superconductors. *Phys. Rev. B*, 48(18):13774–13783, November 1993.

[31] M R Koblischka, T H Johansen, and M Murakami. Field-cooled magnetization measurements of Nd-123 bulk superconductors. *Supercond. Sci. Technol.*, 13(6):745–748, June 2000.

[32] C. P. Bean and J. D. Livingston. Surface Barrier in Type-II Superconductors. *Phys. Rev. Lett.*, 12(1):14–16, January 1964.

[33] Ernst Helmut Brandt. Geometric barrier and current string in type-II superconductors obtained from continuum electrodynamics. *Phys. Rev. B*, 59(5):3369–3372, February 1999.

[34] M. Benkraouda and John R. Clem. Magnetic hysteresis from the geometrical barrier in type-II superconducting strips. *Phys. Rev. B*, 53(9):5716–5726, March 1996.

[35] K. H. Kuit, J. R. Kirtley, W. van der Veur, C. G. Molenaar, F. J. G. Roesthuis, A. G. P. Troeman, J. R. Clem, H. Hilgenkamp, H. Rogalla, and J. Flokstra. Vortex trapping and expulsion in thin-film $yba_2cu_3o_{7-x}$ strips. *Phys. Rev. B*, 77(13):134504, April 2008.

[36] K. H. Kuit, J. R. Kirtley, J. R. Clem, H. Rogalla, and J. Flokstra. Vortex Trapping and Expulsion in Thin-Film Type-II Superconducting Strips. *IEEE Transactions on Applied Superconductivity*, 19(3):3537–3540, June 2009.

[37] P. W. Anderson. Theory of Flux Creep in Hard Superconductors. *Physical Review Letters*, 9(7):309–311, October 1962.

[38] Denis Vasyukov, Yonathan Anahory, Lior Embon, Dorri Halbertal, Jo Cuppens, Lior Neeman, Amit Finkler, Yehonathan Segev, Yuri Myasoedov, Michael L. Rappaport, Martin E. Huber, and Eli Zeldov. A scanning superconducting quantum interference device with single electron spin sensitivity. *Nature Nanotech*, 8(9):639–644, September 2013.

[39] Amit Finkler, Yehonathan Segev, Yuri Myasoedov, Michael L. Rappaport, Lior Ne'eman, Denis Vasyukov, Eli Zeldov, Martin E. Huber, Jens Martin, and Amir Yacoby. Self-Aligned Nanoscale SQUID on a Tip. *Nano Lett.*, 10(3):1046–1049, March 2010.

[40] Finkler A. *Ph.D. Thesis: Scanning NanoSQUID Microscope for Study of Vortex Matter in Type-II Superconductors.* Weizmann Institute of Science, 2011.

[41] M. Wyss, A. Mehlin, B. Gross, A. Buchter, A. Farhan, M. Buzzi, A. Kleibert, G. Tutuncuoglu, F. Heimbach, A. Fontcuberta i Morral, D. Grundler, and M. Poggio. Imaging magnetic vortex configurations in ferromagnetic nanotubes. *Phys. Rev. B*, 96(2):024423, July 2017.

[42] A. Mehlin, B. Gross, M. Wyss, T. Schefer, G. Tutuncuoglu, F. Heimbach, A. Fontcuberta i Morral, D. Grundler, and M. Poggio. Observation of end-vortex nucleation in individual ferromagnetic nanotubes. *Phys. Rev. B*, 97(13):134422, April 2018.

[43] O. Fruchart, J.-P. NoziÃ¨res, W. Wernsdorfer, D. Givord, F. Rousseaux, and D. Decanini. Enhanced Coercivity in Submicrometer-Sized Ultrathin Epitaxial Dots with In-Plane Magnetization. *Phys. Rev. Lett.*, 82(6):1305–1308, February 1999.

[44] D. Vasyukov, L. Ceccarelli, M. Wyss, B. Gross, A. Schwarb, A. Mehlin, N. Rossi, G. Tutuncuoglu, F. Heimbach, R. R. Zamani, A. KovÃ¡cs, A. Fontcuberta i Morral, D. Grundler, and M. Poggio. Imaging Stray Magnetic Field of Individual Ferromagnetic Nanotubes. *Nano Lett.*, 18(2):964–970, February 2018.

[45] L. Lopez-Diaz, J. Rothman, M. Klani, and J.A.C. Bland. Computational study of first magnetization curves in small rings. *IEEE Trans. Magn.*, 36(5):3155–3157, September 2000.

[46] J. Rothman, M. Klaui, L. Lopez-Diaz, C. A. F. Vaz, A. Bleloch, J. A. C. Bland, Z. Cui, and R. Speaks. Observation of a Bi-Domain State and

Nucleation Free Switching in Mesoscopic Ring Magnets. *Phys. Rev. Lett.*, 86(6):1098–1101, February 2001.

[47] P. Landeros, O. J. Suarez, A. Cuchillo, and P. Vargas. Equilibrium states and vortex domain wall nucleation in ferromagnetic nanotubes. *Phys. Rev. B*, 79(2):024404, January 2009.

[48] Riccardo Hertel and Jurgen Kirschner. Magnetic drops in a soft-magnetic cylinder. *Journal of Magnetism and Magnetic Materials*, 278(3):L291–L297, July 2004.

[49] J Escrig, D Altbir, and K Nielsch. Magnetic properties of bi-phase micro- and nanotubes. *Nanotechnology*, 18(22):225704, June 2007.

[50] J. Escrig, P. Landeros, D. Altbir, E.E. Vogel, and P. Vargas. Phase diagrams of magnetic nanotubes. *Journal of Magnetism and Magnetic Materials*, 308(2):233–237, January 2007.

[51] P. Landeros, S. Allende, J. Escrig, E. Salcedo, D. Altbir, and E. E. Vogel. Reversal modes in magnetic nanotubes. *Appl. Phys. Lett.*, 90(10):102501, March 2007.

[52] A. P. Chen, K. Y. Guslienko, and J. Gonzalez. Magnetization configurations and reversal of thin magnetic nanotubes with uniaxial anisotropy. *Journal of Applied Physics*, 108(8):083920, October 2010.

[53] P. Landeros and Alvaro S. Nunez. Domain wall motion on magnetic nanotubes. *Journal of Applied Physics*, 108(3):033917, August 2010.

[54] Ai-Ping Chen, Julian M. Gonzalez, and Konstantin Y. Guslienko. Magnetization configurations and reversal of magnetic nanotubes with opposite chiralities of the end domains. *Journal of Applied Physics*, 109(7):073923, April 2011.

[55] Ming Yan, Christian Andreas, Attila Kakay, Felipe Garcia-Sanchez, and Riccardo Hertel. Chiral symmetry breaking and pair-creation mediated Walker breakdown in magnetic nanotubes. *Appl. Phys. Lett.*, 100(25):252401, June 2012.

[56] D. P. Weber, D. Ruffer, A. Buchter, F. Xue, E. Russo-Averchi, R. Huber, P. Berberich, J. Arbiol, A. Fontcuberta i Morral, D. Grundler, and M. Poggio. Cantilever Magnetometry of Individual Ni Nanotubes. *Nano Lett.*, 12(12):6139–6144, December 2012.

[57] B. Gross, D. P. Weber, D. Ruffer, A. Buchter, F. Heimbach, A. Fontcuberta i Morral, D. Grundler, and M. Poggio. Dynamic cantilever magnetometry of individual CoFeB nanotubes. *Phys. Rev. B*, 93(6):064409, February 2016.

[58] A. Buchter, J. Nagel, D. Ruffer, F. Xue, D. P. Weber, O. F. Kieler, T. Weimann, J. Kohlmann, A. B. Zorin, E. Russo-Averchi, R. Huber, P. Berberich, A. Fontcuberta i Morral, M. Kemmler, R. Kleiner, D. Koelle, D. Grundler, and M. Poggio. Reversal Mechanism of an Individual Ni Nanotube Simultaneously Studied by Torque and SQUID Magnetometry. *Phys. Rev. Lett.*, 111(6):067202, August 2013.

[59] A. Buchter, R. Wolbing, M. Wyss, O. F. Kieler, T. Weimann, J. Kohlmann, A. B. Zorin, D. Ruffer, F. Matteini, G. Tutuncuoglu, F. Heimbach, A. Kleibert, A. Fontcuberta i Morral, D. Grundler, R. Kleiner, D. Koelle, and M. Poggio. Magnetization reversal of an individual exchange-biased permalloy nanotube. *Phys. Rev. B*, 92(21):214432, December 2015.

[60] Daniel Ruffer, Rupert Huber, Paul Berberich, Stephan Albert, Eleonora Russo-Averchi, Martin Heiss, Jordi Arbiol, Anna Fontcuberta i Morral, and Dirk Grundler. Magnetic states of an individual Ni nanotube probed by anisotropic magnetoresistance. *Nanoscale*, 4(16):4989, 2012.

[61] K. Baumgaertl, F. Heimbach, S. Maendl, D. Rueffer, A. Fontcuberta i Morral, and D. Grundler. Magnetization reversal in individual Py and CoFeB nanotubes locally probed via anisotropic magnetoresistance and anomalous Nernst effect. *Appl. Phys. Lett.*, 108(13):132408, March 2016.

[62] Dorri Halbertal, Moshe Ben Shalom, Aviram Uri, Kousik Bagani, Alexander Y. Meltzer, Ido Marcus, Yuri Myasoedov, John Birkbeck, Leonid S. Levitov, Andre K. Geim, and Eli Zeldov. Imaging resonant dissipation from individual atomic defects in graphene. *Science*, 358(6368), December 2017.

[63] Daniel Ruffer, Marlou Slot, Rupert Huber, Thomas Schwarze, Florian Heimbach, Gozde Tutuncuoglu, Federico Matteini, Eleonora Russo-Averchi, Andras Kovacs, Rafal Dunin-Borkowski, Reza R. Zamani, Joan R. Morante, Jordi Arbiol, Anna Fontcuberta i Morral, and Dirk Grundler. Anisotropic magnetoresistance of individual CoFeB and Ni nanotubes with values of up to 1.4% at room temperature. *APL Materials*, 2(7):076112, July 2014.

[64] A. T. Hindmarch, C. J. Kinane, M. MacKenzie, J. N. Chapman, M. Henini, D. Taylor, D. A. Arena, J. Dvorak, B. J. Hickey, and C. H. Marrows. Interface Induced Uniaxial Magnetic Anisotropy in Amorphous CoFeB Films on AlGaAs(001). *Phys. Rev. Lett.*, 100(11):117201, March 2008.

[65] T. Schwarze and D. Grundler. Magnonic crystal wave guide with large spin-wave propagation velocity in CoFeB. *Appl. Phys. Lett.*, 102(22):222412, June 2013.

[66] Arne Vansteenkiste, Jonathan Leliaert, Mykola Dvornik, Mathias Helsen, Felipe Garcia-Sanchez, and Bartel Van Waeyenberge. The design and verification of MuMax3. *AIP Advances*, 4(10):107133, October 2014.

[67] J. A. Katine, Michael K. Ho, Yongho Sungtaek Ju, and C. T. Rettner. Patterning damage in narrow trackwidth spin-valve sensors. *Appl. Phys. Lett.*, 83(2):401–403, July 2003.

[68] S Khizroev and D Litvinov. Focused-ion-beam-based rapid prototyping of nanoscale magnetic devices. *Nanotechnology*, 15(3):R7–R15, March 2004.

[69] Maxim Tsoi, Paul Barbara, James Erskine, John Markert, and Jack Swift. Magnetic Domain Wall Dynamics in Nanoscale Thin Film Structures. page 110, 2008.

[70] J. Albrecht, A. T. Matveev, J. Strempfer, H. U. Habermeier, D. V. Shantsev, Y. M. Galperin, and T. H. Johansen. Dramatic Role of Critical Current Anisotropy on Flux Avalanches in MgB 2 Films. *Phys. Rev. Lett.*, 98(11):117001, March 2007.

[71] J. L. MacManus-Driscoll, S. R. Foltyn, Q. X. Jia, H. Wang, A. Serquis, L. Civale, B. Maiorov, M. E. Hawley, M. P. Maley, and D. E. Peterson. Strongly enhanced current densities in superconducting coated conductors of YBa_2 cu_3 o_{7+x} + $bazro_3$. *Nature Mater*, 3(7):439–443, July 2004.

[72] L. Fang, Y. Jia, V. Mishra, C. Chaparro, V. K. Vlasko-Vlasov, A. E. Koshelev, U. Welp, G. W. Crabtree, S. Zhu, N. D. Zhigadlo, S. Katrych, J. Karpinski, and W. K. Kwok. Huge critical current density and tailored superconducting anisotropy in SmFeAsO0.8f0.15 by low-density columnar-defect incorporation. *Nat Commun*, 4(1):2655, December 2013.

[73] T. Haugan, P. N. Barnes, R. Wheeler, F. Meisenkothen, and M. Sumption. Addition of nanoparticle dispersions to enhance flux pinning of the $yba_2cu_3o_{7-x}$ superconductor. *Nature*, 430(7002):867–870, August 2004.

[74] P Mele, K Matsumoto, T Horide, O Miura, A Ichinose, M Mukaida, Y Yoshida, and S Horii. Tuning of the critical current in YBa $_2$ Cu $_3$ O $_{7â x}$ thin films by controlling the size and density of Y $_2$ O $_3$ nanoislands on annealed SrTiO $_3$ substrates. *Supercond. Sci. Technol.*, 19(1):44–50, January 2006.

[75] S. Kang. High-Performance High-Tc Superconducting Wires. *Science*, 311(5769):1911–1914, March 2006.

[76] J. Gutierrez, A. Llordes, J. Gazquez, M. Gibert, N. Roma, S. Ricart, A. Pomar, F. Sandiumenge, N. Mestres, T. Puig, and X. Obradors. Strong isotropic flux pinning in solution-derived $yba_2cu_3o_{7-x}$ nanocomposite superconductor films. *Nature Mater*, 6(5):367–373, May 2007.

[77] B. Maiorov, S. A. Baily, H. Zhou, O. Ugurlu, J. A. Kennison, P. C. Dowden, T. G. Holesinger, S. R. Foltyn, and L. Civale. Synergetic combination of different types of defect to optimize pinning landscape using $bazro_3$-doped $yba_2cu_3o_7$. *Nature Mater*, 8(5):398–404, May 2009.

[78] A. Llordes, A. Palau, J. Gazquez, M. Coll, R. Vlad, A. Pomar, J. Arbiol, R. Guzman, S. Ye, V. Rouco, F. Sandiumenge, S. Ricart, T. Puig, M. Varela, D. Chateigner, J. Vanacken, J. Gutierrez, V. Moshchalkov, G. Deutscher, C. Magen, and X. Obradors. Nanoscale strain-induced pair suppression as a vortex-pinning mechanism in high-temperature superconductors. *Nature Mater*, 11(4):329–336, April 2012.

[79] S. Lee, C. Tarantini, P. Gao, J. Jiang, J. D. Weiss, F. Kametani, C. M. Folkman, Y. Zhang, X. Q. Pan, E. E. Hellstrom, D. C. Larbalestier, and C. B. Eom. Artificially engineered superlattices of pnictide superconductors. *Nature Mater*, 12(5):392–396, May 2013.

[80] R. Cordoba, T. I. Baturina, J. Sese, A. Yu Mironov, J. M. De Teresa, M. R. Ibarra, D. A. Nasimov, A. K. Gutakovskii, A. V. Latyshev, I. Guillamon, H. Suderow, S. Vieira, M. R. Baklanov, J. J. Palacios, and V. M. Vinokur. Magnetic field-induced dissipation-free state in superconducting nanostructures. *Nat Commun*, 4(1):1437, June 2013.

[81] C. Song, T. W. Heitmann, M. P. DeFeo, K. Yu, R. McDermott, M. Neeley, John M. Martinis, and B. L. T. Plourde. Microwave response of vortices in superconducting thin films of Re and Al. *Phys. Rev. B*, 79(17):174512, May 2009.

[82] G Wendin. Quantum information processing with superconducting circuits: a review. *Rep. Prog. Phys.*, 80(10):106001, October 2017.

[83] Andreas Engel, Julia Lonsky, Xiaofu Zhang, and Andreas Schilling. Detection Mechanism in SNSPD: Numerical Results of a Conceptually Simple, Yet Powerful Detection Model. *IEEE Trans. Appl. Supercond.*, 25(3):1–7, June 2015.

[84] L. Ceccarelli, D. Vasyukov, M. Wyss, G. Romagnoli, N. Rossi, L. Moser, and M. Poggio. Imaging pinning and expulsion of individual superconducting vortices in amorphous MoSi thin films. *Phys. Rev. B*, 100(10):104504, September 2019.

[85] J. Brisbois, B. Raes, J. Van de Vondel, V. V. Moshchalkov, and A. V. Silhanek. Determination of the magnetic penetration depth in a superconducting Pb film. *Journal of Applied Physics*, 115(10):103906, March 2014.

[86] Shugo Kubo. Superconducting properties of amorphous MoX (X=Si, Ge) alloy films for Abrikosov vortex memory. *Journal of Applied Physics*, 63(6):2033–2045, March 1988.

[87] Gheorghe Stan, Stuart B. Field, and John M. Martinis. Critical Field for Complete Vortex Expulsion from Narrow Superconducting Strips. *Physical Review Letters*, 92(9), March 2004.

[88] L. Embon, Y. Anahory, A. Suhov, D. Halbertal, J. Cuppens, A. Yakovenko, A. Uri, Y. Myasoedov, M. L. Rappaport, M. E. Huber, A. Gurevich, and E. Zeldov. Probing dynamics and pinning of single vortices in superconductors at nanometer scales. *Sci Rep*, 5(1):7598, July 2015.

[89] L. Embon, Y. Anahory, Z.L. Jelic, E. O. Lachman, Y. Myasoedov, M. E. Huber, G. P. Mikitik, A. V. Silhanek, M. V. Milosevic, A. Gurevich, and E. Zeldov. Imaging of super-fast dynamics and flow instabilities of superconducting vortices. *Nat Commun*, 8(1):85, December 2017.

[90] M. Pannetier, Ph. Lecoeur, P. Bernstein, T. D. Doan, and J. F. Hamet. Characterization of pinning and vortex motion in thin superconducting microbridges. *Phys. Rev. B*, 62(22):15162–15171, December 2000.

[91] Ophir M. Auslaender, Lan Luan, Eric W. J. Straver, Jennifer E. Hoffman, Nicholas C. Koshnick, Eli Zeldov, Douglas A. Bonn, Ruixing Liang, Walter N. Hardy, and Kathryn A. Moler. Mechanics of individual isolated vortices in a cuprate superconductor. *Nature Phys*, 5(1):35–39, January 2009.

[92] D. Halbertal, J. Cuppens, M. Ben Shalom, L. Embon, N. Shadmi, Y. Anahory, H. R. Naren, J. Sarkar, A. Uri, Y. Ronen, Y. Myasoedov, L. S. Levitov, E. Joselevich, A. K. Geim, and E. Zeldov. Nanoscale thermal imaging of dissipation in quantum systems. *Nature*, 539(7629):407–410, November 2016.

[93] A. Marguerite, J. Birkbeck, A. Aharon-Steinberg, D. Halbertal, K. Bagani, I. Marcus, Y. Myasoedov, A. K. Geim, D. J. Perello, and E. Zeldov. Imaging work and dissipation in the quantum Hall state in graphene. *Nature*, 575(7784):628–633, November 2019.

[94] Aviram Uri, Youngwook Kim, Kousik Bagani, Cyprian K. Lewandowski, Sameer Grover, Nadav Auerbach, Ella O. Lachman, Yuri Myasoedov, Takashi Taniguchi, Kenji Watanabe, Jurgen Smet, and Eli Zeldov. Nanoscale imaging of equilibrium quantum Hall edge currents and of the magnetic monopole response in graphene. *Nat. Phys.*, 16(2):164–170, February 2020.

[95] Dorri Halbertal, Moshe Ben Shalom, Aviram Uri, Kousik Bagani, Alexander Y. Meltzer, Ido Marcus, Yuri Myasoedov, John Birkbeck, Leonid S. Levitov, Andre K. Geim, and Eli Zeldov. Imaging resonant dissipation from individual atomic defects in graphene. *Science*, 358(6368):1303–1306, December 2017.

[96] Jan Muller, Jayaraman Rajeswari, Ping Huang, Yoshie Murooka, Henrik M. Ronnow, Fabrizio Carbone, and Achim Rosch. Magnetic Skyrmions and Skyrmion Clusters in the Helical Phase of Cu 2 OSeO 3. *Physical Review Letters*, 119(13), September 2017.

[97] Arianna Casiraghi, Hector Corte-Leon, Mehran Vafaee, Felipe Garcia-Sanchez, Gianfranco Durin, Massimo Pasquale, Gerhard Jakob, Mathias Klaui, and Olga Kazakova. Individual skyrmion manipulation by local magnetic field gradients. *Commun Phys*, 2(1):145, December 2019.

[98] Olivia Nicoletti. 3D skyrmion imaging. *Nature Mater*, 13(7):664–664, July 2014.

[99] J. Brandao, D. A. Dugato, R. L. Seeger, J. C. Denardin, T. J. A. Mori, and J. C. Cezar. Observation of magnetic skyrmions in unpatterned symmetric multilayers at room temperature and zero magnetic field. *Sci Rep*, 9(1):4144, December 2019.

[100] Takashi Kurumaji, Taro Nakajima, Victor Ukleev, Artem Feoktystov, Takahisa Arima, Kazuhisa Kakurai, and Yoshinori Tokura. Neel-Type Skyrmion Lattice in the Tetragonal Polar Magnet VOSe 2 O 5. *Physical Review Letters*, 119(23), December 2017.

[101] Christina Psaroudaki and Daniel Loss. Quantum Depinning of a Magnetic Skyrmion. *Phys. Rev. Lett.*, 124(9):097202, March 2020.

[102] S. Frasca, B. Korzh, M. Colangelo, D. Zhu, A. E. Lita, J. P. Allmaras, E. E. Wollman, V. B. Verma, A. E. Dane, E. Ramirez, A. D. Beyer, S. W. Nam, A. G. Kozorezov, M. D. Shaw, and K. K. Berggren. Determining the depairing current in superconducting nanowire single-photon detectors. *Phys. Rev. B*, 100(5):054520, August 2019.

[103] Archan Banerjee, Luke J Baker, Alastair Doye, Magnus Nord, Robert M Heath, Kleanthis Erotokritou, David Bosworth, Zoe H Barber, Ian MacLaren, and Robert H Hadfield. Characterisation of amorphous molybdenum silicide (MoSi) superconducting thin films and nanowires. *Supercond. Sci. Technol.*, 30(8):084010, August 2017.

[104] Misael Caloz, Matthieu Perrenoud, Claire Autebert, Boris Korzh, Markus Weiss, Christian Schonenberger, Richard J. Warburton, Hugo Zbinden, and Felix Bussieres. High-detection efficiency and low-timing jitter with amorphous superconducting nanowire single-photon detectors. *Appl. Phys. Lett.*, 112(6):061103, February 2018.

Acknowledgements

In the last four years I went through many challenges in both my workplace and my private life. I manage to overcome those obstacles with the help of many people around me, and the least I can do is to acknowledge all of them.

Firstly, I want to thank Prof. Martino Poggio, who gave me the opportunity to be part of this group and to work in this PhD project in the last four years. Moreover, I want to show him my gratitude for his incredible patience towards my not always easy character. I want to thank Prof. José Maria De Teresa, that so kindly accepted to be part of the defense committee, and reviewed my thesis with incredible availability. Many thanks to Prof. Christoph Bruder, that kindly accepted the role of chair during my defense.

A great acknowledgment is due to all the people and collaborators, who helped in this work under many different aspects and contributions. Prof. Anna Fontcuberta i Morral and her group for the CoFeB nanotubes fabrication, Prof. Christian Schönenberger, Prof. Richard Warburton, and Mr. Daniel Sacker for guidance in the fabrication of the MoSi samples. The technical support received from our mechanical and electronic workshops was fundamental, and in particular, I want to thank Sascha Martin for being so helpful and patience for my (sometimes peculiar) CAD designs.

I started this project under the guidance of Dr. Denis Vasyukov; he gave me the first, brutal but necessary, introduction to the experimental physics world, which helped me to easily overcome all the challenging tasks I faced along this project. I am very grateful towards Nicola Rossi, with whom I have team up in the last part of my PhD. He introduced me the wonderful engineering side of the physics research, showing me the "secret ways of the Ohm's Law" and its underestimated value. A great thank to Davide Cadeddu who was always able to make the workplace lighter, promptly helping to raise the environment mood. Thank to Giulio Romagnoli for his help in the lab, and his constant enthusiasm for

outdoor activities. I also want to express my gratitude towards all the members of the Poggio Lab. group with whom I shared good and bad times: Floris Braakman, Boris Groß, Andrea Mehlin, Marcus Wyss, Thibaud Ruelle, Simon Philipp, David Jaeger, Hinrich Mattiat. I want also to acknowledge Claudia Wirth for her kind assistance with all the bureaucratic aspects of my journey.

Until here, I have expressed my gratitude to all the colleagues and friends in my workplace, but it is sure that I received an incredible support also from far from Basel. I will be never able to express enough gratitude to my family. They supported me on all my decisions. I would not be here writing this words without them. Thank to Maria Antonietta Fazio, we share a wonderful long journey together and thanks to her care and love I was able to overcome many tough obstacles during this PhD. Her essential emotional support was priceless and fundamental. I can not forget to mention my dearest friends, Filippo De Angelis and Parid Doksani. They always made me feel at home despite the long distance between us. Thanks to Chiara Canali for her many tips and advice. They gave me the will to go ahead even in disheartening situations. Finally, thanks to all my friends from Italy and around the world, and to all of those who I felt close when I needed the most.

CV

Lorenzo Ceccarelli

Address

Department of Physics, Klingelbergstrasse 82, 4056 Basel, Switzerland
Email: lorenzo.ceccarelli@unibas.ch

Education

2020 **University of Basel**
PhD in Experimental Physics

- Thesis title: Scanning probe microscopy with SQUID on tip sensor.
- Advisor: Prof. Dr. Martino Poggio

2015 **University of Bologna**
M.Cs. degree in Condensed Matter Physics

- Thesis title: Optimization of numerical methods and realization of an experimental setup for EIT imaging of 3D cell cultures.
- Thesis developed at: **Technical University of Denmark**, Department of Micro-and Nanotechnology
- M.Sc. Thesis advisor: Prof. Beatrice Fraboni
- M.Sc. Thesis co-advisors: Prof. Jenny Emnéus, Dr. Chiara Canali

2012 **University of Bologna**
B.Sc. degree in Physics

- Thesis title: Physical analysis of geothermal systems applied to energy consumption.
- Thesis developed in collaboration with: **Institute for Geophysics and Volcanology (INGV)**
- B.Sc. Thesis advisor: Prof. Maurizio Bonafede
- BSc thesis co-advisor: Dr. Gabriele Ponzoni

Publications

- Imaging pinning and expulsion of individual superconducting vortices in amorphous MoSi thin films
  L. Ceccarelli, D. Vasyukov, M. Wyss, G. Romagnoli, N. Rossi, L. Moser, and M. Poggio
  Phys. Rev. B 100, 104504 - Published 5 September 2019

- Stray-Field Imaging of a Chiral Artificial Spin Ice during Magnetization Reversal
  M. Wyss, S. Gliga, D. Vasyukov, **L. Ceccarelli**, G. Romagnoli, J. Cui, A. Kleibert, R. L. Stamps, and M. Poggio
  ACS Nano 2019, 13, 12, 13910-13916 - Published 10 December 2019

- Imaging Stray Magnetic Field of Individual Ferromagnetic Nanotubes
  D. Vasyukov*, **L. Ceccarelli***, M. Wyss, B. Gross, A. Schwarb, A. Mehlin, N. Rossi, G. Tütüncüoglu, F. Heimbach, R. R. Zamani, A. Kovács, A. Fontcuberta i Morral, D. Grundler, and M. Poggio
  (*: coauthors)
  Nano Lett. 2018, 18, 2, 964-970 - Published 2 January 2018

- Electrical impedance tomography methods for miniaturised 3D systems
  C. Canali, K. Aristovich, **L. Ceccarelli**, L. B. Larsen, Ø. G. Martinsen, A. Wolff, M. Dufva, J. Emnéus, and A. Heiskanen J Electr Bioimp, vol. 7, pp. 59-67 - Published 21 December 2016

Presentations

APS March Meeting. Boston, USA 2019
Imaging superconducting vortex dynamics in amorphous MoSi thin films (Oral)

10th NCCR QSIT General Meeting, Arosa, Switzerland 2019
Imaging superconducting vortex dynamics in amorphous MoSi thin films (Oral)

International Workshop on Magnetism and Superconductivity at the Nanoscale. Coma-Ruga, Spain 2018
Imaging superconducting vortex dynamics in amorphous MoSi thin films (Oral)

Spin Mechanics, Lake Louise, Canada 2017
Direct imaging of a vortex state in short CoFeB nanotubes (Poster)

International Workshop on Magnetism and Superconductivity at the Nanoscale. Coma-Ruga, Spain 2017
Direct imaging of a vortex state in short CoFeB nanotubes (Poster)